

---

# Chiral phonons as the carriers of angular momentum in the ultrafast demagnetization of nickel

Sonja Regina Tauchert

---



München 2021



---

# Chiral phonons as the carriers of angular momentum in the ultrafast demagnetization of nickel

Sonja Regina Tauchert

---

Dissertation  
an der Fakultät für Physik  
der Ludwig-Maximilians-Universität  
München

vorgelegt von  
Sonja Regina Tauchert  
aus München

München, den 17.05.2021

Erstgutachter: Prof. Dr. Ferenc Krausz

Zweitgutachter: Prof. Dr. Alexander Urban

Tag der mündlichen Prüfung: 07.07.2021

# Contents

<b>Zusammenfassung</b>	<b>xi</b>
<b>Abstract</b>	<b>xiii</b>
<b>List of publications</b>	<b>xv</b>
<b>1 Introduction</b>	<b>1</b>
1.1 The Einstein-de-Haas effect . . . . .	2
1.2 Discovery of ultrafast laser-demagnetization . . . . .	3
1.3 Where is the angular momentum? . . . . .	5
1.4 Structure of this thesis . . . . .	6
<b>2 Experimental idea: chiral phonons with angular momentum</b>	<b>9</b>
2.1 Chiral phonons with angular momentum . . . . .	9
2.2 Ultrafast pump-probe diffraction with terahertz-compressed electron pulses . . . . .	11
2.3 Diffraction physics . . . . .	14
<b>3 Necessary experimental advances</b>	<b>19</b>
3.1 Optical pulse compression . . . . .	19
3.2 Ultrafast electron pulses and compression by THz radiation . . . . .	21
3.3 Control of magnetization and remagnetization . . . . .	24
<b>4 Sample preparation</b>	<b>29</b>
4.1 Requirements for electron diffraction . . . . .	29
4.2 Sample preparation and characterization . . . . .	29
4.3 Pre-characterization and proof of epitaxial growth . . . . .	30
<b>5 Femtosecond electron diffraction in nickel</b>	<b>35</b>

---

5.1	Static electron diffraction characterizations . . . . .	35
5.2	Angle-dependent intensity and rocking curves . . . . .	37
5.3	Time-resolved observations of Ni dynamics . . . . .	39
5.4	Time-resolved observations of Si dynamics . . . . .	44
5.5	Fluence dependency . . . . .	44
5.6	Base temperature . . . . .	46
5.7	Asymmetry and evidence for chiral phonons . . . . .	48
<b>6</b>	<b>Theoretical considerations and molecular dynamics simulation</b>	<b>53</b>
6.1	Definition of the problem . . . . .	53
6.2	Numerical simulation . . . . .	55
6.3	Results . . . . .	56
<b>7</b>	<b>Discussion, conclusions &amp; outlook</b>	<b>59</b>
7.1	Previous theories of demagnetization . . . . .	59
7.2	Asymmetry in electron diffraction . . . . .	61
7.3	Stepwise Einstein-de-Haas effect with chiral phonons . . . . .	65
7.4	Outlook . . . . .	68
	<b>Data achiving</b>	<b>70</b>
	<b>Acknowledgments</b>	<b>86</b>

# List of Figures

1.1	Einstein-de Haas effect and Barnett effect . . . . .	3
1.2	First observation of ultrafast demagnetization . . . . .	4
2.1	Phonon angular momentum . . . . .	11
2.2	Experimental setup . . . . .	12
2.3	Experimental setup within chamber . . . . .	13
3.1	Necessary experimental advances: optical pulse compression . . . . .	19
3.2	Necessary experimental advances: FROG . . . . .	20
3.3	Necessary experimental advances: electron compression and streaking setup . . . . .	23
3.4	Visualization of streaking . . . . .	24
3.5	Necessary experimental advances: Hysteresis curves . . . . .	25
3.6	Necessary experimental advances: Simulation of the out-of-plane magnetic field . . . . .	25
3.7	Necessary experimental advances: Simulation of the in-plane magnetic field . . . . .	26
4.1	Ni on Si . . . . .	31
4.2	X-ray diffraction . . . . .	33
5.1	Diffraction pattern . . . . .	36
5.2	2D rocking curve . . . . .	38
5.3	1D rocking curve of Bragg spot Ni(020) . . . . .	39
5.4	Temporal evolution of width of the Ni Bragg spots . . . . .	40
5.5	Temporal evolution of movement of the Ni Bragg spots . . . . .	41
5.6	Difference image and temporal development of Ni . . . . .	42
5.7	Comparison between time-dependent Ni dynamics and Si dynamics . . . . .	44
5.8	Fluence dependency . . . . .	45

---

5.9	Estimation of base temperature . . . . .	47
5.10	Magneto-optical Faraday effect . . . . .	48
5.11	Time-resolved development of the anisotropy . . . . .	49
5.12	Fluence dependence of the anisotropy . . . . .	50
6.1	Simulations: general idea . . . . .	54
6.2	Visualization of the algorithm . . . . .	55
6.3	Simulations: results . . . . .	56
6.4	Simulations: evolution with different settings . . . . .	57
7.1	Illustrations of spin-flip scattering . . . . .	61
7.2	Idea for angular momentum conservation . . . . .	62
7.3	Idea: chiral phonons observable in diffraction . . . . .	63
7.4	Scheme of demagnetization process . . . . .	64
7.5	Torque transfer to lattice . . . . .	65

# List of Tables

4.1	Best fit parameters for XRR . . . . .	32
5.1	Overview of lattice parameters . . . . .	37



# Zusammenfassung

In einem ferromagnetischen Material ist die Ausrichtung der Elektronenspins mit einem Drehimpuls verbunden. Der Barnett-Effekt [1] und der Einstein-de-Haas-Effekt [2, 3] demonstrieren die Umwandlung von Spin-Drehimpuls in mechanische Bewegung und umgekehrt. 1996 entdeckten Beaurepaire et al. [4], dass ferromagnetische Metalle wie beispielsweise Nickel mit ultrakurzen optischen Laserpulsen in weniger als einer Pikosekunde fast vollständig demagnetisiert werden können. Die Entdeckung dieser ultraschnellen Demagnetisierung löste eine neue Frage aus: Was passiert innerhalb einer so extrem kurzen Zeitskala mit dem Drehimpuls? Eine makroskopische Rotation gemäß dem Einstein-de-Haas-Effekt ist innerhalb einer so geringen Zeitspanne unmöglich. Die von Beaurepaire et al. [4] durchgeführten Messungen zeigen daher, dass unser Verständnis der Drehimpulsübertragung von der Drehung des Spins zur mechanischen Rotation lückenhaft sein muss. Seit Beobachtung der ultraschnellen Demagnetisierung analysierten viele Forscher diese Frage und stellten verschiedene Theorien auf, in welches Subsystem und auf welche Art der Drehimpuls übertragen werden könnte. Ein schlüssiges Bild gibt es jedoch bis heute nicht.

In dieser Dissertation kombinieren wir Femtosekunden-Laserpulse mit ultraschneller Elektronenbeugung, um direkt die ultraschnellen und ultrakleinen Veränderungen des atomaren Kristallgitters nach der Demagnetisierung zu untersuchen. Dazu verwenden wir Terahertz-komprimierte Elektronenpulse mit Femtosekunden Pulsdauer in einem Anrege-Abfrage-Experiment mit Femtosekunden Zeitauflösung. Der hierbei untersuchte Ferromagnet ist ein epitaktischer Nickel-Dünnsfilm, welcher in Zusammenarbeit mit Dr. Wolfgang Kreuzpaintner und Alexander Book hergestellt wird. Eine drehbare Magnetkonstruktion erlaubt in diesen Experimenten die Messung der Änderung der Kristallstruktur in Abhängigkeit von der ursprünglichen Magnetfeldrichtung. Durch Entdeckung von symmetriebrechenden Bragg-Reflex-Dynamik wird ein nahezu sofortiger, asymmetrischer Intensitätsverlust sichtbar, der nicht auf eine zufällige atomare Unordnung zurückzuführen ist.

Die Ergebnisse deuten daher auf eine rotierende atomare Bewegung des Kristallgitters in Form von chiralen Phononen hin. Es wird daher argumentiert, dass eine chirale Spin-Phonon-Anregung als Bindeglied zwischen dem Drehimpuls der anfänglich ausgerichteten Elektronenspins und der makroskopischen Rotation besteht. Numerische Simulationen, welche in Zusammenarbeit mit Prof. Dr. Ulrich Nowak und seinen Mitarbeitern entstanden sind, untermauern dieses Bild. Diese berechnen einen ultraschnellen Drehimpulstransfer nach unseren Vorstellungen, durch die Übertragung des Drehimpulses auf das Kristallgitter im Sinne eines mikroskopischen Einstein-de Haas Effekt. Die Ähnlichkeit der simulierten Ergebnisse mit der gemessenen Anisotropie der Bragg Reflexe in den Femtosekunden-Elektronen-Beutungs-Experimenten bekräftigt unsere Theorie, dass der durch Demagnetisierung erniedrigte Spin-Drehimpuls in chiralen Phononen zu finden ist, bevor auf viel langsameren Zeitskalen ein makroskopischer Einstein-de-Haas Effekt auftritt. Neben seiner Bedeutung für die Grundlagen der Physik können diese Erkenntnisse auch dazu beitragen, bessere Materialien für die Herstellung von neuen Datenspeichern mit volloptischer Schaltung zu finden.

# Abstract

In a ferromagnetic material, the alignment of the electron spins is associated with angular momentum. The Barnett-effect [1] and the Einstein-de-Haas effect [2, 3] demonstrate the conversion from mechanical motion to spin angular momentum and vice versa. In 1996 Beaurepaire et al. [4] discovered that ferromagnetic metals like nickel can be demagnetized with ultrashort optical laser pulses on a sub-picosecond timescale. Consequently, the discovery of this ultrafast demagnetization triggered a new question: what happens to the angular momentum within such an extremely short time scale? A macroscopic rotation according to the Einstein-de-Haas effect is impossible within such a small period of time. Hence, the measurements performed by Beaurepaire et al. [4] expose a missing piece of information in the understanding of angular momentum transfer from spin-flipping to mechanical rotation. Since this observation of ultrafast demagnetization, many researchers analyzed this question and came up with different theories to which subsystem and how the angular momentum might be transferred to. However, there is no conclusive picture, yet.

In this dissertation, we combine femtosecond laser pulses to trigger the demagnetization with ultrafast electron diffraction to directly observe ultrafast and ultraslow changes within the crystal lattice. For this purpose, we use terahertz-compressed electron pulses with femtosecond pulse duration in a pump-probe experiment with femtosecond time resolution. The investigated ferromagnet is an epitaxial nickel thin-film, which is produced in collaboration with Dr. Wolfgang Kreuzpaintner and Alexander Book. A rotatable magnet construction allows the measurement of changes in the crystal structure in dependence of the original magnetic field direction. With the discovery of symmetry-breaking Bragg spot dynamics an almost instantaneous, asymmetric loss of intensity is revealed that is unrelated to random atomic disorder. Therefore, the results suggest a rotating atomic motion of the crystal lattice in the form of chiral phonons. Thus, we argue that chiral spin-phonon excitation is a link between the angular momentum of

the initially aligned electron spins and the macroscopic rotation. Numerical simulations carried out in cooperation with Prof. Dr. Ulrich Nowak and coworkers support this picture. These calculate an ultrafast angular momentum transfer according to our ideas, by transferring the angular momentum to the crystal lattice in the sense of a microscopic Einstein-de Haas effect. The resemblance of the simulated and observed investigation of Bragg spot anisotropies in the ultrafast electron diffraction experiments reinforces our idea of chiral phonons carrying the spin angular momentum missing from demagnetization, before a macroscopic Einstein-de Haas effect occurs on much slower time scales. In addition to its importance for the fundamentals of physics, these findings can also help to find better materials for the development of new data storage devices with all-optical switching.

# List of publications

**S.R. Tauchert**, M. Volkov, D. Ehberger, D. Kazenwadel, M. Evers, H. Lange, A. Donges, A. Book, W. Kreuzpaintner, U. Nowak and P. Baum, *Polarized phonons carry the missing angular momentum in femtosecond demagnetization*, Nature submitted.



# Introduction

Today's world is crowded with information. Everyday, we produce and consume vast amounts of data by e.g using computers, browsing on the internet, listening to music, watching a movie and by just owning a smartphone. Most aspects of our modern life are somehow related to the usage of digital media. Consequently, the storage and processing of this incredible amount of data becomes paramount. Amongst the many technologies and physical principles behind them, magnetic devices like hard disks or magnetic random access memories stand out because they offer high information density at minimum energy for storage and switching [5]. Due to the increasing amount of data, faster storage and processing of the data is also desirable. However, applying faster magnetic fields for the manipulation of the bits leads to nondeterministic switching [6]. Hence, a subpicosecond demagnetization of the magnetic bits in combination with the manipulation of magnetic order would be an interesting approach for future data storage devices [7]. Therefore, the understanding of magnetic switching on atomic dimension may hold the key for next-generation applications and devices.

In 1996 Beaurepaire et al. [4] reported about the femtosecond demagnetization time of Ni thin films. In the following years, more of these rapid demagnetization times were found in various magnetic systems [7–10]. Although the mechanism behind this ultrafast demagnetization was thoroughly studied [4, 8–16] in order to understand the interaction between laser photons, electronic states, spin excitations and lattice dynamics, it is still under intense debate [8, 11, 17–23]. According to the Einstein-de Haas effect [2, 3] the demagnetization of a material involves a change in the alignment of the spin system, which ultimately results in the transfer of the angular momentum to mechanical rotation. However, the question where this dissipation of angular momentum remains within ultrashort timescale is still elusive. In the last years the idea of angular momentum of phonons came into consideration [24, 25] which lead to the idea of chiral phonons [26]. These chiral

phonons are relevant for the electron-phonon coupling in solids [27] and could fill the gap between ultrafast demagnetization and the Einstein-de Haas effect.

## 1.1 The Einstein-de-Haas effect

In 1915, Einstein and de Haas [2, 3] discovered the connection between the magnetism of a macroscopic object and the angular momentum conserved in electron spins of a ferromagnetic metal. They demonstrated this experimentally by measuring the mechanical torque caused by the reversal of magnetization within an iron cylinder. The change in the magnetic moment causes a free body to rotate, as depicted in Fig. 1.1(a). From this observation Einstein and de Haas inferred that the magnetism of matter is formed by the electron rotation around the nucleus and the electron spin. The atomic magnetic moment is described with  $M = \frac{e}{2\pi r/v} \pi r^2 = \frac{1}{2} e v r$ , where  $v$  is the velocity,  $r$  denotes the radius of the orbit around a nucleus and  $e$  is the electron charge. When we divide this atomic magnetic moment by the total angular momentum  $J = m v r$ , with  $m$  as the mass of the particle, we receive the gyromagnetic ratio [28]

$$\frac{M}{J} = g \frac{e}{2m}, \quad (1.1)$$

where  $g \approx 2$  is the Lande factor. By considering the individual contributions to the change of magnetization  $\Delta M$ , namely the spin contribution  $\Delta M^{spin} = \frac{e}{m} \Delta J^{spin}$  and the magnetic moment caused by the orbital motion of an electron around a certain axis  $\Delta M^{orb} = \frac{e}{2m} \Delta J^{orb}$ , we obtain  $\Delta M = \Delta M^{spin} + \Delta M^{orb}$ . The total angular momentum is assumed as

$$J^{tot} = J^{lattice} + J^{spin} + J^{orb}. \quad (1.2)$$

Due to energy conservation  $\Delta J = \Delta J^{spin} + \Delta J^{orb} = -\Delta J^{lattice}$  [28, 29], we obtain

$$\Delta M = g \frac{e}{2m} \Delta J. \quad (1.3)$$

The Einstein-de Haas effect was confirmed multiple times and subsequently used to determine  $g$  for different materials.

In the same year, Barnett [1] reported about the induced magnetization of an iron slab, which was rotated with an angular velocity  $\Omega$  as displayed in Fig. 1.1(b). This demonstrated that vice versa magnetization is induced by rotation and that the magnetization  $M$  is given by  $M = \chi \Omega / \gamma$ , with  $\gamma$  as the gyromagnetic ratio and  $\chi$  as magnetic susceptibility. Thus, the rotation of a body causes an effective magnetic field  $B_\Omega = \Omega / \gamma$ .

Both the Einstein-de-Haas effect and the Barnett effect therefore unambiguously connect the mechanical angular momentum of a rotating body with the angular momentum of a magnetic field.

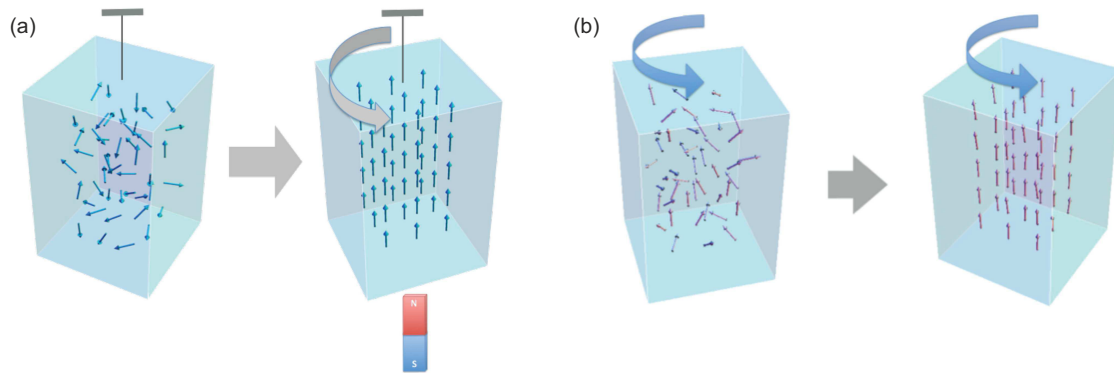


Figure 1.1: The Einstein-de Haas effect (a) outlines that the modulation of magnetization by applying an external field changes the magnetic angular momentum. This is observable by a mechanical rotation of the magnetized specimen. The Barnett effect (b) describes the induction of magnetization due to mechanical rotation. Graphic reproduced from Matsuo et al. [30].

## 1.2 Discovery of ultrafast laser-demagnetization

In order to rapidly switch the magnetic order in a material, researchers attempt to use ultrashort laser pulses which can nowadays have durations of few femtoseconds. Thus, the speed limit is solely determined by the physics of the material. The first experiments regarding ultrafast demagnetization were reported by Vaterlaus et al. [31] and resulted in the observation of a demagnetization time of 100 ps in ferromagnetic gadolinium. In 1996, Beaurepaire et al. [4] investigated the demagnetization dynamics of ferromagnetic Ni with 60-fs laser pulses and reported a decrease of magnetization within less than one picosecond, which is more than three orders of magnitude faster than the observations of Vaterlaus et al. [31]. The measurement of the transient remanent magneto-optical Kerr effect signal by Beaurepaire et al. [4] is reproduced in Fig. 1.2(a).

With this observation, a new question arose: what happens to the angular momentum after demagnetization? Beaurepaire et al. [4] tried to explain the mechanism of ultrafast demagnetization with a three-temperature model without regarding the angular momentum. This model assumes the electrons, the spins and the lattice as thermalized reservoirs for the exchange of energy. Each of these reservoirs is assigned a temperature  $T_e$ ,  $T_s$  and  $T_l$ . With this model, Beaurepaire et al. [4] could simulate the experimentally determined  $T_s$  and  $T_e$  as shown in Fig. 1.2(b,c). An initial energy transfer to the electron bath within  $\sim 100$  fs was inferred. Then, the majority and minority spins tend to homogenize due to scattering which results in an increase of  $T_s$  for 1 – 2 ps. Although the three-

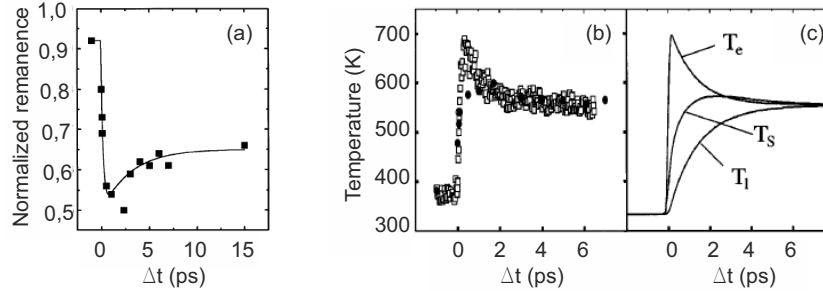


Figure 1.2: Observations of Beaurepaire et al. [4]. Image (a) depicts the ultrafast demagnetization of Ni. In (b) the measured temperatures for spins  $T_s$  (black dots) and electrons  $T_e$  (white squares) are plotted. The simulations with the three-temperature model are shown in (c) with the calculated temperatures  $T_e$ ,  $T_s$  and the temperature for the lattice  $T_l$ . Graphic reproduced from Beaurepaire et al. [4].

temperature model is in good agreement with the measurements, it neglects the conservation of angular momentum. Moreover, the measurements reproduced in Fig. 1.2 only determine  $T_s$  and  $T_e$ .

In 2018, Tengdin et al. [15] observed an absorption of laser energy in Ni within 20 fs by combining time- and angle-resolved photoemission with time-resolved transverse magneto-optical Kerr spectroscopy. Within this time span, enough energy is absorbed in the material such that it could go through the ferromagnetic-to-paramagnetic phase transition, but no significant demagnetization has been observed. Tengdin et al. [15] reported a fluence-independent demagnetization time of  $\sim 176$  fs. Beyond that, a fluence-dependent recovery time of the spin system on longer time scales was observed. For fluences below a critical fluence of  $F_c \approx 2.8$  mJ/cm<sup>2</sup>, a fast recovery of magnetization within  $\sim 500$  fs was detected, whereas for  $F > F_c$  the recovery time increases to  $\sim 70$  ps. It was inferred that  $F_c$  corresponds to a hot electron temperature approaching the Curie temperature ( $\sim 631$  K). For the case of fast recovery, Tengdin et al. [15] assumed a damping of magnons and for slow recovery a coupling to the phonons and the lattice over longer time scales than a picosecond. Yet, the phonons were not experimentally observed.

In 2020, Maldonado et al. [32] investigated the nonequilibrium energy transfer between electrons and phonons in Ni with ab initio calculations and diffuse ultrafast electron diffraction. In the experiment, the researchers inspected momentum resolved phonon occupation dynamics within the Brillouin zones in the first 4.9 ps after femtosecond laser illumination. They observed a strong deviation from a

thermalized occupation within this time-span. This was in agreement with the simulations of transient phonon excitation, assuming a transition of ferromagnetic to paramagnetic electron structure after 300 fs. Due to the calculations, the researchers inferred that within this time period the phonon population stays out of equilibrium [32]. Hence, a strong deviation from previously simulated phonon occupations was observed. Maldonado et al. [32] reported strong electron-phonon coupling as most effective channel for lattice relaxation and observed an interplay of the energy flow from the electronic system to the lattice within the investigated time-span. A dependence of the magnetic character of a ferromagnet like Ni and a change within lattice dynamics was concluded. The angular momentum conservation was not discussed.

In 2019, Dornes et al. [11] discussed the temporal gap between the quenching of the magnetization and the mechanical rotation. With time-resolved X-ray diffraction measurements the researchers investigated an in-plane magnetized iron film epitaxially grown on non-magnetic  $\text{MgAl}_2\text{O}_4$  with a capping layer on top to prevent oxidation. Dornes et al. [11] concentrated on the measurements of transverse and longitudinal strains and observed oscillations in the difference signal of the diffraction intensities measured in antiparallel magnetization directions. The measurements were in close relationship to the simulations of strain waves as a consequence from a mechanical torque caused by the demagnetization process. Thus, Dornes et al. [11] argued that the ultrafast loss of angular momentum within the spin system is followed by a transient volume torque density  $\boldsymbol{\tau} = -\gamma^{-1}d\mathbf{M}/dt$ , with  $\mathbf{M}$  as the initial magnetization,  $t$  as time and  $\gamma$  as the gyromagnetic ratio. Dornes et al. [11] inferred that the transfer of angular momentum happens within 200 fs and mentioned that 80% of the angular momentum is lost through ultrafast demagnetization getting transferred to the lattice with strain waves. The researchers connected this to an ultrafast Einstein-de Haas effect. This result gave strong evidence to the importance of the interaction between the electron spins and the lattice in ultrafast demagnetization, although earlier simulations predicted a time scale of  $\sim 300$  ps for the spin-lattice relaxation [33].

### 1.3 Where is the angular momentum?

Given the above account, the key question of this thesis is the fate of angular momentum after the first femtoseconds of successful demagnetization. A femtosecond time period is too brief to start a macroscopic rotation. Consequently, the angular momentum must be elsewhere. Until today, published literature offers no coherent explanation for this discrepancy between femtosecond demagnetization and transition of the angular momentum to mechanical rotation.

In this thesis, we therefore apply a novel experimental methodology to this

problem. Instead of X-rays, we utilize ultrafast electron diffraction to observe the reciprocal lattice and compare the measurements to simulated phonons. The ability of this experimental approach to track atomic positions directly in space and time as well as their disorder along various lattice directions provides direct insight into the atomistic origins of the fate of angular momentum after laser excitation.

Ultimately the understanding of the angular momentum transfer from quenched magnetization to macroscopic rotation can assist the search for next-generation materials for all-optical switching in devices.

## 1.4 Structure of this thesis

This work aims to investigate the angular momentum preservation after demagnetization of ferromagnetic Ni. Since we assume an angular momentum transfer to the lattice, we study the time-dependent intensity evolution of the crystal lattice of Ni after demagnetization. For this, we couple near-infrared femtosecond pulses illuminating the Ni layer with ultrafast electron diffraction to observe changes within the reciprocal lattice. The thesis is structured as follows:

**Chapter 2** introduces the idea of phonon angular momentum and its theoretical realization within the microscopic picture of angular momentum conservation, leading to the theoretical and experimental observation of chiral phonons. In this Chapter, we also describe the experimental concept that could visualize chiral lattice motion as possible angular momentum transfer channel. Moreover, we explain the theoretical background of electron diffraction and how it can observe changes in the crystal lattice.

**Chapter 3** deals with the experimental advances that are needed for the observation of time-dependent Bragg diffraction after ultrashort demagnetization. By inserting a construct of two diametrically magnetized ring magnets, we ensure an in-plane magnetization of the Ni layer after remagnetization and keep the trajectory of the electron beam aligned to the detector. In order to shorten the electron pulse duration, we apply terahertz compression and characterize the pulses with all-optical streaking. Electron pulses in the single-electron limit are applied to achieve the necessary angular and time resolutions.

**Chapter 4** explains the requirements for a Ni sample investigated with ultrafast electron diffraction and then describes the procedure of growing an epitaxial crystal on a Si membrane achieved in collaboration with Alexander Book and Dr. Wolfgang Kreuzpaintner from Technische Universität München. A pre-characterization of the sample reveals the thickness of the sputtered layers and the quality of the epitaxial growth.

**Chapter 5** presents the investigation of the epitaxial Ni layer with the ultra-

fast electron diffraction methods as developed in Chapter 3. The clear observation of the electron diffraction patterns confirms the epitaxial growth and maps the observed Bragg peaks to the different layers of the sputtered specimen. An investigation of time-resolved Bragg spot intensities shows decrease of intensity within the Ni peaks according to the Debye-Waller effect. We estimate the base temperature of the specimen using the Debye-Waller factor. In addition, we evaluate with Magneto-optical Faraday rotation measurements under similar excitation conditions, whether the base temperature of our thin-film is permanently below the Curie temperature. A time-dependent study of the Bragg spot position reveals no change of the lattice constants due to laser excitation. Moreover, we investigate the adjacent Si peaks and do not observe an intensity change beyond the noise level. The recorded angle-dependent intensity scan is in agreement with the X-ray measurements and confirms the epitaxy of the specimen. A fluence scan shows a linear increase of intensity loss with an increased fluence. A key result is the observation of symmetry-breaking Bragg spot dynamics. Here, we benefit from the in-plane magnetization of the specimen described in Chapter 3.3. With this special analysis we observe an asymmetry within the Ni Bragg spots, despite the symmetry of the crystal lattice. By rotating the initial magnetic field by  $90^\circ$ , the intensity of this anisotropy changes in direction, but not in intensity. We infer that this almost instantaneous intensity change reveals nonthermal phonon dynamics with a magnetic origin and implicates a localization of excitation by rotational phonon dynamics, i.e. chiral phonons.

**Chapter 6** summarizes our discussion with theory collaborators on the numerical simulations of such chiral phonons for an in-plane and out-of-plane magnetization of the Ni layer. The final implementation of the simulations is performed by Prof. Dr. Ulrich Nowak and coworkers at the Universität Konstanz. The results predict an observable anisotropy for in-plane magnetization. The strength of the simulated anisotropy is in accordance with the measurements presented in Chapter 5.

**Chapter 7** relates the obtained results to the ongoing debate about ultrafast demagnetization of the last two decades and describes the main approaches for explaining this phenomenon. In this chapter, the two main different mechanisms under discussion for ultrafast demagnetization are summarized. We line out how the idea of this thesis of transferring the angular momentum to the lattice fits within this discussion. Moreover, we explain the observed changes in Chapter 5.7 within the diffraction pattern introduced by in-plane rotational motion of the atoms in comparison to an attenuation according to Debye-Waller theory. This chapter concludes the thesis by summarizing the key results from the experiments and points out future improvements and experiments that could help to substantiate the theory for chiral phonons as transfer path between spin angular momentum

and specimen rotation.

# Experimental idea: chiral phonons with angular momentum

This chapter introduces the idea of rotational lattice motion in form of chiral phonons. Furthermore, it describes the experimental apparatus behind the pump-probe measurements (presented in Chapter 5) and our approach of visualizing the chiral phonon within Ni with ultrafast electron diffraction in dependence of a removable and rotatable in-plane magnetic field. Moreover, we give a short overview about electron diffraction physics and about the Debye-Waller effect, since it will be important for the analysis in Chapter 5.

The experiment is based on the idea that angular momentum gets transferred on ultrafast timescales to the crystal lattice in form of chiral phonons, that is, rotational atomic motions around their equilibrium positions. In order to observe these chiral phonons experimentally, we apply ultrafast electron diffraction and check for changes of the time-dependent Bragg diffraction as a function of the initial magnetization direction. The necessary experimental advances needed for its realization in case of Ni are described in Chapter 3.

## 2.1 Chiral phonons with angular momentum

Angular momentum is conserved [25] and the Einstein-de Haas [2, 3] experiment demonstrates the connection between mechanical rotation and an angular momentum change within electrons. However, the microscopic mechanism of angular momentum transfer from the spin to the phonon system and consequently the complete crystal remains elusive. Phonons emerge from vibrations of atoms around their equilibrium position [34]. Although traditionally phonons are assumed to have no angular momentum, in a system of interacting spins and phonons the an-

gular momentum conservation needs to be fulfilled [24]. In order to study phonons with rotational atomic vibrations and consequently with angular momentum Zhang and Niu [25] introduced the concept of phonon spin with

$$\mathbf{J}^{ph} = \sum_{l\alpha} \mathbf{u}_{l\alpha} \times \dot{\mathbf{u}}_{l\alpha}, \quad (2.1)$$

where  $\mathbf{u}_{l\alpha}$  describes the multiplication of the vector for the local shift of the  $\alpha$ th atom within the  $l$ th unit cell times the square root of mass  $\sqrt{m_\alpha}$ . In order to link this idea of phonon angular momentum with the Einstein-de Haas [2, 3] effect, the angular momentum of all atoms in a crystal lattice was phrased in the same publication from a microscopic perspective as

$$\mathbf{J}^{atom} = \sum_{l\alpha} (\mathbf{R}_{l\alpha} + \mathbf{u}_{l\alpha}) \times (\dot{\mathbf{R}}_{l\alpha} + \dot{\mathbf{u}}_{l\alpha}), \quad (2.2)$$

where  $\mathbf{R}_{l\alpha}$  denotes the multiplication of the equilibrium position of the  $\alpha$ th atom in the  $l$ th unit cell times  $\sqrt{m_\alpha}$ . In addition, the angular momentum of the lattice, corresponding to the mechanical rotation of the specimen [25, 29], was defined as

$$\mathbf{J}^{lattice} = \sum_{l\alpha} \mathbf{R}_{l\alpha} \times \dot{\mathbf{R}}_{l\alpha}. \quad (2.3)$$

Regarding, that all cross terms associated with  $\mathbf{u}$  and  $\dot{\mathbf{u}}$  become 0 in equilibrium and thus  $\mathbf{J}^{atom} = \mathbf{J}^{lattice} + \mathbf{J}^{ph}$ , Zhang and Niu [25] modified Eq. (1.2) to

$$\mathbf{J}^{tot} = \mathbf{J}^{lattice} + \mathbf{J}^{ph} + \mathbf{J}^{spin} + \mathbf{J}^{orb}, \quad (2.4)$$

with  $\mathbf{J}^{spin}$  the angular momentum of the spin and  $\mathbf{J}^{orb}$  the angular momentum of the orbital. With the assumption of an angular momentum  $\mathbf{J}^{ph} \neq 0$  due to spin-phonon interaction, this leads to

$$\Delta \mathbf{J}^{spin} + \Delta \mathbf{J}^{orb} = -\Delta \mathbf{J}^{lattice} - \Delta \mathbf{J}^{ph}, \quad (2.5)$$

considering a preservation of the total angular momentum. Zhang and Niu [25] investigated the phonon angular momentum for different lattice symmetries and revealed a tendency of increasing angular momenta for lattices with more sites per unit cell. Hence honeycomb lattices should provide an easier target to investigate the phonon angular momentum than triangle and square lattices. On top of that there have been calculations of phonons with definite chiralities despite a zero total phonon angular momentum for monolayer hexagonal systems with broken inversion symmetry [26, 28]. Hereby, chirality was defined in terms of the polarization of the phonons, emerging from circular vibrating sublattices. These predicted chiral

phonons were confirmed with transient infrared spectroscopy by Zhu et al. [27] in monolayer WSe<sub>2</sub>.

Subsequently, Garanin et al. [24] investigated the angular momentum transition from atomic spin to the orbital and spin angular momenta carried by phonons. It was reported that the angular momentum of phonons is divisible into two contributions and was characterized as  $\mathbf{L} = \mathbf{L}^{(1)} + \mathbf{L}^{(2)}$  [24]. One is the orbital angular momentum  $\mathbf{L}^{(1)}$ , describing the rotation around an origin as depicted in Fig. 2.1(a). The other is the spin angular momentum  $\mathbf{L}^{(2)}$ , which represents rotational movements of atoms around their equilibrium position as shown in Fig. 2.1(b). The studies of  $\mathbf{L}^{(1)}$  in this context revealed that the internal mechanical torque can be phrased as the rotation of the lattice and spin in the case of an existing spin-lattice coupling. The analysis of the phonon-spin angular momentum  $\mathbf{L}^{(2)}$  indicated that phonons have an angular momentum  $\hbar$ , which is needed for the conservation of the total angular momentum [24].

Until today, the chiral phonon has been predicted several times [35–39] and was experimentally observed [27, 40, 41]. Chiral phonons can be analyzed with the polarization of the phonons. However, chirality can also be interpreted in the presence of a magnetic field [41].

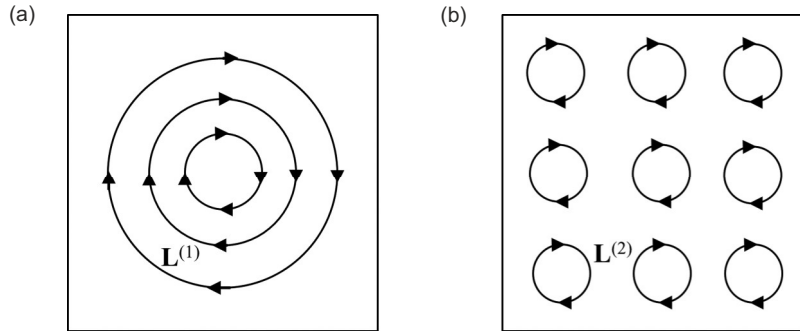


Figure 2.1: The two contributions of the phonon angular momentum split up into (a) rotation around an origin and (b) small rotational displacements around an equilibrium position. Graphic reproduced from Garanin et al. [24].

## 2.2 Ultrafast pump-probe diffraction with terahertz-compressed electron pulses

The setup used for the investigation of the ultra-thin Ni layer is displayed in Fig. 2.2. For the investigation of the ultra-thin Ni layer (see Chapter 5) we

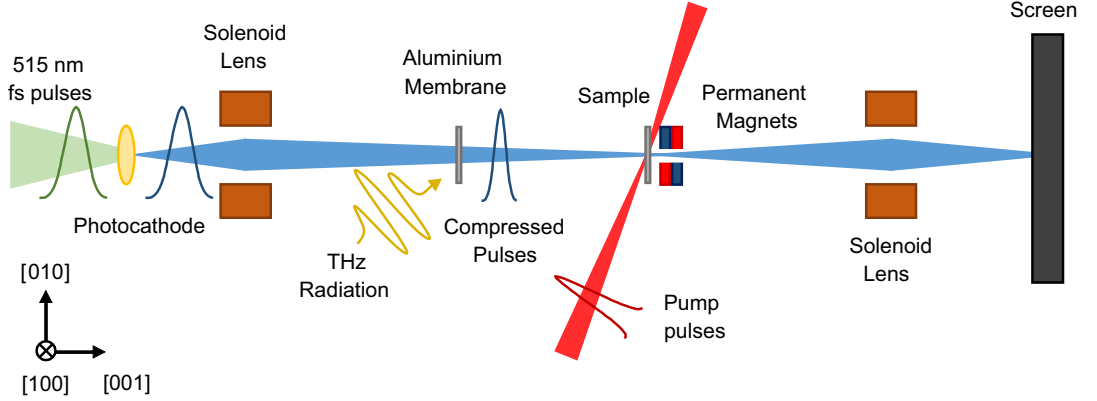


Figure 2.2: Illustration of the experimental setup. Permanent magnets (red and blue) induce an in-plane magnetization along a distinct axes. The specimen gets pumped with 95–fs laser pulses (red) to quench the magnetization of the Ni layer. Ultrashort electron pulses (blue) compressed with THz radiation (yellow) serve as probe to investigate the lattice dynamics.

design a pump-probe experiment with femtosecond pulses with a pulse duration of  $95 \pm 5$  fs as pump to induce the demagnetization of the Ni specimen (as described in Chapter 3.1). The pump beam is oriented in  $25 \pm 5^\circ$  to the Ni layer. We apply an excitation energy density (fluence) of  $3.6 \text{ mJ/cm}^2$  calculated by

$$F = \frac{1}{\cos(25^\circ)} \frac{2 \cdot 2 \ln(2)}{\pi \omega_{FWHM}^2} \cdot \frac{P_{avg}}{f_{rep}}, \quad (2.6)$$

where  $\omega_{FWHM}$  is the laser beam waist at full width at half maximum (FWHM),  $P_{avg}$  is the averaged laser power and  $f_{rep}$  is the laser repetition rate. This equals a pulse energy  $E_{pulse} = \frac{P_{avg}}{f_{rep}}$  of  $1.48 \mu\text{J}$ . With this configuration, Ni demagnetizes by  $\sim 50\%$  within  $\sim 250$  fs [42, 43]. As a probe, we apply femtosecond electron pulses generated by two-photon photoemission [44] (as mentioned in Chapter 3.2) and accelerate these with a kinetic energy of 70 keV [45]. Thus, we generate a de Broglie wavelength of

$$\lambda = \frac{hc}{\sqrt{2m_e c^2 E_{kin} + E_{kin}^2}} \approx 4.49 \text{ pm}, \quad (2.7)$$

where  $m_e$  is the electron mass,  $E_{kin}$  is the kinetic energy and  $h$  is the Planck constant. For electron pulse compression (as described in detail in Chapter 3.2) we use a laser-generated single-cycle terahertz field [46]. The compressed electron pulses are characterized with all-optical streaking using THz radiation as proposed

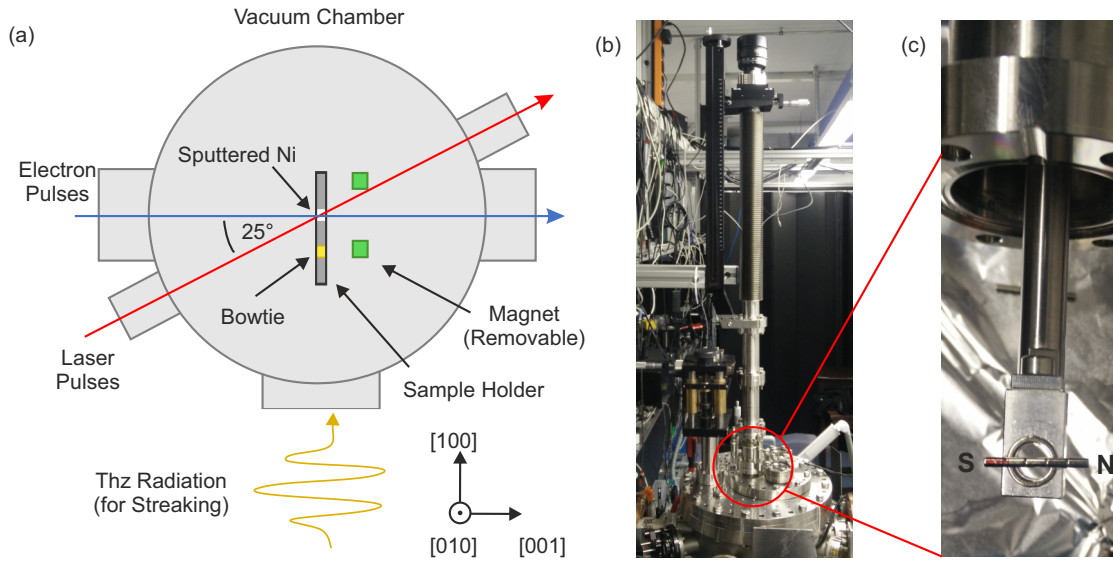


Figure 2.3: Images of the experimental setup. (a) Close up of the setup within the chamber. The optical laser beam (red) and the electron beam (blue) are overlapped at the Ni specimen (white). The magnetic construction (green) is placed behind the sample holder. A bowtie (yellow) is mounted on the sample holder to enable streaking measurements with THz radiation (yellow). (b) Manipulator on top of sample chamber to control the position and height of the magnetic construct. (c) Close up of the magnetic construction attached to the manipulator. A bar magnet is used to determine the orientation of the in-plane magnetic field.

by Kealhofer et al. [47], by using a THz driven bowtie resonator, mounted on the same sample holder as the Ni thin-film as shown in Fig. 2.3(a). An electron pulse duration of  $\sim 90$  fs is inferred. These electron pulses are focused on the Ni sample with a solenoid lens, which results in an electron beam size of  $60 \pm 5 \mu\text{m}$  at the thin-film's position, evaluated with knife-edge measurements. With the electron pulses, we investigate the lattice dynamics of the laser excited ferromagnetic thin-film. Since we analyze the transmitted electrons, it is important that the thickness of the investigated specimen is  $< 70$  nm as a compromise between diffraction strength and electron absorption. The 95-fs laser pulses are aligned at an angle of  $25^\circ$  to the electron pulses and the size of the laser beam on the specimen is about two times bigger than the electron beam.

The transmitted diffracted electrons are detected with a sensitive detector system (F416, TVIPS GmbH) equipped with a complementary metal-oxide-semiconductor (CMOS) sensor. A second solenoid lens installed after the specimen is

used to optimize the image of the diffraction pattern on the detector system.

In order to ensure an initial in-plane magnetization of the Ni layer we insert a combination of two permanent ring magnets in imminent proximity of  $2 \pm 1$  mm from the thin-films surface (as explained in Chapter 3.3). The permanent ring magnets are diametrically aligned to create an in-plane magnetization on the specimen. By using two equal magnets with opposing magnetic fields, we are able to compensate the off-axis deflection of the electron beam introduced by the front magnet. Thus, the electrons experience only slight deflection and distortion and the full diffraction pattern can be detected by the camera. Furthermore, the permanent magnet assembly is designed to be rotatable around the Ni[001]-direction, which equals the z-axis of the setup. Consequently, we are able to investigate the time-dependent diffraction pattern with an in-plane magnetization along the Ni[100] direction (x-axis) and the Ni[010] direction (y-axis). The image rotation introduced by all magnetic solenoid lenses is corrected with rotation transformations within the analysis procedure. The ability to turn the in-plane magnetization along these two crystallographic axes is crucial for our investigations, since it introduces an anisotropy between the Ni[100]-direction and the Ni[010]-direction of the crystal (as we will explain in Chapter 5.7 and Chapter 7.2). In order to be able to remove the rotatable, in-plane magnetic field from the beam line, we mount the magnetic construct on a manipulator as shown in Fig. 2.3(b). This manipulator enables us to move the magnetic construct  $40 \pm 10$  cm away from the sample holder. Thus, it is possible to record e.g. streaking measurements of the electron pulses without distortions of the electron beam [48]. To determine the direction of the in-plane magnetic field we use a commercial bar magnet, as depicted in Fig. 2.3(c). Hence, we can ensure an initial in-plane magnetization along a selected crystallographic axis of the specimen. In the experiments, we choose an initial in-plane magnetization along Ni[100] and along Ni[010].

## 2.3 Diffraction physics

Since ultrafast electron diffraction is our main tool for the investigation of an ultrafast angular momentum transfer to the crystal lattice, the following section describes the physics behind electron diffraction.

### Basics

Diffraction is a useful tool for analyzing crystal structures. Crystal lattices show a characteristic pattern when irradiated with a wavelength in range of their lattice constant. This diffraction pattern occurs due to interference of elastically scattered particles from the periodic potential distribution of the atoms within the lattice

[34]. In electron diffraction the investigated potential is the periodic electron density of the crystal lattice. A crystal can be defined as an amount of unit cells that periodically repeat in all three dimensions to form a lattice. This lattice can be described with  $\mathbf{R} = n_1\mathbf{a}_1 + n_2\mathbf{a}_2 + n_3\mathbf{a}_3$  where  $n_1, n_2, n_3 \in \mathbb{Z}$  and  $\mathbf{a}_1, \mathbf{a}_2, \mathbf{a}_3$  are the basis of the three dimensional lattice. When the difference of the wave vector of the incident radiation  $\mathbf{k}_i$  and the wave vector of the diffracted radiation  $\mathbf{k}_d$  is equivalent to the vector of the reciprocal lattice  $\mathbf{G}$ , constructive interference arises. This is described by the Laue equation

$$\mathbf{k}_i - \mathbf{k}_d = \mathbf{G}. \quad (2.8)$$

The reciprocal lattice vector is defined as  $\mathbf{G} = h\mathbf{b}_1 + k\mathbf{b}_2 + l\mathbf{b}_3$ , with a basis of  $\{\mathbf{b}_1, \mathbf{b}_2, \mathbf{b}_3\}$  and  $h, k, l \in \mathbb{Z}$  as so called Miller indices. It is connected to the real lattice with  $\mathbf{G} \cdot \mathbf{R} = 2\pi n$  with  $n \in \mathbb{N}$  and its length is defined as  $|\mathbf{G}| = n \frac{2\pi}{d_{hkl}}$  with  $d_{hkl}$  the spacing between the lattice planes perpendicular to  $|\mathbf{G}|$ . In case of elastic scattering the length of the vector for the incident electrons equals the length of the vector for the diffracted electrons  $|\mathbf{k}_i| = |\mathbf{k}_d| = k$ . When we define the angle between the incident electrons and the diffracted electrons as  $2\theta$ , we can convert Eq. (2.8) to Bragg's law

$$n\lambda = 2d_{hkl} \sin(\theta), \quad (2.9)$$

where  $\lambda$  describes the wavelength of the incident electron [34]. Constructive interference and consequently the peaks of the diffraction pattern result only, when Eq. (2.8) and Eq. (2.9) are satisfied. In case of elastic scattering, the Ewald's sphere is a helpful tool to illustrate Eq. (2.8). It is defined as a sphere within the reciprocal lattice. Its center is at the origin of the incoming wave vector  $\mathbf{k}_i$  and the spheres radius equals  $k$ . If the surface of the Ewald's sphere coincides with a lattice point of the reciprocal lattice, the Bragg condition shown in Eq. (2.9) is satisfied [49]. Consequently, we can observe constructive interference at these positions, with an intensity  $I_{hkl}$  of these Bragg spots is

$$I_{hkl} \propto |S_{hkl}^{stat}|^2, \quad (2.10)$$

with  $S_{hkl}^{stat}$  defined as the structure factor in case of elastic scattering [34]

$$S_{hkl}^{stat} = \int_V \rho(\mathbf{r}) \exp(-i\mathbf{G}\mathbf{r}) d^3r = \sum_j f_j \exp(-i\mathbf{G}\mathbf{r}_j). \quad (2.11)$$

In Eq. (2.11)  $V$  is the volume of the unit cell,  $\rho(\mathbf{r})$  is the scattering density, the indices  $h, k, l$  are the Miller indices of the reciprocal lattice vector  $\mathbf{G}$ . By establishing the scattering factor  $f_j$ , which is determined by the position of the atom  $\mathbf{r}_j$ , we can convert the integral to a sum over the base atoms of the lattice as

shown on the right side of Eq. (2.11). Hence, the position of the Bragg spots on a detector contains structural information about the form and the size of the unit cell. In case of a face-centered cubic system like Ni, with just one type of atom within the unit cell at the positions  $(000)$ ,  $(\frac{1}{2}\frac{1}{2}0)$ ,  $(\frac{1}{2}0\frac{1}{2})$  and  $(0\frac{1}{2}\frac{1}{2})$  Eq. (2.11), turns to

$$S_{hkl}^{stat} = f \cdot (1 + e^{-i\pi(h+k)} + e^{-i\pi(h+l)} + e^{-i\pi(k+l)}) = \begin{cases} 4f & \text{if all } h, k, l \text{ even or odd} \\ 0 & \text{else} \end{cases} \quad (2.12)$$

Hence, we can only observe Bragg spots where all Miller indices are equal or all are odd [34].

### Debye-Waller effect

In a real crystal lattice, the atoms are not in equilibrium. Thus, a part of the incident radiation is scattered inelastic, due to the vibration of the lattice. For atoms in non-equilibrium, the position of the atom  $\mathbf{r}_j$  in respect to its equilibrium position  $\mathbf{r}_{j,0}$  and the time-dependent atomic displacement of  $\mathbf{u}(t)$  is defined as  $\mathbf{r}_j = \mathbf{r}_{j,0} + \mathbf{u}(t)$  [34]. The structure factor is evaluated from the temporal mean value

$$\begin{aligned} \langle S_{hkl} \rangle_t &= \sum_j f_j \exp(-i\mathbf{G} \cdot \mathbf{r}_{j,0}) \langle \exp(-i\mathbf{G} \cdot \mathbf{u}(t)) \rangle_t \\ &\approx S_{hkl}^{stat} [1 - \langle i\mathbf{u}(t) \cdot \mathbf{G} \rangle_t - \frac{1}{2} \langle (\mathbf{u}(t) \cdot \mathbf{G})^2 \rangle_t] \end{aligned} \quad (2.13)$$

for small displacements of  $\mathbf{u}(t)$  and  $\mathbf{G} \cdot \mathbf{u} \ll 1$ . In case of thermal motion the atoms have an arbitrary movement. Thus,  $\mathbf{u}(t)$  and  $\mathbf{G}$  are uncorrelated which corresponds to  $\langle i\mathbf{u}(t) \cdot \mathbf{G} \rangle_t = 0$ . The second term of the approximation in Eq. (2.13) can be phrased as

$$\frac{1}{2} \langle (\mathbf{u}(t) \cdot \mathbf{G})^2 \rangle_t = \frac{1}{2} \langle u(t)^2 G^2 \cos^2(\phi) \rangle_t = \frac{1}{6} G^2 \langle u(t)^2 \rangle_t, \quad (2.14)$$

with  $\phi = \angle(\mathbf{u}, \mathbf{G})$  and  $u(t) = |\mathbf{u}(t)|$  and  $G = |\mathbf{G}|$ . With respect to Eq. (2.10) and a first order series expansion of an exponential function of Eq. (2.13), the intensity can be written as

$$I_{hkl} = I_0 \cdot \exp(-\frac{1}{3} G^2 \langle u(t)^2 \rangle_t), \quad (2.15)$$

with  $\exp(-\frac{1}{3} G^2 \langle u(t)^2 \rangle_t)$  as so called Debye-Waller factor [34]. Within the Debye-Waller factor  $u(t)$  describes the excitation of the lattice and thus the phonons.

These can be seen as a set of uncorrelated harmonic oscillators, with a mean potential energy  $\langle U \rangle_t$  of

$$\langle U \rangle_t = \frac{1}{2} m \omega^2 \langle u(t)^2 \rangle = \frac{3}{2} k_B T, \quad (2.16)$$

where  $T$  is the temperature,  $k_B$  the Boltzmann constant,  $\omega$  the frequency and  $m$  the mass of the oscillator. Hence, the intensity of the diffraction pattern regarding the temperature is revealed as

$$I_{hkl} = I_0 \cdot \exp\left(-\frac{k_B T}{m \omega^2} G^2\right). \quad (2.17)$$

Consequently, increasing temperatures and higher reciprocal lattice vectors lead to decreasing Bragg peak intensities.



## Necessary experimental advances

In order to be able to investigate the angular momentum transfer from the demagnetization process, a special configuration of the setup is crucial. The following sections describe the necessary improvements constructed for the beam-line to visualize the lattice dynamics of the reciprocal lattice for the ultrafast demagnetization process of Ni.

### 3.1 Optical pulse compression

The setup used for optical pulse compression is presented in Fig. 3.1. It is de-

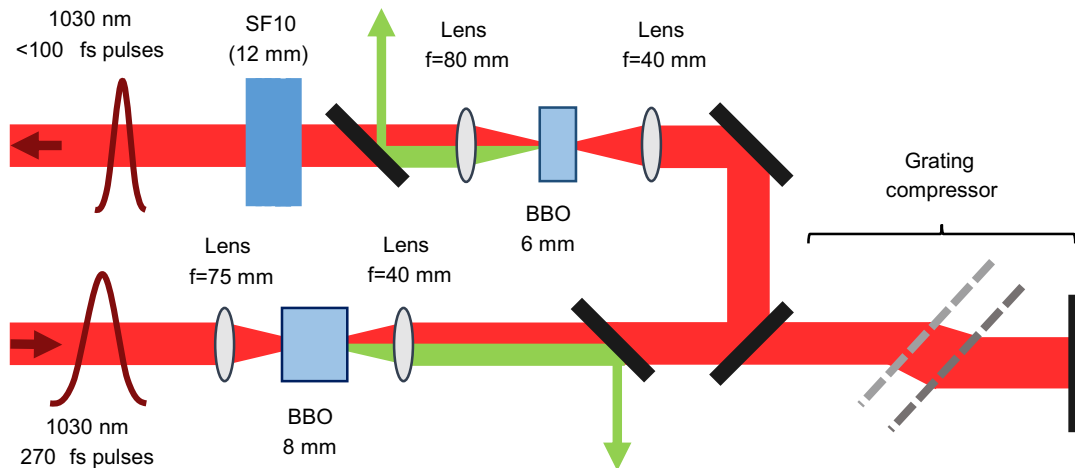


Figure 3.1: Optical pulse compression with two BBO-broadening-stages, a grating compressor and a block of SF10 to finally compress the beam.

signed by Dr. Bo-Han Chen. For optical excitation we use a commercial Yb:YAG laser source (Pharos, Light Conversion Inc.) with an applied repetition rate of 25 and 50 kHz at a center wavelength of 1030 nm with 270-fs pulses. To reduce the 270-fs-long optical pulse duration we apply two-stage-compression with self-defocusing bulk media as reported in [50]. In the first broadening-stage a  $f = 75$  mm lens is applied to focus the beam through a 8 mm thick beta-barium borate (BBO) crystal (Döhler Electrooptic GmbH). Cascaded second harmonic generation (SHG) lead to a broadening of the spectrum [50]. The spectrally broadened pulses from the BBO-stage optimized for 600 mW input power ( $12 \mu\text{J}$ ) at a repetition rate of 50 kHz are compressed by a grating pair (100 lines/mm, LSFSG-1000-3212-94, LightSmyth) at a distance of 2.5 mm. To further shorten the pulse a second BBO-stage is implemented with a  $f = 40$  mm lens focusing the beam through a 6 mm BBO-crystal (Döhler Electrooptic GmbH). Finally, a 12 mm thick block of high-refractive-index glass (SF10) is applied to compress the pulses by adding a group delay dispersion of  $\sim 1300 \text{ fs}^2$ . The resulting pulse duration is characterized with a second-harmonic-generation frequency-resolved optical-gating setup (SHG-FROG), by applying an  $80 \mu\text{m}$  thick BBO-crystal for second harmonic generation and a wavelength-calibrated spectrometer. Figure 3.2 depicts the results, revealing a full width at half maximum of  $95 \pm 5$  fs after

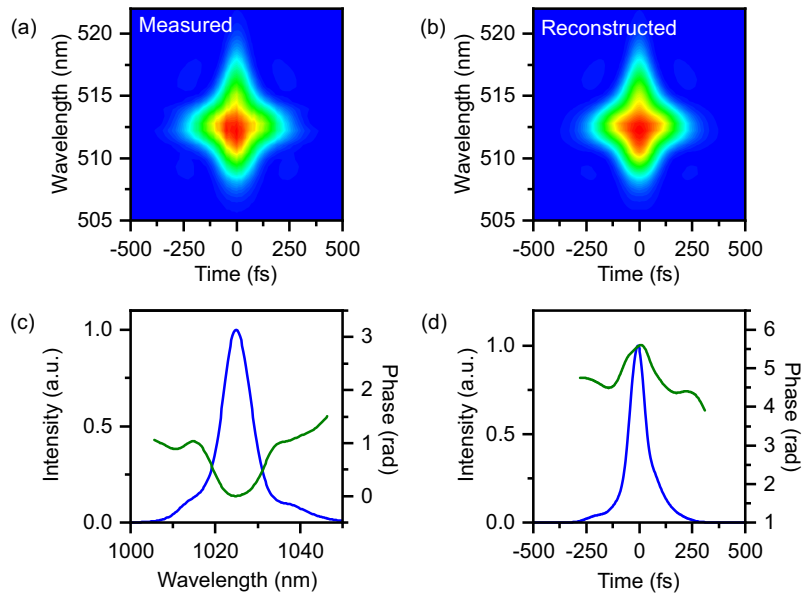


Figure 3.2: FROG measurements of the output pulses after two-stage compression. (a) Measured and (b) retrieved FROG traces. (0.27% FROG error on a  $256 \times 256$  grid) (c) Evaluated spectrum and spectral phase. (d) Retrieved pulse shape with temporal phase. The pulse duration is 93.0 fs.

two-stage-compression. To ensure a center wavelength of the pump-beam of solely 1030 nm, we add 515 nm high-reflection mirrors to filter out the residual radiation. The implementation and characterization of the optical compression is executed with help of Dr. Bo-Han Chen.

## 3.2 Ultrafast electron pulses and compression by THz radiation

### Generation of electron pulses

The electron pulses are generated with two-photon photoemission [51] by back-illumination of a photocathode within an electron gun. The sapphire cathode is coated with a 20 nm gold layer and illuminated with the second harmonic of 270-fs-long laser pulses from the Yb:YAG laser source at a repetition rate of 50 kHz and a center wavelength of 1030 nm. We enable the application of a high electrostatic acceleration field by a highly polished cathode surface with a gap-free contact between the sapphire and the metal construction. This allows a stable gun operation [44]. With a kinetic energy of 70 keV the electrons are accelerated across a range of 11 mm. We obviate space charge effects [52] by regulating the number of emitted electrons per pulse to  $< 20$ . Two solenoid lenses after the gun exit are used to control the size of the electron beam for an optimized electron diffraction and detection. The first magnetic solenoid lens is located 12 cm behind the gun exit and aligned collinear to the beam axis to minimize temporal aberrations [48]. The second lens is placed behind the sample and mainly used for imaging the diffraction pattern to a single-electron-sensitive camera system (F416, TVIPS GmbH) with a pixel size of  $15.6 \times 15.6 \mu\text{m}^2$  used for electron detection.<sup>1</sup>

In the experiments, the distances with respect to the electron gun are 0.9 m for the Ni specimen, 0.17 m for the first solenoid lens, 1.1 m for the second solenoid lens and 2.2 m for the camera. The experiments are performed with an electron beam diameter of  $60 \pm 5 \mu\text{m}$  (FWHM) at the specimen.

### Compression and characterization of ultrafast electron pulses with THz radiation

The pulse duration of the generated electron pulses is limited by the pulse duration of the laser source and has a finite duration after acceleration due to dispersion [52]. Without compression an electron pulse duration of 490-fs is measured with streaking metrology [47] at the Ni thin-film's position with 75 keV [45]. For

---

<sup>1</sup>The electron beam line was implemented by Dominik Ehberger and Kathrin Mohler. Further information about the electron beam line can be found in [45].

an improved pulse duration, THz single-cycle pulses are generated at a central frequency of 0.4 THz. We use the THz pulses for compression and characterization of the electron pulses and generate them in two different LiNbO<sub>3</sub> slabs with silicon prisms as output couplers [53].

The LiNbO<sub>3</sub> slab needed for generation of the THz pulses for electron compression uses a pump power of approximately 3 W at a repetition rate of 50 kHz. The intersection of the electron beam with the THz beam at approximately 90° at an ultra-thin Al mirror, placed 0.4 m behind the electron source, provides an only longitudinal momentum modulation of the electron beam [45, 54]. The 10–nm thin Al mirror is reinforced by a freestanding, 10–nm thick Si<sub>3</sub>N<sub>4</sub> membrane. In this configuration, the mirror is able to reflect the THz pulses, while transmitting the electron pulses. Furthermore, it enables velocity matching while excluding time-dependent deflection [54]. With the configuration displayed in Fig. 3.3(a) the trailing part of the propagating electron pulse gets accelerated at the intersection with the Al mirror, while the leading part gets slowed down as depicted in Fig. 3.3(b). Hereby, the mean velocity stays unmodified [45, 46]. Both parts of the pulse become compressed in time being shortest at the position of the temporal focus. At this point of shortest pulse duration, the sample is placed. The ultra-thin mirror ensures the time-dependent momentum modulation of the electron beam, since it enables the electrons to enter the electromagnetic field abruptly within a time interval below a cycle period [45, 56]. A cosine-shaped THz pulse is suitable for electron-pulse compression, since it yields a sine-like momentum modulation which is roughly linear around its zero-crossing [54]. Thus, we arrange the focusing conditions and the Gouy phase to transform the sine-like THz pulses created at the LiNbO<sub>3</sub> crystal into cosine-shaped pulses at the mirror surface [45]. Electron beams have a finite emittance and consequently a finite beam size. In our case, this finite diameter is roughly 1 mm [45]. Hence, it is much smaller at the intersecting region than the waist of the THz beam with 2.8 mm [45]. Therefore, we assume that the THz phase fronts at the mirror to be approximately planar, when they overlap with the electrons. In case of planar elements, there is a configuration of electron incidence angle  $\theta_e$  and THz incidence angle  $\theta_{THz}$  called (transverse) velocity-matching condition [56]. It is realized for  $\frac{c}{\sin(\theta_{THz})} = \frac{v_e}{\sin(\theta_e)}$ , where  $c$  is the speed of light and  $v_e$  is the electron velocity [54]. In this condition, the phase velocity of the THz pulses equals the velocity of the electron pulses along the surface of the ultra-thin mirror. Since this condition occurs at our setup without time-dependent deflections [54], the induced net modulation is only longitudinal [45]. Thus, by setting the aluminium foil in an angle of  $\theta_{THz} \approx 65^\circ$  suitable for velocity-matching, we receive compressed and non-tilted electron pulses at the temporal focus.

The characterization of the electron pulse duration is executed at the temporal

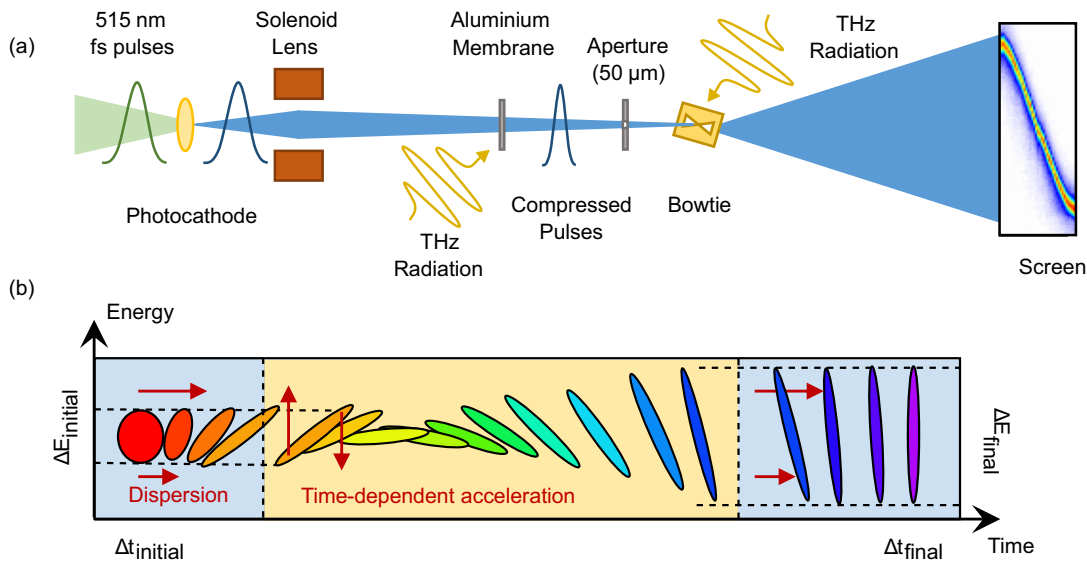


Figure 3.3: Setup for electron compression and characterization, implemented by Dominik Ehberger. (a) The electron pulse propagates to the Al mirror, where the THz wave intersects with the electron beam. Temporal characterization is enabled via streaking metrology. The optical oscilloscope maps electron arrival times to positions of the screen. (b) Energy-time phase-space picture of the electron beam dispersion and time-dependent compression with a cosine-shaped terahertz pulse. Figure 3.3(b) redrawn from Gliserin et al. [55].

focus with THz streaking metrology [45] as depicted in Fig. 3.3(a). A pump power of approximately 12 W at a repetition rate of 50 kHz is applied to the LiNbO<sub>3</sub> crystal to generate THz radiation. With this radiation a butterfly-shaped copper resonator with 400 μm width, 400 μm height, 56 μm gap width and 80 μm gap height is used as streaking element. This streaking element is needed to deflect the electrons out of plane in dependence to their arrival time [47], mapping electron arrival time onto positions on the screen as shown in Fig. 3.4(b) [46, 47]. The butterfly shaped resonator is located in the same position as the Ni specimen during diffraction experiments. During characterization, we use a solenoid lens to focus the electrons to this position. To improve streaking resolution a 50 μm aperture is applied. To exclude temporal distortions, no electro-optical elements are installed between compression and streaking stage [57]. The obtained streaking profile is a convolution of the electron pulse duration and the transverse beam profile. The electron pulse compression and characterization in its current design

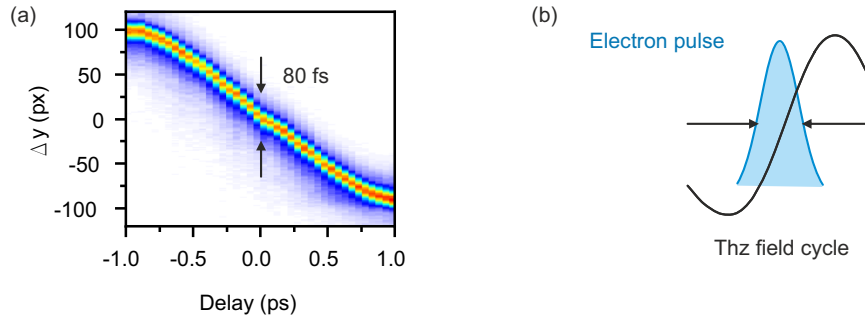


Figure 3.4: Visualization of streaking. (a) THz streaking data used for temporal characterization of the electron pulses after all-optical compression. (b) Schematics of the streaking of an electron pulse (blue) with a single THz fields cycle (black) for mapping time to position.

was implemented by Ehberger et al. and previously described in [45].

For the experiments presented in Chapter 5 electron pulse durations of  $< 130$  fs,  $< 120$  fs,  $< 76$  fs and  $< 80$  fs are observed for different diffraction scans. These values represent upper limits due to streaking resolution. Moreover, in contrast to [45], the values are a convolution of the electron pulse duration and the transverse beam profile. The streaking profile for the characterization of the  $< 80$  fs long electron pulse is depicted in Fig. 3.4(a).

### 3.3 Control of magnetization and remagnetization

The main challenge with the implementation of a magnetic field within the setup is to avoid the permanent deflection of the electron beam, while selecting a field strength high enough to ensure the desired configuration. Hence, the installation of a magnetic field needs to be planned thoroughly.

Two different configurations of the magnetic field are investigated to control the magnetization within an ultra-thin Ni sample: an out-of-plane configuration and an in-plane configuration. Superconducting quantum interference device (SQUID) measurements of a similar produced sample<sup>2</sup> revealed a saturation of  $\sim 35$  mT for the out-of-plane magnetization of the Ni slab and a saturation of  $\sim 4$  mT for an in-plane magnetization as depicted in Fig. 3.5(a) and Fig. 3.5(b). The wide discrepancy between the magnetic fields needed to change from in-plane to out-of-plane magnetization can be explained by the shape anisotropy of the ultra-thin specimen [58]. The measurements are performed at 300 K with a superconducting

<sup>2</sup>Measurements performed by Ilona Wimmer at Universität Konstanz.

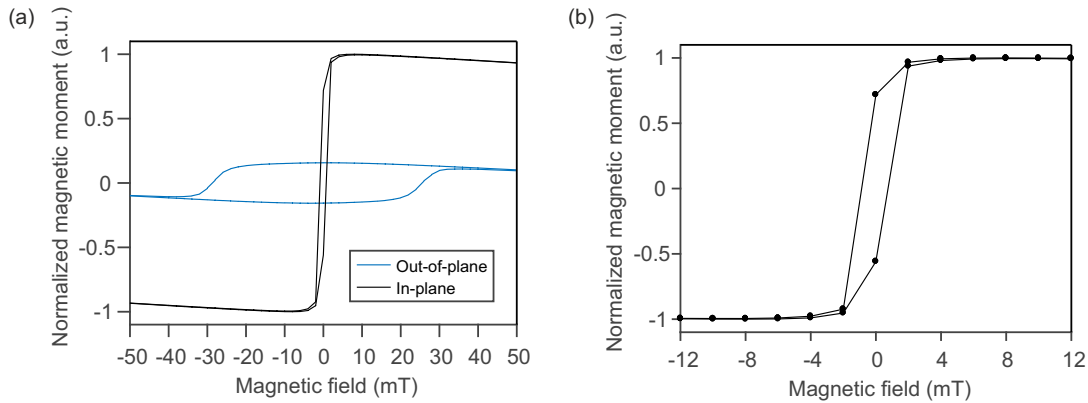


Figure 3.5: Hysteresis curves revealed by SQUID measurements for (a) in-plane and out-of-plane magnetization of the sputtered Ni thin-film. (b) Close up of the in-plane SQUID measurement. Measurements performed by Ilona Wimmer at Universität Konstanz.

quantum interference device (rf SQUID MPMS XL5, Quantum Design). The magnetic field applied ranges from  $-60$  mT to  $60$  mT. To fine resolve the hysteresis curve a step size of  $2$  mT is chosen from  $-40$  mT to  $40$  mT.

For the out-of-plane magnetization of the membrane a commercial NdFeB ring magnet (inner diameter  $10$  mm, outer diameter  $14$  mm, length  $4$  mm) installed on a manipulator behind the membrane (see Fig. 3.6(a)) is suitable.

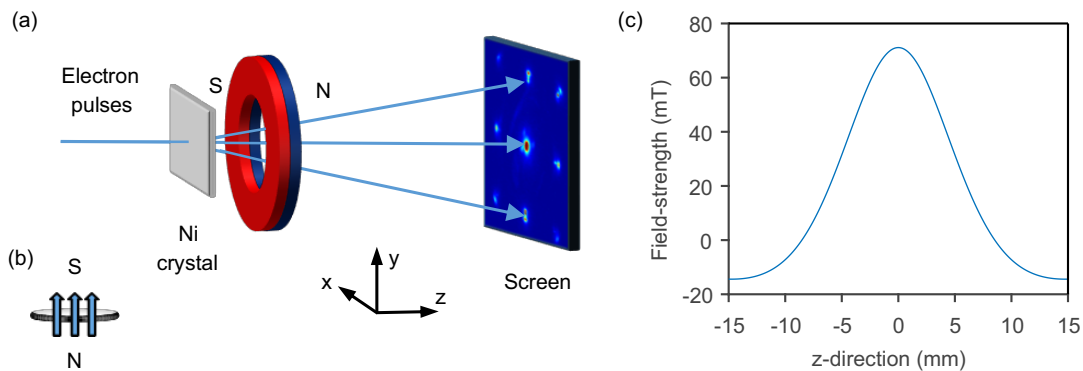


Figure 3.6: Realization of the out-of-plane magnetization. (a) The out-of-plane magnetization shown in (b) can be achieved with a commercial ring magnet placed behind the specimen. (c) Simulations of the magnetic field-strength of the commercial NdFeB ring magnet along the  $z$ -axis of the experiment.

To estimate the magnetic field strength the installed magnet can be approximated as magnetic lens. Simulations in Fig. 3.6(c) indicate a magnetic field suitable for out-of-plane magnetization within 5 mm distance of the center of the ring magnet. However, in this configuration all Bragg spots have the same orientation to the magnetic field and are thus exposed equally to the magnetization change of the demagnetization. The simulations presented in Chapter 6.3 confirm that such a magnetic field applied is not feasible for the observation of a located plane of phonon excitation.

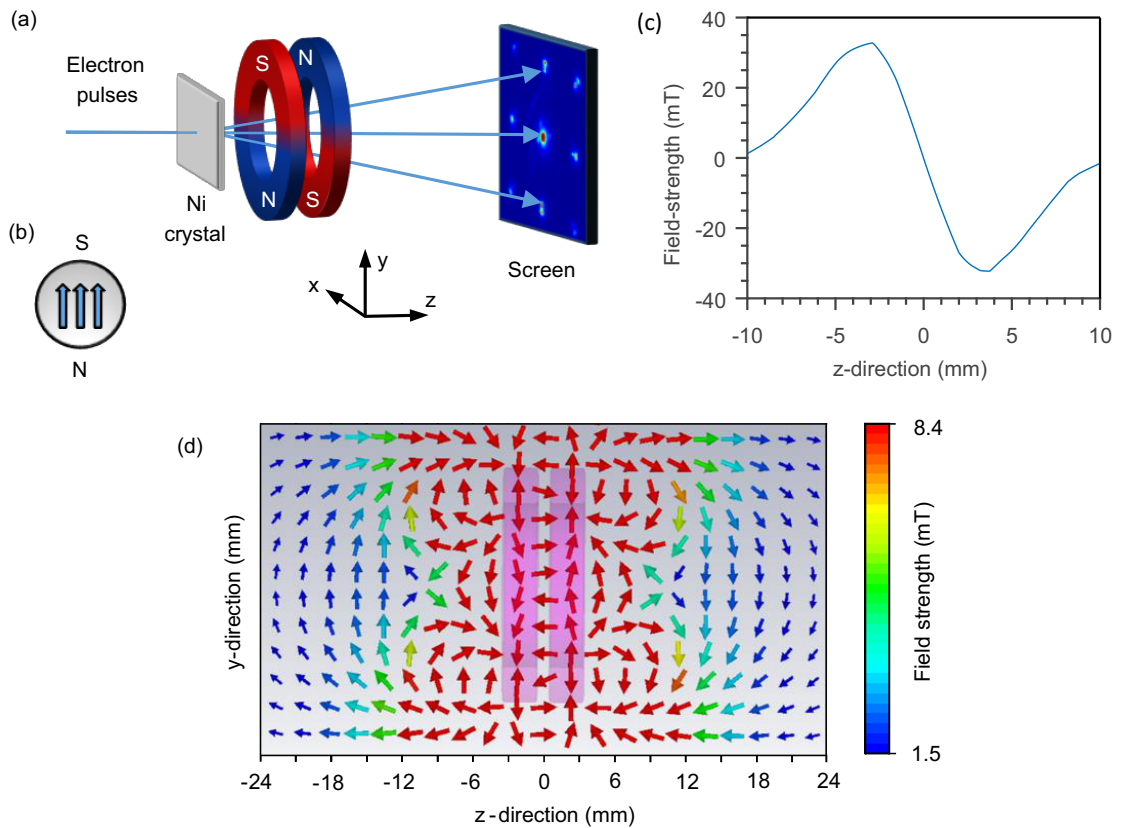


Figure 3.7: Realization of the in-plane magnetization. (a) Experimental setup with two diametrically magnetized ring magnets combined placed behind the specimen for realization of an in-plane magnetization of the thin-film depicted in (b). (c) Simulation of the magnetic field distribution along the trajectory of the electron beam. (d) Visualization of the magnetic field lines along the profile of the double-ring-magnet confirm an in-plane magnetization within close proximity to the magnet.

For the observation of a magnetic anisotropy an in-plane magnetization of the sample is essential. A normal bar magnet would be feasible for providing an in-plane magnetization. However, the magnetic field created by the bar magnet would deflect the electron beam and it would not be observable on the detector. Consequently, we install a construct of two contrary diametrically magnetized NdFeB ring magnets as shown in Fig. 3.7(a), with 7 mm inner diameter, 10 mm outer diameter, 3 mm length and a remanent magnetization of 1.32 – 1.37 T. The simulations confirm an in-plane magnetization at the membrane with only a slight deflection of the electron beam along the trajectory as observed in Fig. 3.7(c,d). The simulations are performed with CST STUDIO SUITE 2017. Since the path of the electron trajectory was not visualized in the simulation plot of the field lines, we extract here the visualization of the field provided by the software and estimate the distance of the z-axis with the size of the ring magnets for Fig. 3.7(d).



# Chapter 4

## Sample preparation

### 4.1 Requirements for electron diffraction

In order to perform ultrafast electron diffraction experiments and analyze the time-dependent development of Bragg spots after laser excitation we need an ultra-thin single-crystalline Ni specimen. The thickness of the specimen as a whole needs to be  $< 100$  nm for electron beam probing in transmission. Moreover, the single-crystallinity is required for the analysis of specific Bragg spots. Thus, we collaborate with Alexander Book and Dr. Wolfgang Kreuzpaintner from the Technische Universität München to produce a sample fitting those conditions. The following section describes the procedure for manufacturing the specimen and a first, static characterization, performed by Alexander Book.

### 4.2 Sample preparation and characterization

The specimen is produced by sputtering a nominally 22 nm thick Ni layer on a single-crystalline Si(100) transmission electron microscopy (TEM) grid with a diameter of 3 mm and 9 membrane windows with a 35 nm single-crystalline Si(100) membrane (Plano GmbH). The windows have a size of  $100 \times 100 \mu\text{m}^2$ , except for a special window used for orientation of the TEM grid with a size of  $350 \times 100 \mu\text{m}^2$  and are aligned in a square. Prior to the sputtering procedure, the grid is cleaned by using consecutively a bath of acetone, ethanol and by rinsing it with distilled water, before removing the native oxide layer of the Si grid by dipping the grid in 5% hydrofluoric acid for 15 s. Afterwards, the grid is washed with deionized water and blown dry with laboratory grade clean air, before it is instantly placed into a thin-film deposition system as described in [59, 60]. Thus, a hydrogen terminated silicon surface suitable for the epitaxial growth of the Ni layer is produced [61–63].

For not ultrafast electron diffraction connected measurements, we simultaneously prepare a  $20 \times 20$  mm Si wafer (CrysTec, 99.999% pure) with exactly the same procedure.

To grow the Ni thin-film direct current (DC) magnetron sputtering is performed in a thin-film deposition system. For the sputtering procedure, one of the 2" sputter guns is mounted with a Cu (6.3 mm thick, 99.99% pure) target, while for the second sputter gun a Ni (1.4 mm thick, 99.99% pure) target is used. The sputter targets are positioned in a distance of approximately 11 cm normal to the surface of the grid and a deposition-shutter is placed in between to be able to control the sputtered film thickness in dependence of the deposition time. Before the sputtering process is initiated, the system is pumped down to a base pressure of  $3 \times 10^{-8}$  mbar and the grid stabilizes at 273 K for 1 h. Potential impurities on the sputtering targets can be excluded, due to a 10 min long pre-sputtering with a closed deposition shutter. The growing procedure follows metal-metal epitaxy on silicon [64–66]. First, a 6 nm Cu seed layer is sputtered at an ultra-high purity (7N) Ar working gas pressure of  $2.5 \times 10^{-3}$  mbar. With a selected sputtering power of 50 W, this provides a deposition rate of  $0.5 \text{ \AA}/s$ . Then, the Ni layer is sputtered on top of the Cu seed layer. The working gas pressure for the sputtering of the Ni layer is  $4.0 \times 10^{-3}$  mbar and the DC sputtering power is 50 W, which leads to a deposition rate of  $0.41 \text{ \AA}/s$ .

Both, the preparation of the hydrogen terminated Si surface and the growing of the thin-film layer is executed at the Technische Universität München. The thin-film growing procedure is performed and evaluated with X-ray characterization by Alexander Book with supervision of Dr. Wolfgang Kreuzpaintner based on [61].

### 4.3 Pre-characterization and proof of epitaxial growth

The pre-characterization is performed on a substrate, prepared simultaneously and under the same conditions, since the grids were too fragile and small for the laboratory instruments used. For determination of the layer and crystal structure X-ray reflectometry (XRR) and diffraction (XRD) scans are performed by Alexander Book. The out-of-plane rocking curves are measured with a two-circle X-ray diffractometer (D5000, Siemens GmbH) with parallel beam optics and  $\text{Cu}_{K\alpha}$  ( $\lambda = 1.5419 \text{ \AA}$ ) source in a  $\theta - 2\theta$  scattering geometry. The instrument resolution is measured by the out-of-plane rocking-scan of the Si(400) peak and determined to be  $0.023^\circ$  (FWHM).

The XRR measurements are used to investigate the actual structure of the deposited layers. In these measurements, the reflectivity of the sample is scanned

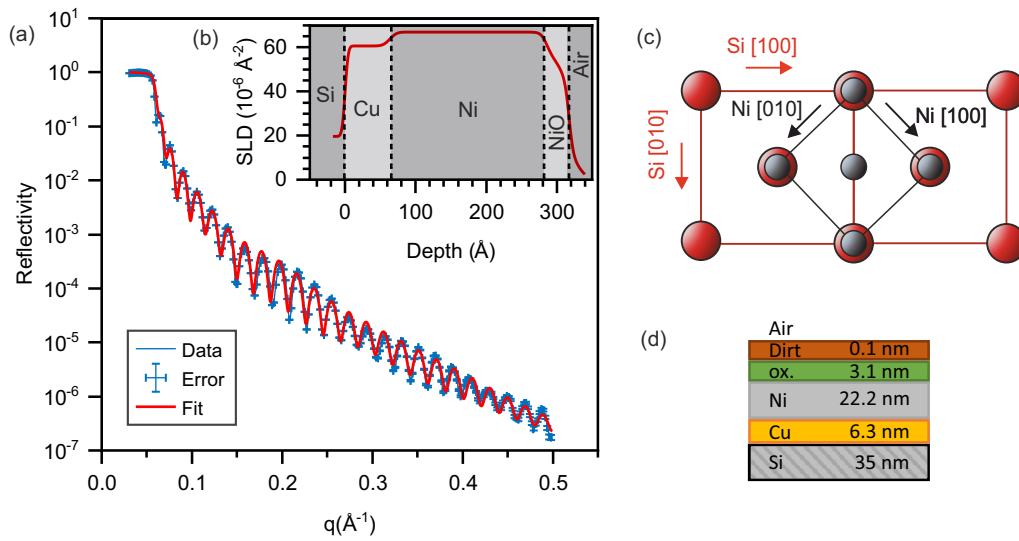


Figure 4.1: (a) XRR measurement with fit of the acquired data using a four-layer model and (b) the scattering length density profile used for fitting. Data for both is measured and evaluated by Alexander Book from Technische Universität München. (c) Epitaxial relationship of the Ni thin-film to the Si(100) substrate. The Ni lattice grows  $45^\circ$  rotated to the Si layer. Figure 4.1(c) is inspired by Kreuzpaintner et al. [61]. The Cu seed layer in intermediate position and the mismatch between the grids is not depicted to keep clarity. (d) Sequence of layers within the specimen. The value for Si differs from Table 4.1, since the membranes are too small and fragile for the XRR measurements.

as a function of wave vector transfer  $q = 4\pi/\lambda \sin(\theta)$ , where  $\theta$  is the angle of the incidence with respect to the sample's surface. Hereby, the incident X-ray get reflected at the thin-film interfaces and interference at these interfaces produce the prominent oscillations, called Kiessig fringes [67], in the reflectivity profile. For these measurements the surface of the sputtered substrate is aligned by optimizing the reflected intensity. The data obtained is analyzed using the GenX 3.0.0 software package [68] and fitted with a logarithmic figure of merit  $\text{FOM} \sim \sum |\log R_{fit} - \log R_{meas}|$ , where  $R_{meas}$  is the measured reflectivity and  $R_{fit}$  is the fit of the measurement<sup>1</sup>. The acquired XRR data fitted with a four-layer model is depicted in Fig. 4.1(a). The associated scattering length density profile, which describes the sample's structure, is presented in Fig. 4.1(b). The parameters of the best fit are presented in Table 4.1. From the XRR measurements we can determine the specimens' structure as  $\text{NiO}_{x_{3.1 \text{ nm}}}/\text{Ni}_{22.2 \text{ nm}}/\text{Cu}_{6.3 \text{ nm}}/\text{Si}_{\text{Substrate}}$ , where NiOx

<sup>1</sup>Fit and evaluation performed by Alexander Book at Technische Universität München.

Layer	Thickness [Å]	Density [g/cm <sup>3</sup> ]	rms Roughness [Å]
Dirt	1 ± 2.1	N.A.	4.5 ± 2.9
NiO	31 ± 3.6	5.11 ± 0.19	17.4 ± 2.4
Ni	222 ± 5.5	9.32 ± 0.23	6.4 ± 1.1
Cu	63 ± 3.9	8.43 ± 0.27	7.7 ± 2.3
Si	∞	2.32 ± 0.12	3.5 ± 0.1

Table 4.1: Best fit parameters for the XRR intensities. Data is measured and fitted by Alexander Book from Technische Universität München.

describes a natural 3.1 nm nickel oxide layer emerging at the Ni surface after the exposition of the sputtered thin-film to air.

For determination of the crystal quality out-of-plane XRD rocking scans are performed, to estimate the mosaic spread<sup>2</sup>. The Gaussian shaped rocking-scan is analyzed with its standard deviation  $\sigma = \frac{FWHM}{2\sqrt{2\ln 2}}$  [69], with FWHM as full-width-at-half-maximum. The size of the crystallites equals the coherence length  $L$  and can be revealed with the Scherrer formula [70]  $B(2\theta) = \frac{0.94\lambda}{L \cdot \cos(\theta)}$ , where  $B(2\theta)$  is the FWHM in radians of the diffraction peak,  $\theta$  is the angular peak position in radians and  $\lambda$  is the wavelength of the radiation applied. For the out-of-plane XRD analysis the substrate is aligned with the out-of-plane reflection of the Si(400) peak as a reference for the crystalline direction of the sputtered Cu and Ni layers. The out-of-plane XRD measurements are depicted in Fig. 4.2(a-b). The intensity at  $2\theta \approx 50.53^\circ$  (see Fig. 4.2(a)) with a rocking-curve width of  $\omega_{FWHM}^{Cu} = 5.6^\circ \pm 0.1$  (see Fig. 4.2(b)) belongs to the Cu(200) reflection and the intensity at  $2\theta \approx 52.13^\circ$  (see Fig. 4.2(a)) with a rocking-curve width of  $\omega_{FWHM}^{Ni} = 4.4^\circ \pm 0.1$  (see Fig. 4.2(b)) to the Ni(200) reflection. The absence of the Cu(111) and the Ni(111) intensities in Fig. 4.2(a) affirms the epitaxial growth. The FWHM of the intensities are in agreement with literature values [61, 64, 69]. Using the Scherrer formula, a coherence length of  $L(100)_{Cu} = 159.5 \pm 2.7 \text{ \AA}$  and  $L(100)_{Ni} = 221.1 \pm 2.7 \text{ \AA}$  can be inferred from the out-of-plane XRD scans. Since these values are in relationship to the layer thicknesses determined with the XRR measurements, we can assume that there is no epitaxial fracture within the layers in this direction. Moreover, the curves of the rocking scans in Fig. 4.2(b) reveal no splitting into multiple peaks [61], which further confirms that there are no defects along the growth direction.

<sup>2</sup>Scans performed by Alexander Book at Technische Universität München.

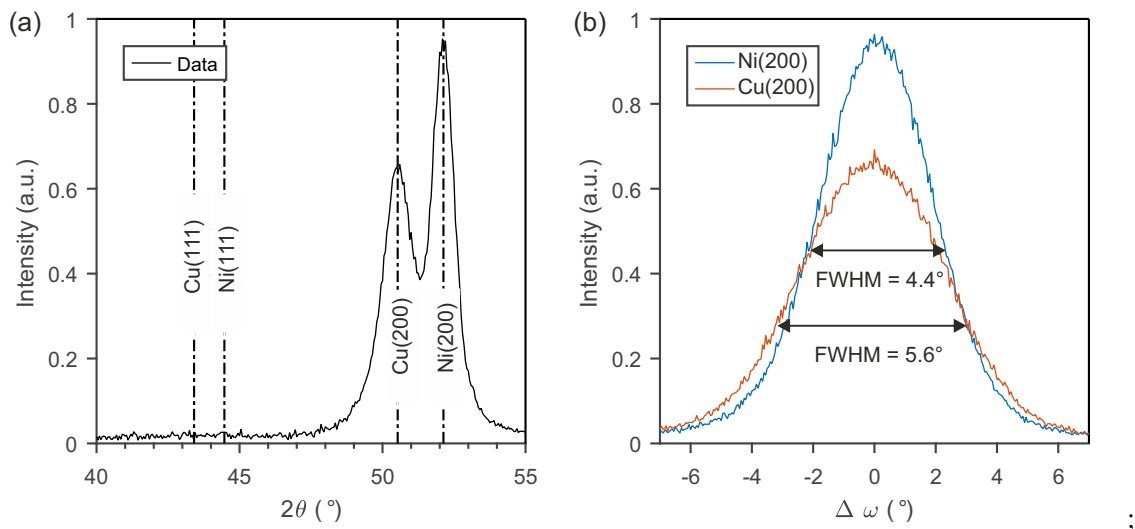


Figure 4.2: Out-of-plane XRD scans. (a) The intensities observed at  $2\theta \approx 50.53^\circ$  and  $2\theta \approx 52.13^\circ$  correspond to the Cu(200) and Ni(200) peak. (b) Close up of the Ni(200) and Cu(200) rocking-scans. Data for both graphs measured and evaluated by Alexander Book.



# Femtosecond electron diffraction of demagnetization dynamics in nickel

This section sums up the data analysis of the epitaxial Ni layer with a few-electron configuration in the ultrafast electron diffraction beamline described in Chapter 2.2 and Chapter 3. In the following sections, all diffraction pattern presented and data analyzed is recorded at an angle adjusted for the optimization of the Ni Bragg spots<sup>1</sup>.

## 5.1 Static electron diffraction characterizations

Before conducting ultrafast experiments, it is essential to confirm and calibrate the diffraction as obtained with the same electron beam used later for time-resolved investigations. The various layers of the specimen and in particular a single-crystalline Ni layer with epitaxial orientation are observable in the electron diffraction pattern. An analysis with the ultrafast electron diffraction beam line as described in Chapter 2.2 but without laser excitation, without compressed pulses and without a magnetic field applied to the sample reveals a diffraction pattern as depicted in Fig. 5.1(a). Within the pattern, the desired Ni spots are clearly observable. However, also peaks apart from Ni are detected. As shown in the zoomed region of interest in Fig. 5.1(b-c), up to three different kinds of Bragg spots can appear in dependence of the specimens' angle with respect to the electron beam. The parallel alignment of the Si[110]-direction with the Ni[100]-direction pre-

---

<sup>1</sup>Technical problems with the goniometer and drifts of the electron beam prevented the adjustment of exactly the same diffraction pattern in every scan. This results in a different intensity within some of the Ni peaks and the appearance of different Si and NiO<sub>x</sub> peaks. Thus, not all the peaks shown in this section can be observed in Fig. 5.1.

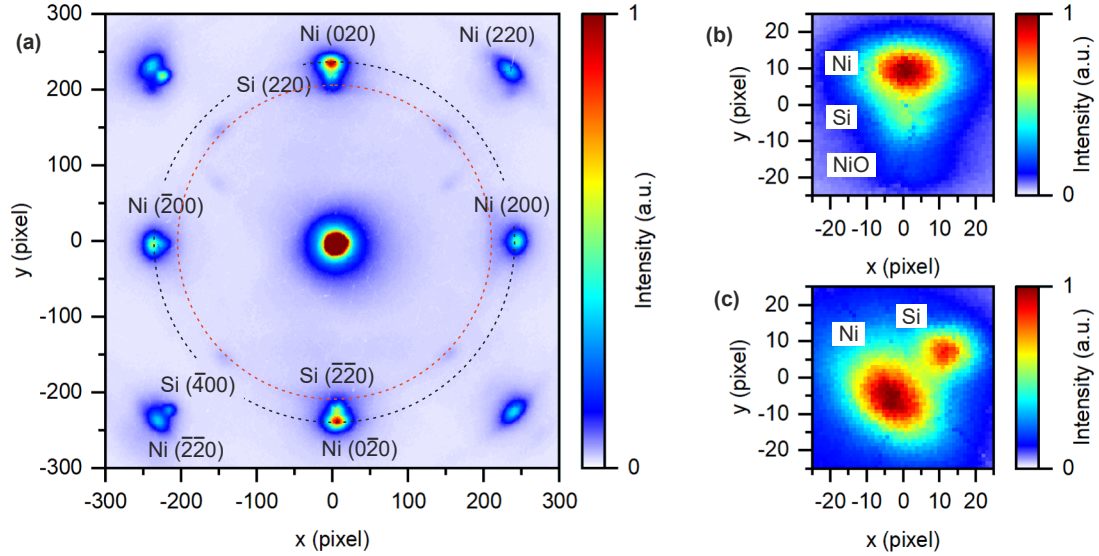


Figure 5.1: Images of the acquired diffraction pattern before probing. In (a) the complete diffraction pattern is shown with labeled Bragg spots for Ni and Si. The assignment of the Ni peaks differs from the Si peaks due to a  $45^\circ$  rotation of the lattices as described in Table 5.1. The black circle marks the Ni $\{200\}$  and Ni $\{020\}$  peaks. The red circle marks the NiO $_x$  peaks. (b,c) show a close up of two selected peaks. In (b) Ni, Si and NiO $_x$  Bragg spots are observable. In (c) only a Ni spot and a Si spot are visible.

sented in Fig. 4.1(c) results in a  $45^\circ$  rotation of the Si lattice with respect to the Ni lattice. Thus, the lattice mismatch between Si and the different layers can be evaluated by multiplying the literature value of the lattice parameters with  $\sqrt{2}$ . The relative position of the individual layers in respect to Si as shown in Table 5.1 can be used to map the different adjacent Bragg spots to the individual layers. With considering the widths of the individual Bragg spots, it can be inferred that the slightly blurred spots at the edge of each region of interest belong to the Ni layer. We map the central, sharp peaks to the Si membrane, since the rocking curve of the commercially acquired Si membrane in the pre-characterization in Chapter 4.3 is noticeably narrower than the rocking-curve of all other layers. Regarding the lattice mismatches with Si in Table 5.1 the weak, blurred-out spots shown in Fig. 5.1(b) and highlighted with a red circle in Fig. 5.1(a) belong to the NiO $_x$  at the surface of the specimen. According to Table 5.1 the Cu Bragg spots would emerge between the Ni and the Si peaks and would be expected to have similar appearance to the Ni spots, since they show a comparable rocking curve width as mentioned in Chapter 4.3. However, the distance between these Bragg spots is too narrow to determine whether a Cu peak is visible in-between.

Layer	lattice parameter [Å]	aligns to Si	arranged lattice parameter [Å]	lattice mismatch with Si
NiO <sub>x</sub>	4.18 [71]	45°	5.90	1.087
Ni	3.52 [61]	45°	4.98	0.917
Cu	3.62 [72]	45°	5.12	0.943
Si	5.43 [61]	-	-	1

Table 5.1: Overview of the lattice parameters of the different layers and their arrangement with respect to Si. The lattice mismatch regarding the Si peak is needed for the evaluation of the Bragg spot positions of the sputtered layers in respect to the refined Si peaks of the Si membrane. Values > 1 indicate a smaller distance to the zero order (000), which displays the direct electron beam.

## 5.2 Angle-dependent intensity and rocking curves

To estimate the crystallinity of the investigated Ni thin-film, angle dependent intensity measurements (rocking curves) are acquired for all analyzed Bragg peaks. The rocking curves are obtained by ultrafast electron diffraction measurements with non-compressed electron pulses by centering the sample within the electron beam and rotating 55° around the Ni[0 1 0]-axis in 0.250° steps and 5° around the Ni[1 0 0]-axis with a step size of 1°. The range of the rotation around the Ni[1 0 0]-axis is defined significantly smaller, because the goniometer only allows a limited rotation around this axis. To avoid losing the centering of the sample within the electron beam its position along the Ni[0 1 0] and Ni[1 0 0]-axis is corrected in every step. In order to not saturate the phosphorous screen of the CMOS camera, roughly 20 electrons per pulse are adjusted and the exposure time of the CMOS camera is set to 2 s. No iterations of the recorded data are performed, hence the resulting 2D rocking curve displayed in Fig. 5.2 presents non-averaged data. The enlargement of the angular width and the shifting intensity centers can be explained with a slightly changing displacement of the sample during the scan, resulting in a subtle decentralization of the sample. This effect is most prominent in the Ni(0 2 0) and Ni(0 $\bar{2}$  0) peak, since these are the Bragg spots located closest to the rotation axis Ni[0 1 0]. Partially, the shifting of intensity can also be observed in the Ni(2 $\bar{2}$  0), Ni(2 2 0), Ni(2 $\bar{2}$  0) and Ni(2 $\bar{2}$  0) spots, which should also be an artifact of a slightly wrong position correction. The angular width of the rocking curve is determined to be  $\omega = 6.45 \pm 0.14^\circ$  FWHM by fitting a Gaussian function to Ni(200), one of the Bragg spots not suffering from any attributes due to the correction procedure, as presented in Fig. 5.3. The increase of the fitted width compared to the X-ray data presented in Fig. 4.2(b) can be accounted to electron energy losses and other inelastic diffraction effects [49]. A strong deviation from

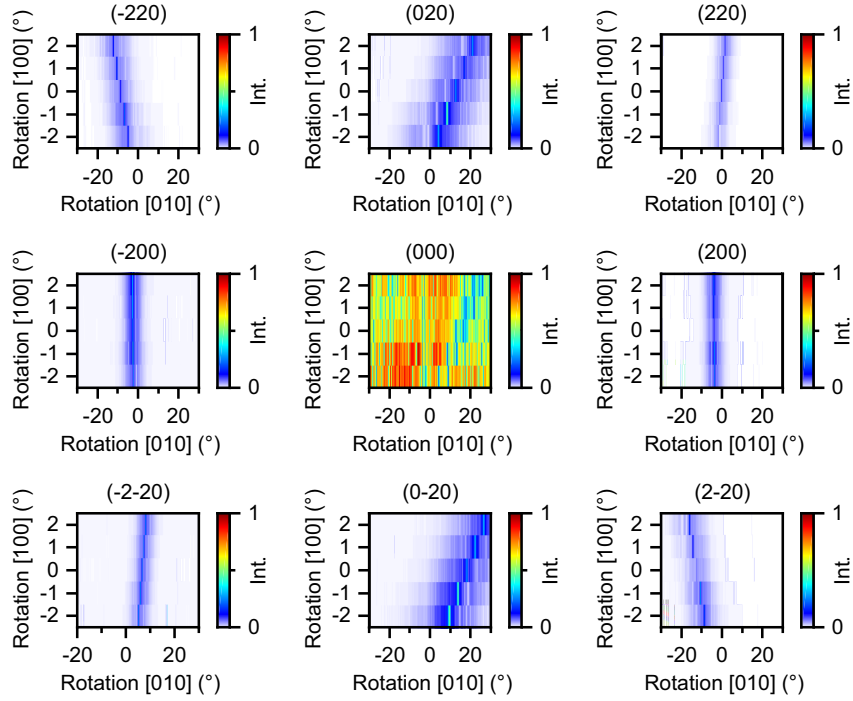


Figure 5.2: Colormap of the angle-dependent intensity development for all analyzed Ni Bragg spots.

the Gaussian profile can be observed at approximately  $-1.85^\circ$ ,  $2.15^\circ$  and  $0^\circ$ . These fluctuations within the intensity profile can be ascribed to the single-crystalline Si(100) membrane that the Ni(200) layer is sputtered on. Due to the Si membranes' high crystallinity, its rocking curve has very sharp, defined peaks with a low angular width and high intensities. For the analysis of the Ni peaks, only regions of interest were investigated. Thus, a peak of the Si membrane can be optimized at a specific angle, without being observed within the analysis. Since the total amount of electrons per pulse is constant, an increase of intensity at a not analyzed position results in an intensity decrease of the analyzed Ni peak as observed at  $-1.85^\circ$  and  $2.15^\circ$ . On the contrary, the strong increase of intensity at  $0^\circ$  indicates the appearance of the adjacent Si( $2\bar{2}0$ ) peak. Overall, such effects do not influence the time-resolved results, because for the time-resolved diffraction scans a specific angle, optimizing the Ni Bragg spots, is chosen and not rotated during the data acquisition. The probability of the evaluation of an adjacent Si peak is minimized by selecting an elliptical region of interest just containing the Ni peak as shown in Fig. 5.6(a-b).

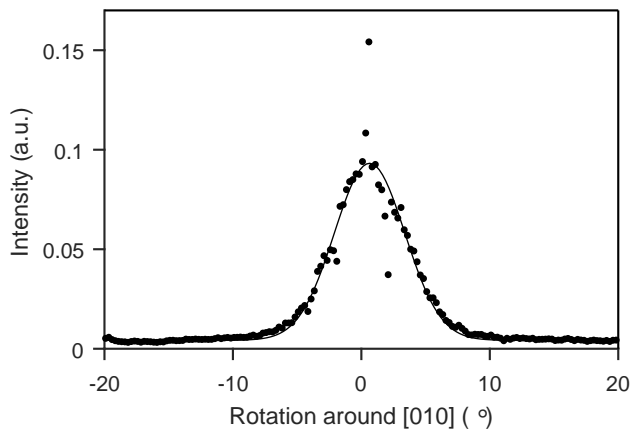


Figure 5.3: Rocking curve for the Ni(200) Bragg spot (dots) with a Gaussian fit (solid curve). The fit retrieves a width of  $\omega = 6.45^\circ$  (FWHM). For measuring the angle-dependent intensity the specimens angle is fixed along the [100]-axis to  $0^\circ$  and the rotation occurs along the [010]-axis.

### 5.3 Time-resolved observations of Ni dynamics

In the following, the time-resolved dynamics are discussed. We use a pump-probe setup with the THz-compressed electron pulses described in Chapter 3.2 as probe and the compressed optical pulses outlined in Chapter 3.1 as pump pulses to investigate time-dependent changes of the Ni Bragg spots observable within the reciprocal lattice. If not stated differently, we apply a fluence of  $3.6 \text{ mW/cm}^2$  to induce the demagnetization of the Ni specimen. Since the Ni surface of the sample suffered for higher fluences, we refrain to apply more than  $3.6 \text{ mW/cm}^2$  in order to avoid a melting of the Ni layer and to prevent the formation of new layers within the specimen. All time-dependent data is presented in relation to  $t_0 = 0$ , the time at which an optical pulse arrives at the sample position at the same time as the probe pulse.

In order to analyze the temporal evolution of the width and position of each Bragg spot, a Pseudo-Voigt function is fitted to each Ni Bragg spot individually. The Pseudo-Voigt function is defined as the sum of the Gaussian function  $G(x)$  and the Lorentzian function  $L(x)$  [73, 74] with a parameter  $0 \leq \eta \leq 1$  to shift the profile towards Gaussian for  $\eta$  approaching 1 or Lorentzian, when  $\eta$  converges to 0. It can be defined as

$$pV(x) = I \cdot (\eta \cdot G'(x, \Gamma) + (1 - \eta) \cdot L'(x, \Gamma)), \quad (5.1)$$

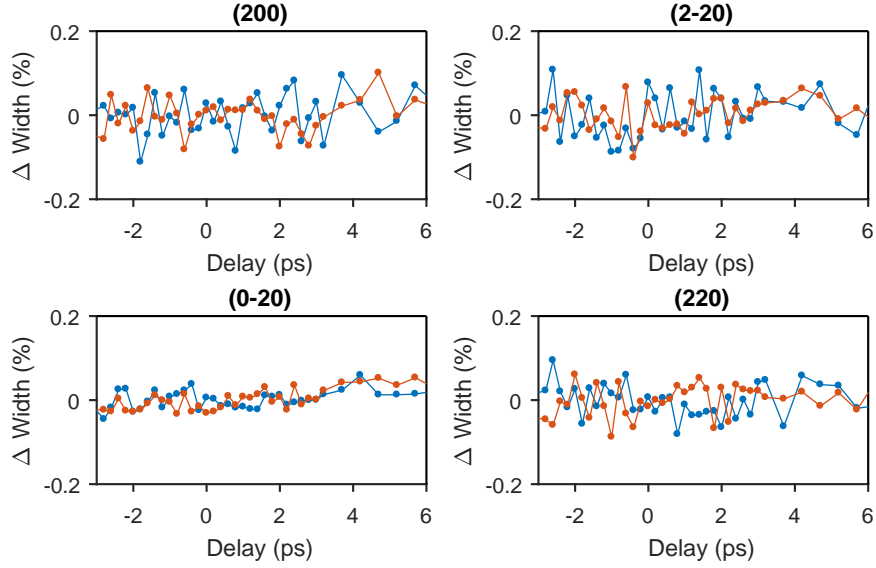


Figure 5.4: Temporal evolution of the Bragg spot width. The blue curve describes the broadening along the x-axis and the orange curve the broadening along the y-axis.

where  $G'(x, \Gamma)$  is the normalized Gaussian

$$G'(x, \Gamma) = \frac{1}{\sigma\sqrt{2\pi}} \cdot e^{-\frac{(x-x_0)^2}{2\sigma^2}}, \quad (5.2)$$

with  $\sigma = \frac{\Gamma}{2\sqrt{2\ln(2)}}$  and  $L'(x, \Gamma)$  is the normalized Lorentzian described with

$$L'(x, \Gamma) = \frac{1}{\pi} \cdot \frac{(\Gamma/2)}{(x - x_0)^2 + (\Gamma/2)^2}. \quad (5.3)$$

The parameters  $I$ ,  $\Gamma$  and  $x_0$  represent the peak intensity, the peak width (FWHM) and the peak center. The evaluation of the Ni(200) and Ni(0 $\bar{2}$ 0) spot is representative for Ni{200} and the Ni(220) and Ni(2 $\bar{2}$ 0) spot is representative for Ni{220}. The analysis of the Bragg spots' width is presented in Fig. 5.4. No change of the fitted peak width can be observed before and after  $t_0$ . Moreover, the fluctuation of the fitted width is below 0.2%. This indicates that there is no substantial transient stain due to laser illumination, since a strain would result in a less refined peak.

When we fit the peak center, we retrieve information how much the central position of a Bragg spot moves due to laser interaction. This movement of the

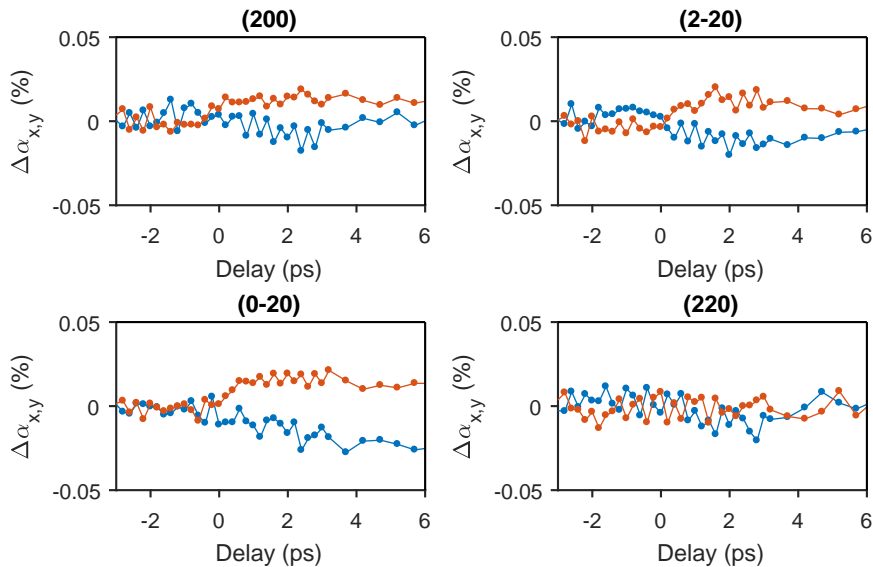


Figure 5.5: Temporal evolution of displacement of the Bragg spots. The blue curve describes the movement along the x-axis and the orange curve the movement along the y-axis. The displacement occurs due to a change of the Bragg spot angles  $\Delta\alpha$ .

central position equals a change of the Bragg angle  $\Delta\alpha$ . There is a slight development to a different Bragg spot distance in the reciprocal lattice after  $t_0$ , as depicted in Fig. 5.5. Since the decay is tiny and within hundreds of femtoseconds, we attribute this as an artifact of the reference procedure applied. Furthermore, the observed change of the Bragg angle is below 0.05%. Hence, the analyzed crystal is not subjected to isotropic or anisotropic deformations and keeps his volume during experiments. The percentage change of width and position differ by an order of magnitude. This difference can be explained with the different regions of interest chosen for the fitting procedure. For fitting the width a rectangular region of interest is selected, as presented in Fig. 5.1(b-c). Although a rectangular region of interest has the possibility to contain a Si peak, we want to fit the complete width, to be able to observe any change of peak width. For the fit of the position, an elliptical region of interest is chosen, as shown in Fig. 5.6(a-b). We can crop here the edges of the peak, since only the maximum is relevant. Thus, the peak center of the Pseudo-Voigt profile is fitted with more precision to the Bragg spot. From the unchanged position and width of the Ni peaks after laser excitation, we conclude that there is no substantial transient strain or lattice expansion during the investigated time range. The intensity of the time-resolved Bragg spot evolution of the Ni peaks is investigated with manually selected regions of interest. An elliptical area is chosen, as depicted in Fig 5.6(a-b), to optimize the Ni spots. In

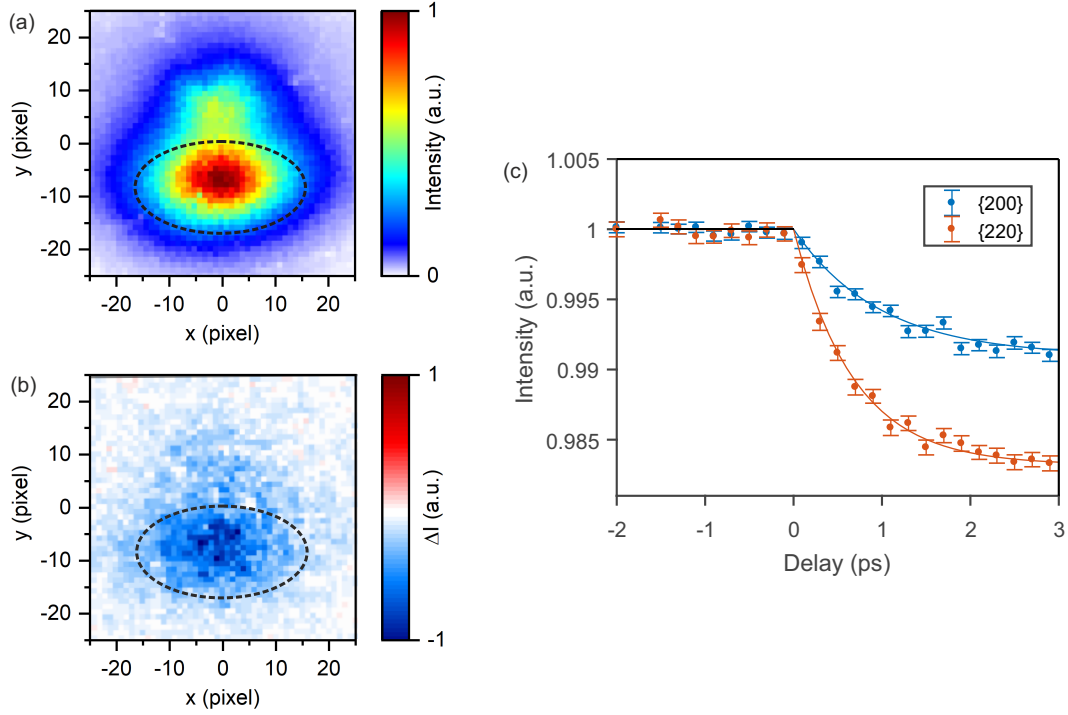


Figure 5.6: Temporal intensity development and close up image of Ni( $0\bar{2}0$ ) from Fig. 5.1. The dashed lines in (a,b) represent the region of interest selected for evaluation of  $I_{0\bar{2}0}$ . (a) The selected Bragg spot Ni( $0\bar{2}0$ ) before laser excitation with scaled intensity. (b) The difference image of peak Ni( $0\bar{2}0$ ) calculated as  $I_{0\bar{2}0}(t \leq -1 \text{ ps}) - I_{0\bar{2}0}(2 \text{ ps} \leq t \leq 4 \text{ ps})$ . (c) Time-resolved intensity development of Ni{200} and Ni{220} with error bars. The solid lines denote a decay time of  $\tau_D = 750 \pm 40 \text{ fs}$  for  $I_{\{220\}}$  and  $\tau_D = 670 \pm 90$  for  $I_{\{200\}}$  according to Eq. (5.7). The measurement levels after saturation are  $0.9922 \pm 4 \cdot 10^{-4}$  for Ni{200} and  $0.9847 \pm 5 \cdot 10^{-4}$  for Ni{220}.

order to determine the individual Bragg spot intensity, the digital counts of each pixel of the CMOS sensor mentioned in Chapter 2.2 are summed up within the region of interest. The measured temporal intensity evolution of a peak  $I_{hkl}^{raw}(t)$  is normalized with the values before femtosecond laser interaction  $I_{hkl}^{raw}(t < 0)$ . Consequently, a function of

$$I_{hkl}(t) = \frac{I_{hkl}^{raw}(t)}{I_{hkl}^{raw}(t < 0)} \quad (5.4)$$

is applied for all the intensities presented in this Chapter. In order to minimize

the influences of fluctuations and long-time drifts of the generated electrons,  $I_{hkl}(t)$  is referenced to the integrated digital counts of the direct electron beam  $I_{(000)}(t)$  with  $I_{hkl}^{ref}(t) = I_{hkl}(t)/I_{(000)}(t)$ .

An intensity decrease after  $t_0$  can be observed within the difference image  $I_{hkl}^{diff}$  received by averaging the intensities before  $t_0$  and subtracting them with the averaged data after intensity decay with

$$I_{hkl}^{diff} = I_{hkl}^{raw}(t < t_0) - I_{hkl}^{raw}(2 \text{ ps} \leq t \leq 4 \text{ ps}). \quad (5.5)$$

In Fig. 5.6(b) the difference of  $I_{0\bar{2}0}^{diff}$  is depicted. Here, the region of interest, labeled with dashed lines, clearly displays a decrease of intensity, which is more thoroughly investigated in the next paragraph. On contrary to this, the intensity decrease of the Si peak outside of this region of interest is weak. The slight change in intensity can be explained with multiple scattering within the high quality Si membrane [75, 76]. Consequently no time-resolved intensity development within the Si Bragg spots is detected. A more detailed analysis of the Si Bragg spots is presented in Chapter 5.4.

For a more refined analysis of the intensity decrease after laser interaction with a better signal-to-noise ratio all the symmetry-equivalent Bragg spots are averaged with

$$\begin{aligned} I_{\{200\}} &= \frac{1}{4}(I_{(200)} + I_{(020)} + I_{(\bar{2}00)} + I_{(0\bar{2}0)}) \\ I_{\{220\}} &= \frac{1}{4}(I_{(220)} + I_{(\bar{2}20)} + I_{(2\bar{2}0)} + I_{(\bar{2}\bar{2}0)}) \end{aligned} \quad (5.6)$$

as a function of time. Thus, we receive a time-dependent intensity plot as presented in Fig. 5.6(c). The intensity of Ni{200} and Ni{220} decreases after laser excitation. This can be attributed to the Debye-Waller effect [77–79] explained in Chapter 2.3. Due to absorption of energy, the atoms within the lattice increase the movement around their equilibrium position. We observe an intensity decrease of  $\sim 0.7\%$  for Ni{200} with a standard error of  $4 \cdot 10^{-4}$  and for Ni{220} the intensity decreases by  $\sim 1.5\%$  with a standard error of  $5 \cdot 10^{-4}$  due to thermal disorder. In order to retrieve the time constant of the Debye-Waller effect depicted in Fig. 5.6(c) the intensity decay of Ni{200} and Ni{220} is fitted using a single exponential fit function  $I(t)$ , defined as

$$I(t) = \begin{cases} 1 & \text{for } t \leq t_0 \\ A - B(1 - \exp(-\frac{t}{\tau_D})) & \text{for } t > t_0 \end{cases}, \quad (5.7)$$

in close proximity to [80]. In Eq. (5.7),  $A$  is the signal before  $t_0$ ,  $B$  is the amplitude of the decay and  $\tau_D$  is the time constant for the exponential decay. We receive a decay time of  $\tau_D = 750 \pm 40$  fs for  $I_{\{220\}}$  and a decay time of  $\tau_D = 670 \pm 90$  fs for  $I_{\{200\}}$ .

## 5.4 Time-resolved observations of Si dynamics

The Si membrane should not absorb light in the near infrared. Therefore no forces should drive the Si atom out of equilibrium on femtosecond time scales. In order to exclude that the Si substrate influences the analyzed Ni Bragg spots, the Si peaks are investigated with the procedure introduced in Chapter 5.3 using Eq. (5.4) to calculate the time dependent intensity changes. Hereby, we minimize signal contributions from the adjacent Ni peaks by using regions of interest as shown in Fig. 5.7(a,c). The difference in intensity change after interaction with the laser is clearly visible within Fig. 5.7(b,d). Whereas the loss of intensity within the Ni peaks is in both cases about 1.5%, the change of intensity within the Si peaks is less than 0.3% and can be explained with multiple scattering. Therefore the Si atoms remain unaffected from the laser excitation and the procedure from Chapter 5.3 reveals purely the atomic motion of the Ni atoms.

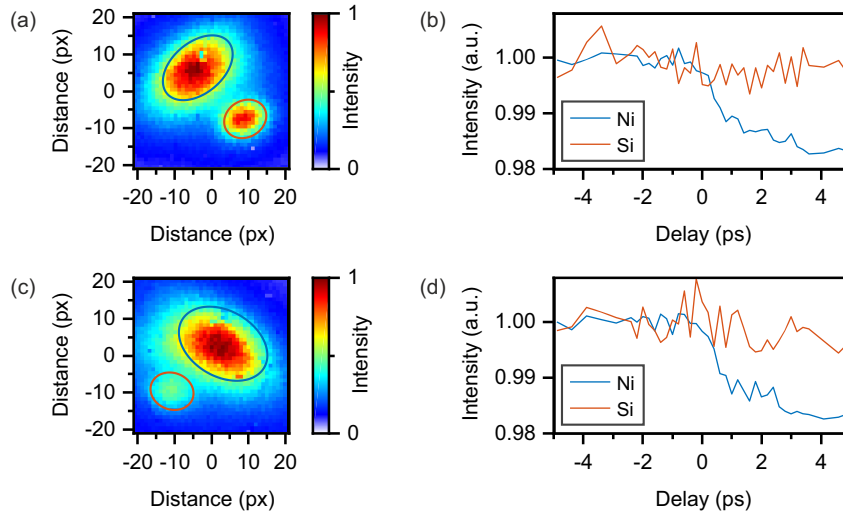


Figure 5.7: Comparison of time-dependent Ni dynamics and Si dynamics. (a,c) show the regions of interest for the Ni(220) and Ni( $\bar{2}$ 20) spot with adjacent Si peaks. The blue and orange ellipsis illustrate the areas used for evaluation of the Ni and Si spots. (b,d) display the time-resolved intensity dynamics for (a,c).

## 5.5 Fluence dependency

The laser fluence is the radiant energy received by a surface per unit area and is calculated with Eq. (2.6). For assessment of the beam waist knife edge measurements are performed at sample position and the beam profile is recorded with

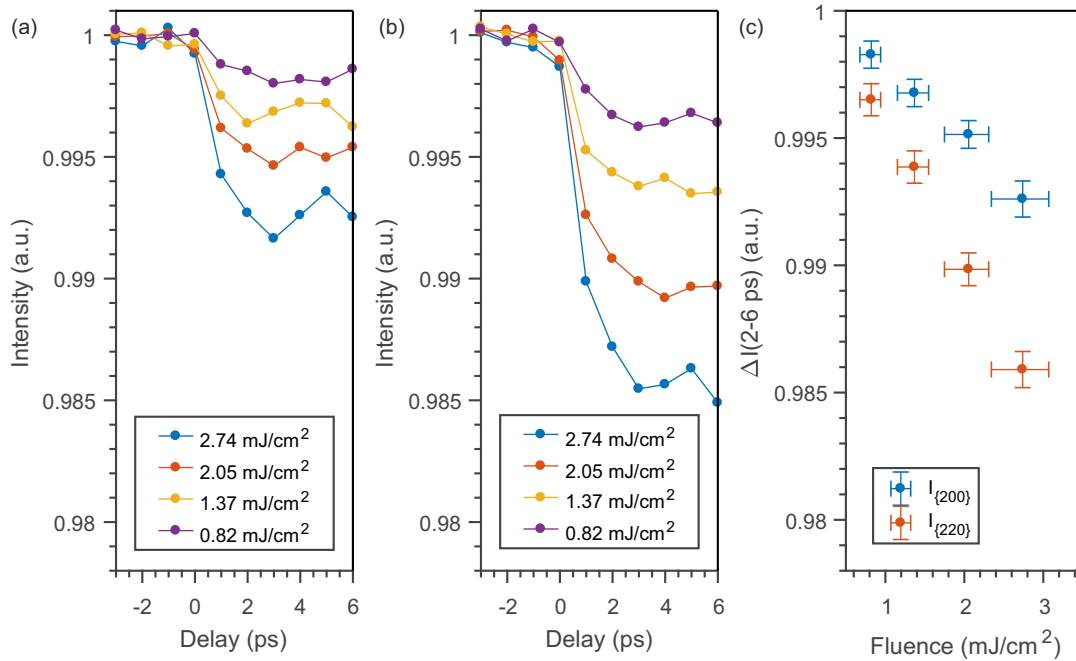


Figure 5.8: The fluence dependency of the pump-probe experiment on different Ni Bragg peaks. Temporal intensity evolution of the averaged (a) crystallographic equal Bragg peaks Ni{200} and (b) Ni{220} in respect to excitation with different laser fluences. (c) Difference in Bragg peak intensity after femtosecond laser excitation. The plot shows the mean value of the averaged Bragg peaks depicted in (a) and (b) 2 – 6 ps after laser excitation.

a *The Imaging Source* DMK 27AUJ003 camera. The resulting images are evaluated by fitting the standard error function to the integrated images. An error of 6% is assumed for estimation of the beam width due to a slightly non-Gaussian profile and therefore a less precise fit. Moreover, we assume a measurement inaccuracy of the average laser power of 0.2 mW. Further sources for an error within the assessment of the fluence could be an imprecise spacial overlap of the optical beam and the electron beam. The dependence between the laser fluence and the time-resolved intensity development  $I_{hkl}^{ref}$  of the Ni{200} and Ni{220} peaks are depicted in Fig. 5.8(a-b). Both figures show that the loss of intensity within the Bragg peaks increases with more energy deposited within the same area. This effect can again be explained with the Debye-Waller effect. Due to a higher fluence, more energy is absorbed within the illuminated area. Consequently, according to Eq. (2.15) the excitation of the lattice  $u(t)$  increases due to a higher temperature within the lattice as described by Eq. (2.17). This results in a decreased Bragg

spot intensity. The emerging Bragg peak intensity in terms of different fluences is depicted in Fig. 5.8(c). The error bar associated with the intensity change within the spots is calculated by the standard error derived from the measurements points taken from 2 – 6 ps after femtosecond excitation. The graph clearly indicates the correlation between a more intense laser radiation and a more pronounced loss of Bragg peak intensity after excitation and consequently stronger thermalization of the lattice. We observe a linear fluence dependence for the Ni{200} and Ni{220} peaks. For the acquisition of the fluence dependent data, the magnetic construct is removed. Thus, we cannot precisely determine the initial in-plane magnetization.

## 5.6 Base temperature

The experiments aim to investigate the structural change in dependence of demagnetization. Hence, it is important that the base temperature of the Ni thin-film is below the Curie temperature  $T_{Curie} = 627$  K, since otherwise no difference before and after demagnetization can be evaluated. Agranat et al. [81] performed experiments with picosecond pulses on Ni and reported about no irreversible demagnetization effect up to the melting point of the sample. Hence, this is an indication that the induced magnetization in our experiment is transient. Since we are using femtosecond pulses for investigation, we double-check the base temperature in the following with the Debye-Waller-Factor and Magneto-optical-Faraday measurements.

For a first evaluation, we compare  $I_{\{200\}}(t < t_0)$  with  $I_{\{200\}}^{no\ laser}$  and infer a difference of 0.5%. With reported values for the mean square displacement  $\langle u^2 \rangle$  as a function of temperature [82], we use Eq. (2.15) to determine with the values of the mean square displacement the values of the Debye-Waller-Factor  $\frac{I}{I_0} = \exp(\frac{-1}{3}|G|^2 \cdot \langle u^2 \rangle)$ . Subsequently, we linear fit the calculated values for the Debye-Waller-Factor as presented in Fig. 5.9. With the fitted curve, a base temperature of  $\frac{|I_{\{200\}}(t < t_0) - I_{\{200\}}^{no\ laser}|}{2.11 \cdot \exp(-4)} \text{ K} + T_{lab} = 319 \text{ K}$  can be inferred, with  $T_{lab} = 295 \text{ K}$ . Hence, we can assume that the specimen does not get heated continuously beyond  $T_{Curie}$  by the near infrared pulses. As explained in Chapter 2.3, the Debye-Waller-Factor calculates from  $\langle u^2 \rangle$ , which means, that it is sensitive to changes of temperature. However, due to the dependence to the reciprocal lattice  $G^2$  it is also affected by changes of the interplanar spacing, the bond length and by lattice imperfections [78]. Hence, calculations from the Debye-Waller-Factor to the temperature are critical.

To verify an only transient demagnetization of the Ni thin-film, time-resolved Magneto-optical Faraday effect measurements are performed by Daniel Kazenwadel at Universität Konstanz to estimate the demagnetization  $M$  as a function

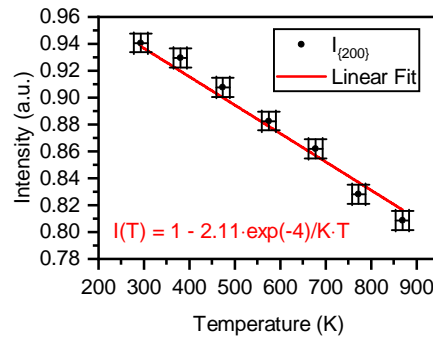


Figure 5.9: Estimation of the base temperature of the Ni specimen with calculation of the Debye-Waller-Factor through mean square displacement. Since we need to manually read out the data from [82], we assume an error of  $\pm 15$  K for the temperature and  $\pm 0.007$  for the intensity.

of laser excitation. In these measurements the hysteresis loop of the ferromagnetic thin-film is obtained for a fixed delay by sweeping the magnetic field  $H$ . For each value of  $H$  the magnetization  $M$  is averaged over several hundred pulses. By recording the hysteresis curve for different time delays, we obtain a time-dependent function of saturation magnetization. In order to create a comparable measurement, we adjust similar conditions as in the ultrafast electron diffraction experiments. For this, we choose the same incidence angle, central wavelength, repetition rate and a pulse duration of 600 fs. Since these measurements are under ambient conditions, we apply a fluence close to the damage threshold of the Ni thin-film, as it is done in the diffraction experiments. The hysteresis curve depicted in Fig. 5.10(a) compares the change of the magnetization  $M$  before (black curve) and after (red curve) laser excitation, with a diminished amplitude but otherwise unchanged hysteresis curve. The corresponding time-dependent dynamics of saturation magnetization is revealed by the difference of the mean value of the saturation magnetization at the edges of the hysteresis curve. It is depicted in Fig. 5.10(b) and shows a rapid decrease of saturation magnetization at  $t_0$ . The reduction of saturation magnetization is  $\approx 50\%$ . Since the experiment is repeated with the same repetition rate of  $f_{rep} = 25$  kHz as in the diffraction experiment and the signal is averaged over several pump-probe cycles, we can conclude from this Magneto-optical Faraday effect measurement that the demagnetization in the diffraction experiments is transient. Thus, the base temperature must be below  $T_{Curie}$ . If the sample would be constantly beyond  $T_{Curie}$ , the intensity decrease in Fig. 5.10(b) could not be measured, since the ferromagnetic metal would constantly behave like a paramagnet. Moreover, if the thin-film's base temperature

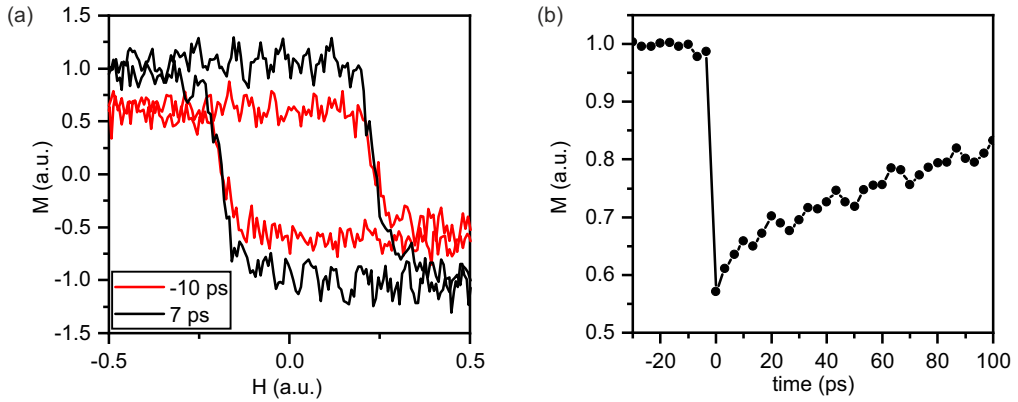


Figure 5.10: Normalized measurements of the Magneto-optical Faraday effect of a similar Ni thin-film (a) Measured hysteresis curves before (black curve) and after (red curve) laser interaction (b) Observation of the time-dependent Magneto-optical Faraday Effect. Measurements and evaluation executed by Daniel Kazenwadel at Universität Konstanz.

would be above  $T_{Curie}$ , the hysteresis curve shown in Fig. 5.10(a) would collapse. Since for the diffraction measurements and for the Magneto-optical Faraday effect measurement a laser fluence in close approximation to the threshold of the thin-film's damage is applied, we can infer that the base temperature in the diffraction experiments is below  $T_{Curie}$ . Thus, we observe ferromagnetic-dependent changes in Chapter 5.7.

## 5.7 Asymmetry and evidence for chiral phonons

For the evaluation of the Bragg spots presented in Chapter 5.3 we average all crystallographic equivalent peaks to Ni{200} and Ni{220}, to optimize the signal-to-noise ratio. However, despite their crystallographic equivalence, these spots are not equal in dependence of the initial in-plane magnetization. For the investigation of the Ni peaks with respect to their initial magnetization, we use a different approach: The peaks Ni(200) and Ni( $\bar{2}$ 00), in the following denoted with Ni{200}, as well as the peaks Ni(020) and Ni(0 $\bar{2}$ 0), denoted as Ni{020}, are Friedel pairs. According to Friedel's law the diffraction intensities of  $(hkl)$  and  $(\bar{h}\bar{k}\bar{l})$  are equal, hence  $I_{hkl} = I_{\bar{h}\bar{k}\bar{l}}$ . This statement is empirical, but has been widely adopted [83–85]. In order to exclude the possibility of a violation of Friedel's law due to out-of-phase intensity oscillations [84], we investigate the aver-

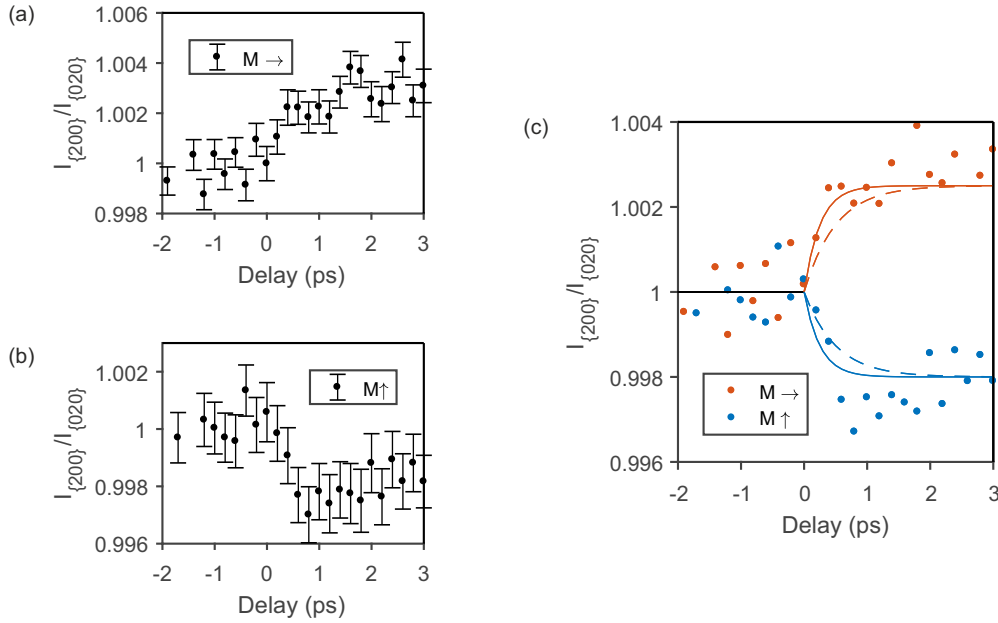


Figure 5.11: Time-resolved development of the anisotropy  $I_{\{020\}}/I_{\{200\}}$ . (a,b) present the temporal development of the anisotropy in regard of an initial magnetization along the Ni[1 0 0] and Ni[0 1 0] orientation with error bars. In (c) both initial magnetic orientations are plotted together. The orange data points refer to  $M \rightarrow$  with a level saturation of  $1.0028 \pm 0.0007$  and the blue curve refers to the  $M \uparrow$  measurement with an intensity saturation at  $0.9981 \pm 0.001$ . The solid and dashed curves suggest a possible fit of the intensity development according to Eq. (5.7) with  $\tau_D = 500$  fs (solid lines) and  $\tau_D = 250$  fs (dashed lines).

age values of the Friedel pairs  $I_{\{200\}} = \frac{1}{2}(I_{200} + I_{\bar{2}00})$  and  $I_{\{020\}} = \frac{1}{2}(I_{020} + I_{0\bar{2}0})$ . By applying this procedure the experimental data becomes insensitive to possible modulations of the crystallographic axes. Since we calculate the average of the Friedel pairs, we would not expect to observe time dependent intensity changes for the relation  $I_{\{200\}}/I_{\{020\}}$  in the highly symmetric pattern of Ni. Only the magnetic field affects the peaks of Ni $\{200\}$  differently than the peaks of Ni $\{020\}$ . When the magnetic field is aligned parallel to Ni $\{200\}$  it is aligned orthogonal to Ni $\{020\}$  and vice versa. However, Fig. 5.11(a-c) shows a small modulation of  $I_{\{200\}}/I_{\{020\}}$  after laser interaction. For the magnetization along Ni[0 1 0], we obtain a ratio of  $I_{\{200\}}/I_{\{020\}} = 0.998$  and thus an anisotropy. On the contrary, we obtain a ratio of  $I_{\{200\}}/I_{\{020\}} = 1.002$ , when we turn the magnetic construct by  $90^\circ$  and create thus an initial magnetization along Ni[1 0 0]. The levels of the curves saturize within  $1 \text{ ps} < t < 4 \text{ ps}$  and can be evaluated as  $0.9981 \pm 0.001$

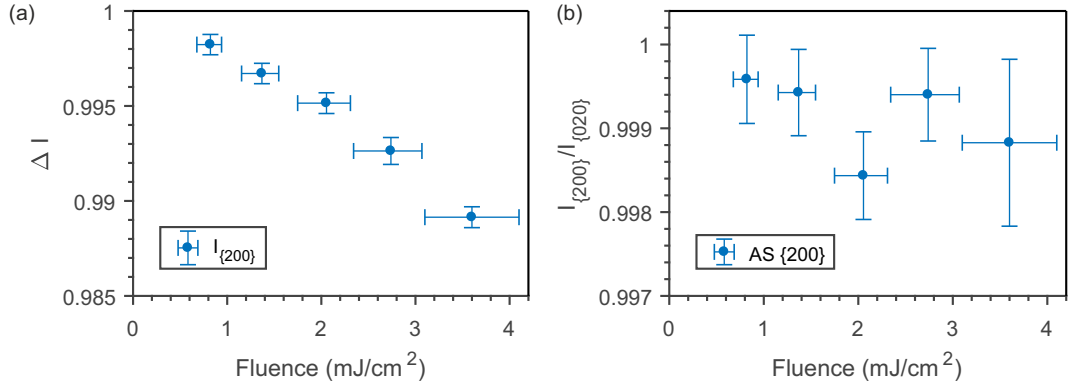


Figure 5.12: Fluence dependence of the (a) Debye-Waller effect calculated as in Chapter 5.3 and the (b) anisotropy for Ni{200}. In both plots. We retrieve  $\Delta I$  by integration of  $t > 2$  ps.

and  $1.0028 \pm 0.0007$ . A fit of the anisotropies shown in Fig. 5.11 with Eq. (5.7) results in a decay time  $\tau_D = 490 \pm 230$  fs for Fig. 5.11(a) and  $\tau_D = 235 \pm 180$  fs for Fig. 5.11(b). As Fig. 5.11(c) indicates, the measured intensity ratio is equally suitable for time constants of  $\tau_D = 250$  ps and  $\tau_D = 500$  ps. Previous studies have reported that a time span of at least 120 – 300 fs is needed for the demagnetization of Ni [4, 8, 15, 42, 86]. This is in agreement with the data presented in Fig. 5.11(a-c). If the lattice disorder would be solely based on a transient temperature increase, the asymmetry observed in Fig. 5.11 would not be possible, since it would affect Ni{020} and Ni{200} similarly due to equipartition. Thus, the observation of this anisotropy reveals nonthermal phonon dynamics and implicates a localization of the excitation and a fracture of the symmetric crystal structure.

When we apply  $I_{\{200\}}/I_{\{020\}}$  to the fluence dependent data presented in Fig. 5.8 and combine it with the data acquired for Fig. 5.11(b), we get an indication that the intensity of the anisotropy scales linearly with the fluence (see Fig. 5.12(b)). Note, that although for the fluence dependent measurement the magnetic construct is removed, the Ni thin-film has to have in-plane magnetization due to the shape anisotropy, mentioned in Chapter 3.3. Although we can not unambiguously determine the direction of the in-plane magnetization, we can assume that it is close to Ni[010]. In Chapter 7.2 we will show, how such a magnetic-field dependent asymmetry within these crystallographic equal peaks could be explained and why this anisotropy reveals the transfer of angular momentum from the electronic spin to the crystal lattice.

We refrain from time-resolved measurements with different polarizations, since measurements by Dalla Longa et al. [87] show that demagnetization time and

electron-phonon equilibration time are not affected by pump helicity.



# Theoretical considerations and molecular dynamics simulation

The theoretical results are simulated by Hannah Lange and Dr. Martin Evers from the group of Prof. Dr. Ulrich Nowak at the Universität Konstanz. As their results are crucial for the design of the magnetic field and for the estimated intensity of the expected effect, the following section describes the frame demanded for the simulation by our own design, a rough summary of its realization and the theoretical observation of anisotropy. The simulations presented in this chapter are obtained using molecular dynamics and are computed with LAMMPS (Large-scale Atomic/Molecular Massively Parallel Simulator) and are executed by Prof. Dr. Ulrich Nowak and coworkers.

## 6.1 Definition of the problem

Simulations for explaining the ultrafast demagnetization are often based on the three-temperature model [4, 88, 89]. This model extends the two-temperature model of Anisimov et al. [90] and Kaganov et al. [91], which investigates the electron emission from metal surfaces, and assumes three thermalized reservoirs for electrons, spins and the lattice. This approach has been questioned before [92, 93], since it ignores non-equilibrium behaviour. Moreover, it neglects the conservation of angular momentum [8] we consider as the crucial effect. Thus, a different model is needed for simulating the consequences on the lattice dynamics of the ultrafast demagnetization of Ni. In order to simulate an excitation of the lattice with angular momentum  $\Delta L = \hbar e_M = m\Delta \times v$  ( $e_M \parallel$  magnetization) an atom of mass  $m$  is deflected by  $\Delta$  along  $e_1$  from its equilibrium position with a velocity  $v = \frac{\Delta L}{m\Delta}$  along  $e_2(\perp e_1)$  as depicted in Fig. 6.1(a-c) [94]. The angular momentum emerges

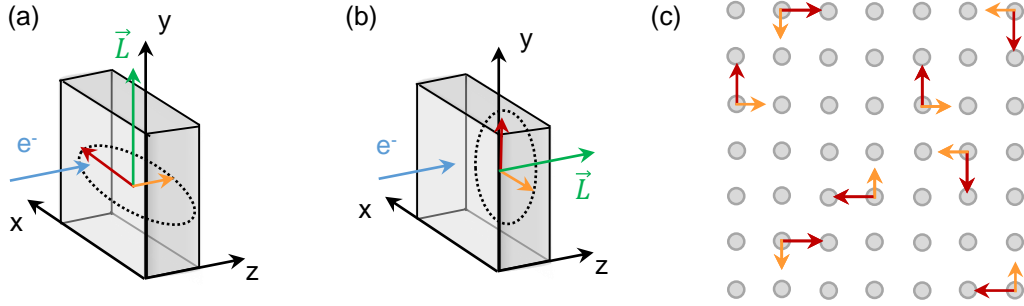


Figure 6.1: Idea for the simulations. Red arrows imply the deflection  $\Delta$  and orange arrows the velocity  $v$  perpendicular to the deflection. Green arrows depict the resulting angular momentum change and blue arrows label the incoming electrons. (a) Visualization of the in-plane magnetization resulting in a phonon excitation in the x-z-plane, (b) Visualization of the out-of-plane magnetization resulting in the excitation of the phonons in the x-y-plane. (c) Visualization of the principal idea of an algorithm introducing an angular momentum to the crystal by distributing  $\Delta$  and  $v$  randomly on single atoms. Figure 6.1 is inspired and redrawn from the Bachelor Thesis of Hannah Lange [94].

along  $e_3$ , perpendicular to the plane of the phonon excitation  $e_1 \times e_2$ . An out-of-plane magnetization ( $e_M \propto e_z$ ) can be modelled by selecting the phonon excitation  $m\Delta \times v$  in the x-y-plane as shown in Fig. 6.1(b). Thus, an angular momentum change  $\Delta L$  is measurable along the z-direction. For an in-plane magnetization ( $e_M \propto e_y$ ) the phonon excitation is along the x-z plane, as depicted in Fig. 6.1(a). Hence,  $\Delta L$  can be observed along the y-direction.

For a first approach, a demagnetization of  $D = 50\%$  as reported by Beaurepaire [4] is suggested. The magnetic moment per atom can be estimated with the saturation magnetization  $M_{Ni} = 5.219(27) \cdot 10^5 \text{ A m}^2$  [95] as

$$\mu_{Ni} = M_{Ni} \cdot V_{atom} = 5.69 \cdot 10^{-24} \text{ A m}^2 = 0.616 \mu_B, \quad (6.1)$$

where  $\mu_B = \frac{e \cdot \hbar}{2 m_e}$  describes the Bohr magneton and  $V_{atom} = \frac{(3.52 \text{ \AA})^3}{4}$  the volume per Ni atom. A demagnetization of  $D = 50\%$  is correlated with a change of magnetic moment and thus with a change of the angular momentum per atom with

$$L_0 = \mu_{Ni} \frac{2 m_e}{g_e \cdot e} = 3.25 \cdot 10^{-35} \text{ J s} = 0.308 \hbar, \quad (6.2)$$

where  $g_e = 1.8550 \approx 2$  describes the Landé-Factor [94, 96]. This equals a transfer of spin angular momentum  $\hbar$  to every seventh atom. In dependence of  $\mu_B$  Eq. (6.2)

converts to

$$\Delta L = D \frac{\mu_{Ni} \hbar}{g_e \mu_B} \approx 0.154 \hbar. \quad (6.3)$$

## 6.2 Numerical simulation

The implemented algorithm is designed by Prof. Dr. Ulrich Nowak and coworkers according to our requirements introduced in Chapter 6.1. It computes the consequences of the lattice dynamics, for the case of an angular momentum transfer of the demagnetized atoms to the lattice. Hereby, the algorithm is designed to not introduce a total momentum to the simulated crystal. A demagnetization of 50% is assumed according to measurements of Beaurepaire et al. [4], corresponding to an angular momentum transfer of  $\hbar$  to every seventh atom as calculated with Eq. (6.3) equally distributed over the simulated cubic Ni crystal in free space. The theoretical physicists designed the algorithm to disperse the angular momentum with respect to the center of mass of the crystal. The transfer of the angular momentum is modelled as a local excitation of the lattice (in contrast to a macroscopic rotation). Consequently, the algorithm chooses the excited atoms and the direction of velocities and deflection uniformly, but half of the chosen atoms carry the exact negative velocities with respect to the center of mass, to maintain a linear momentum of zero. The procedure is depicted in Fig. 6.2. Since the simulation of the demagnetization is performed by collaborators, this thesis only describes the general setup and the results important to us. Further information about the simulation can be found in the Bachelor thesis of Hannah Lange [94].

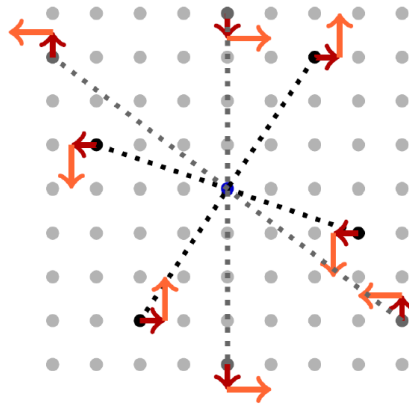


Figure 6.2: Visualization of the algorithm as implemented by Hannah Lange and Dr. Martin Evers. By distributing the angular momentum with regard to the center of mass (blue center) the transfer of angular momentum corresponds to a local excitation. Graphic taken from Bachelor thesis of Hannah Lange [94].

### 6.3 Results

Depending on the incident radiation the plane for this implemented phonon excitation can be either selected perpendicular or parallel to the electron beam. A perpendicular alignment will result from an out-of-plane magnetization as depicted in Fig. 6.1(b), where the angular momentum change is perpendicular to the crystal's surface. A parallel alignment to the radiation's direction will model an in-plane magnetization as presented in Fig. 6.1(a) with a phonon excitation parallel to the incident radiation. Calculations are performed by Hannah Lange for both cases, revealing an observable anisotropy with diffraction intensities only for the in-plane configuration. As depicted in Fig. 6.3(a), the temporal intensity development for Bragg spots parallel to the applied magnetic field differs from the temporal intensity development of the Bragg spots perpendicular to the magnetic field for an in-plane magnetization of the Ni specimen. Due to the applied magnetic field the deflection happens only in the Ni[1 0 0] and Ni[0 0 1]-direction, but not in the Ni[0 1 0]-direction. Thus an anisotropy between the peaks in the Ni[1 0 0] and Ni[0 1 0]-plane arises. In the out-of-plane configuration no difference in

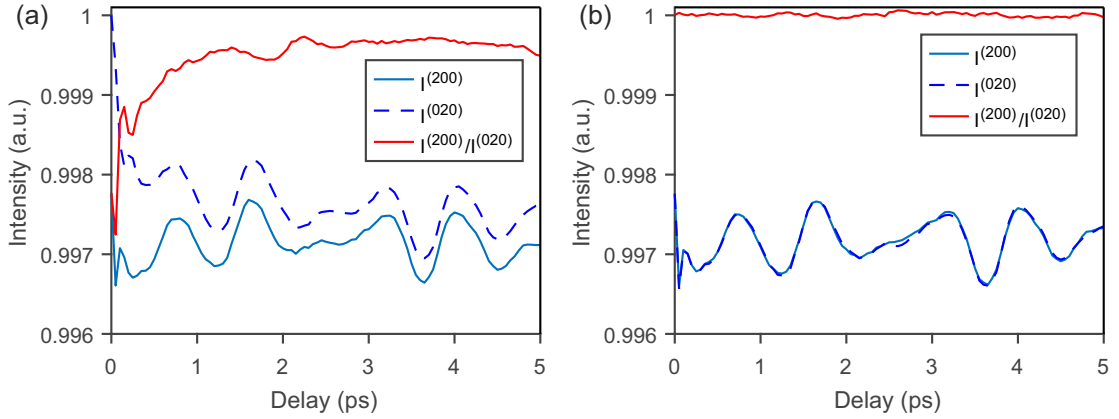


Figure 6.3: Simulation of the (a) in-plane and (b) out-of-plane configuration of the phonon excitation with electron probe in Ni[0 0 1]-direction. For the out-of-plane configuration no anisotropy is revealed. The in-plane configuration depicts anisotropy. Both simulations are calculated with  $10^3$  unit cells (4631 atoms) and free boundaries at 0 K. Graphs recalculated from data from Bachelor thesis of Hannah Lange [94]. Simulation performed by Hannah Lange at Universität Konstanz.

the temporal intensity development is observable, since in this configuration both Ni[1 0 0] and Ni[0 1 0]-direction are exposed equally to the magnetization change of

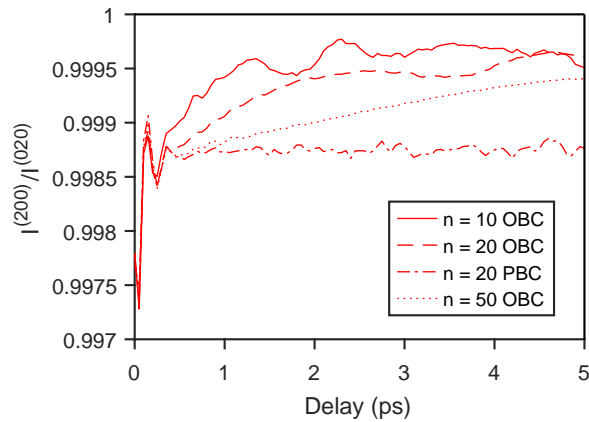


Figure 6.4: Evolution of asymmetry with different crystal sizes ( $n^3$  = amount of unit cells) and different boundary conditions. For periodic boundary condition, no constant increase of the anisotropy is observed. Simulation performed by Dr. Martin Evers at Universität Konstanz.

the demagnetization. Thus, no anisotropy in the calculated traces is observable as depicted in Fig. 6.3(b). The simulated anisotropy in Fig. 6.3(a) depicts a continuous rise of intensity within the first 4 ps. However, as Fig. 5.11(a-c) shows, we are not able to confirm this rise experimentally. Thus, additional simulations with different crystal sizes and different boundary conditions are performed<sup>1</sup>. For open boundary conditions (OBC) the angular momentum is strictly conserved. Here, the simulated increase of intensity development rises slower for more simulated unit cells, which can be identified as finite-size effect related to the existence of boundaries not present in the experiment. Investigations with periodic boundary conditions (PBC) reveal a simulated anisotropy without a gradual intensity increase as depicted in Fig. 6.4. Consequently, the simulation of the theoretical model confirms an anisotropy in the order of  $10^{-3}$  for an in-plane magnetization of the Ni thin-film.

<sup>1</sup>Simulations performed by Dr. Martin Evers at Universität Konstanz.



## Discussion, conclusions & outlook

In this chapter the main mechanisms used to describe ultrafast demagnetization are presented. Until today, the process of ultrafast demagnetization is highly debated. The origin of this mechanism and the preservation of the angular momentum is still elusive. We argue, how our idea of the emission of a chiral phonon prior to macroscopic specimen rotation is related to earlier approaches to explain this phenomenon and describe how our observations of the results from Chapter 5 fits to this idea. Furthermore, we explain how the observation of an asymmetry in the intensity relation of  $I_{\{200\}}/I_{\{020\}}$  reveals an angular momentum transfer to the lattice. Finally, we mention possible steps to improve the experiments further.

### 7.1 Previous theories of demagnetization

Since the first observation of ultrafast demagnetization by Beaurepaire et al. [4] in 1996 many researchers tried to explain this phenomenon. There have been investigations in order to explain the role and relations between laser photons, electronic states, spin excitations and lattice dynamics [97–101]. Stanciu et al. [100] reported a controllable reversal of the magnetic configuration within GdFeCo with circularly polarized femtosecond pulses and Radu et al. [99] presented experiments using linearly polarized femtosecond laser pulses, showing that the magnetization in GdFeCo can be manipulated thermally. These experiments expose that an external field is not required to switch the magnetization on ultrafast timescales, but optical pulses. The absorbed energy of these pulses is transferred to the electron bath, creating an out-of-equilibrium electron distribution [4, 15]. Afterwards, the energy of the hot electron bath transfers to the spin, inducing spin excitations within 20 fs, which store the magnetic energy. Demagnetization occurs after  $\sim 176$  fs, driven by relaxation of the nonequilibrium spins [15]. Although we

know the timescale for demagnetization, it is still uncertain, where the angular momentum gets transferred to in such a short time period. There are two main mechanisms in discussion for ultrafast demagnetization: the spin-flip scattering and the spin-transport mechanism.

The spin-transport mechanism presumes that the quenching of magnetization occurs by the transport of majority spins away from the illuminated area. Since the transport of minority spins is less efficient, this leads to a depletion of majority spins. The result is an area with a diminished magnetization density [17]. Experiments performed by Eschenlohr et al. [21] and Siegrist et al. [102] report an indirectly reduced magnetization of a ferromagnetic material, by optical excitation of a metallic layer in close proximity. Turgut et al. [103] and Melnikov et al. [104] observed spin transport after the laser illumination of a ferromagnet into unexcited layers of neighboring ferromagnetic or nonmagnetic metals. Thus, there are indications that spin-transport can contribute to ultrafast demagnetization. Nevertheless, there has been evidence for an unaltered demagnetization process by Schellekens et al. [105], where an insulating sapphire substrate prevents the transport of majority spins away from the pumped layer. If the main driving force for the demagnetization process would be the spin-transport, the angular momentum should stay within the ferromagnetic layer in this scenario. Consequently, the experiment by Schellekens et al. [105] indicates that the ultrafast demagnetization has main contributions from a mechanism, that transfers the angular momentum away from the spin system.

The spin-flip scattering mechanism, illustrated in Fig. 7.1(b), assumes that demagnetization occurs due to an enhancement of scattering processes, like electron-electron, electron-phonon, electron-magnon and direct spin-light interactions. These processes lead to a diminution of the spin order and imply a transfer of the angular momentum from the electronic spin to another subsystem, like the electromagnetic field, the lattice or the orbital angular momentum of the electrons. Measurements by Dalla Longa et al. [87] confirmed that the photon contribution to demagnetization is less than 0.01%. This excludes a direct transfer of angular momentum from the laser pulse. Early calculations by Zhang and Hübner [106] linked the ultrafast demagnetization to spin-orbit coupling. There has been evidence by Stamm et al. and Boeglin et al. [18, 86, 107], who performed experiments with femtosecond X-ray magnetic circular dichroism, that show a reduction of the angular momenta of electronic spins and orbitals within similar timescales. Furthermore, Stamm et al. [86] excluded that the electron orbit serves as a reservoir for angular momentum and inferred from their measurements the existence of a new kind of femtosecond spin-lattice relaxation path. This agrees with observations and simulations of Koopmans et al. [8, 108] who suggested Elliot-Yafet spin-flips as mechanism for an angular momentum transfer between the electron spin and the lattice system as

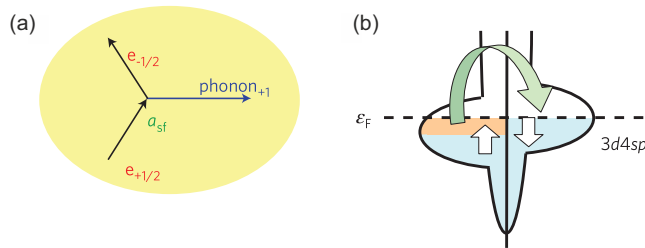


Figure 7.1: Visualization of the spin-flip scattering mechanism. (a) Elliot-Yaffet spin-flip process with a probability  $a_{sf}$  for emission or absorption of a phonon when an electron spin-flips from  $-1/2$  to  $1/2$ . (b) Spin-flip scattering illustrated in a density of states plot. The states of the 3d4sp band are filled to the fermi energy  $\epsilon_F$ . The difference between majority and minority spins depicts the uncompensated spins highlighted in orange. Figure 7.1 is reproduced from Koopmans et al. [8].

depicted in Fig. 7.1(a). This spin-flip channel describes the change of the electron spin by the emission of a phonon with angular momentum. With this model, the different demagnetization timescales observed for Ni and Gd can be explained [8]. Hennecke et al. [80] reported a transfer time of a few hundred femtoseconds for the spin and orbital angular momentum to the lattice in GdFeCo. A similar time scale was observed by Maldonado et al. [32] for Ni. On top of that Dornes et al. [11] reported about an ultrafast Einstein-de-Haas effect indicating strong evidence for a connection between the spin-flip process and the emission of phonons through a mechanical torque. However, simulations presented by Chen and Wang [20] point out a minor role to the electron-phonon coupling for the angular momentum transfer within femtoseconds, but attributed it to spin-orbit-coupling.

Hence, there is no comprehensive picture for the angular momentum conservation, yet. This thesis supports the approach of a transfer of the angular momentum to the lattice. We argue that rotating atomic motion by emission of a chiral phonon is the fundamental mechanism behind the angular momentum transfer from spin to lattice.

## 7.2 Asymmetry in electron diffraction

The experiments in this thesis are designed to answer one specific question: where is the angular momentum after demagnetization? As described in Chapter 1, there is a temporal gap between the loss of the magnetic order within femtosecond timescales as observed by Beaurepaire et al. [4] and the macroscopic specimen rotation due to angular momentum conservation as described with the Einstein-de-

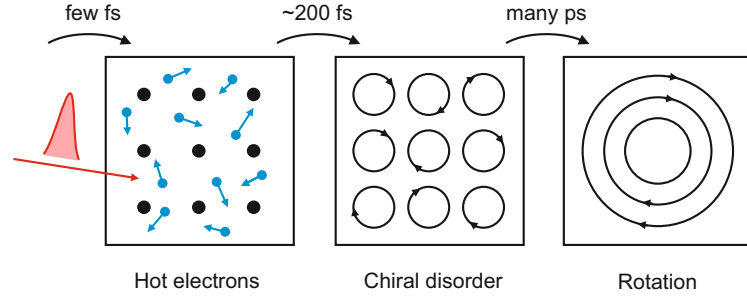


Figure 7.2: Idea of the angular momentum transfer process: Through absorption of light the energy gets transferred to the electron bath. Within a few femtoseconds the demagnetization sets in. Due to spin-orbit-coupling and electron-phonon coupling the angular momentum gets transferred to the lattice and the atoms start to rotate around their equilibrium position. After several picoseconds the chiral motion gets transferred to mechanical angular momentum as observed with the Einstein-de-Haas effect.

Haas effect [2, 3]. In our picture this loss gets transferred to atomic rotations. The angular momentum gets preserved by atoms rotating around their equilibrium position around an axis parallel to the magnetic field. The amplitude and magnitude of this rotation depends on the amount of the quenched spin angular momentum due to demagnetization. Hence, the angular momentum located in spins would be transferred to the lattice within hundreds of femtoseconds as phonons, before converting into mechanical angular motion after many picoseconds as presented in Fig. 7.2. Since we assume that the angular motion is transferred to the phonons, we choose to investigate the temporal lattice dynamics with ultrafast electron diffraction. By choosing the electron beam trajectory along the Ni[001]-axis, we are able to investigate lattice changes along the Ni[100] and Ni[010]-axis. With an in-plane magnetization along one of these axes we introduce an observable channel for anisotropic phonon distributions, as explained in the following: Due to thermal energy, atoms start to randomly move around their equilibrium position. As a result the Bragg spots created by the atomic grating start to blur and their peak intensity is reduced, as described by the Debye-Waller effect explained in Chapter 2.3. For a face-centered cubic solid like Ni the Ni(200), Ni( $\bar{2}00$ ), Ni(020) and Ni(0 $\bar{2}0$ ) peaks are equivalent within the Debye-Waller theory for thermal excitation of the crystal. Consequently, a thermal disorder of the lattice attenuates these Bragg peaks equally, as it is presented in Fig. 7.3(a). However, in the experimental setup depicted in Fig. 2.2 the Ni crystal is in dependence of the magnetic field. Due to the applied in-plane magnetization Ni(200) and Ni( $\bar{2}00$ ) have a differ-

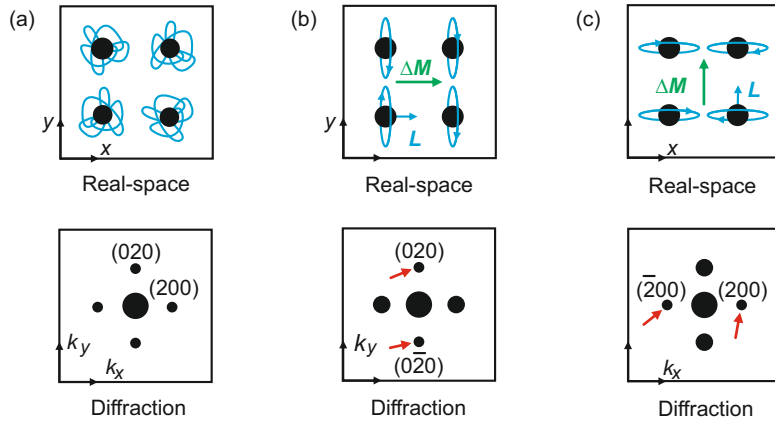


Figure 7.3: Comparison of atomic movement in real-space with the expected diffraction pattern in reciprocal space. The different spot sizes in the diffraction images represent the intensity. (a) For only thermal induced disorder all diffraction spots experience the same random movements (blue). (b,c) present the behavior of the diffraction pattern for an in-plane magnetization (green arrow) along  $x,y$ . Due to a rotational atomic movement (blue) induced by angular-momentum conservation Ni(200) and Ni(020) show a different intensity.

ent orientation to the magnetic field than Ni(020) and Ni(0 $\bar{2}$ 0). Hence, different Lorentz forces act on these pairs of Bragg spots. The Debye-Waller factor connects a change of a Bragg spots intensity with the random movement of atoms around their equilibrium position. The relation between the atomic displacement  $u_{x,y,z}$  and intensity  $I$  is

$$\frac{I}{I_0} = \left\langle \exp \left[ \frac{2\pi i}{a_{\text{Ni}}} \begin{pmatrix} h \\ k \\ l \end{pmatrix} \cdot \begin{pmatrix} u_x \\ u_y \\ u_z \end{pmatrix} \right] \right\rangle^2 \quad (7.1)$$

where  $\langle \rangle$  describes the average of the probed atomic grating,  $I_0$  is the intensity without disorder,  $a_{\text{Ni}} \approx 352$  pm denotes the lattice constant of Ni and  $h, k, l$  represent the Miller indices of the Bragg spot investigated. When one of the Miller indices in Eq. (7.1) is equal to 0 the Debye-Waller-factor is not influenced by the atomic movement along the associated dimension in real space. Consequently the Bragg peaks Ni(200) and Ni( $\bar{2}$ 00) only experience disorders along  $x = \text{Ni}[100]$ , while Ni(020) and Ni(0 $\bar{2}$ 0) along  $y = \text{Ni}[010]$ . Therefore, an anisotropic behavior of these spots expose nonthermal phonon dynamics in violation of equipartition. When the in-plane magnetization aligns with  $y$ , we can observe a displacement of the atoms along  $x$  and  $z = \text{Ni}[001]$ . Since the electron trajectory is chosen along the  $z$ -axis the diffraction pattern will only be sensitive to the rotational movement

along  $x$ . Hence, we can observe an asymmetry of intensity in the reciprocal lattice between Bragg peaks along the  $k_y$ -axis ( $\parallel y$ ) and  $k_x$ -axis ( $\parallel x$ ) as presented in Fig. 7.3(b-c). By combining the opposing Bragg spots and comparing the average intensity of Ni(200) and Ni( $\bar{2}00$ ) with the average intensity of Ni(020) and Ni(0 $\bar{2}0$ ) the analysis gets not affected by possible tilting or shearing of the crystal lattice. To confirm the dependence of the observed anisotropic behavior to the applied magnetic field, we rotate the in-plane magnetization by  $90^\circ$ . The results presented in Chapter 5.7 are in agreement with this theory and show a different anisotropic behavior in dependence of the orientation of the magnetic field. Since the inspected Bragg spots have crystallographic equivalence, the observed anisotropy reveals nonthermal phonon dynamics.

Our idea of an ultrafast angular momentum transfer to the lattice is based on the assumption of phonon angular momentum, revealed as chiral phonons [24, 25, 27]. The loss of magnetization due to the demagnetization of the material implies a loss of angular momentum. However, angular momentum is preserved and thus, it should be somewhere else. Our approach combines the theories of Dornes et al.[11] and Chen and Wang [20], as illustrated in Fig. 7.4: The laser excites the electron orbital, which then introduces a torque on the electronic spin due to spin-orbit-coupling. This results in a quenching of the magnetization [20]. Via spin-orbit-coupling this torque gets transferred back to the electron orbital and finally gets conveyed by electron-phonon-interactions to the lattice. This torque within the phonons could be realized with two different mechanisms: The first option is that all atoms get excited by the laser illumination. Consequently each atom starts

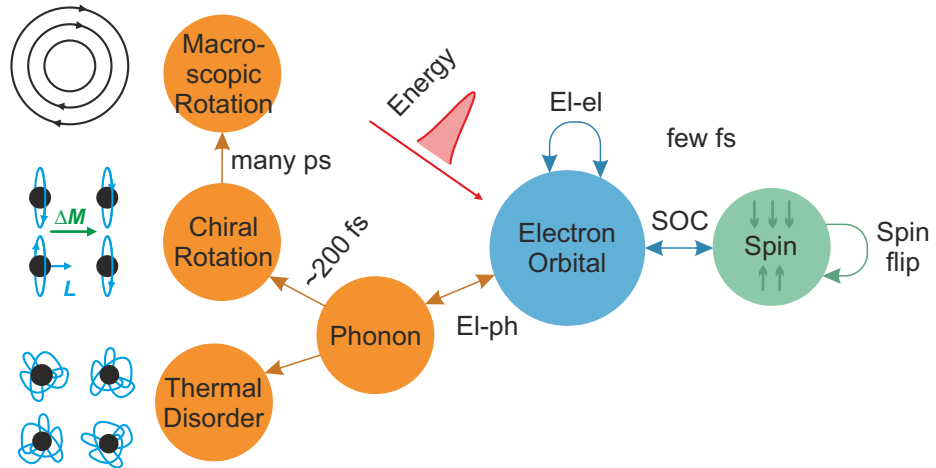


Figure 7.4: Scheme for a possible demagnetization process from laser excitation to mechanical rotation. Graphic inspired by Chen and Wang [20].

to move around its equilibrium position. With a considered demagnetization of  $D \approx 50\%$  as measured by Beaurepaire et al. [4] this would equal a spin angular momentum transfer of  $\approx 0.15 \hbar$  revealed in Eq. (6.3). This case is depicted in Fig. 7.5(a). The second option is that the laser absorption happens at localized atoms. In case of  $D \approx 50\%$  this would correspond to an angular momentum transfer to every seventh atom. Hence, these random localized atoms perceive a change in spin-angular momentum and start to rotate around their equilibrium position. Although only every seventh atom experiences a quenching of the magnetization, the torque can get transferred to the lattice due to short range interactions as Pauli repulsion and long range interactions like van der Waals interactions as shown in Fig. 7.5(b).

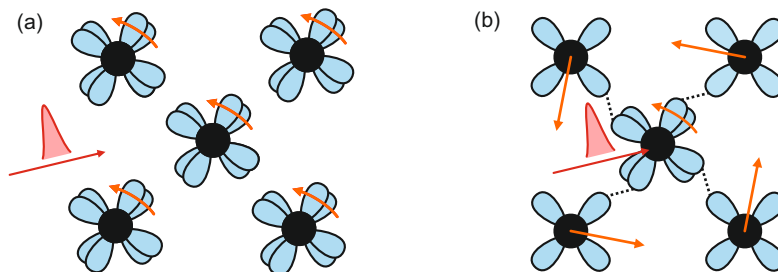


Figure 7.5: Different ways of exerting a torque within phonons. (a) All atoms get excited by photon illumination and consequently, all atoms start to move around their equilibrium position. (b) The photon gets absorbed at random localized atoms and only these experience a change in spin-angular momentum. Although only these random localized atoms start to move around their equilibrium position, the torque could get transferred to the complete lattice, due to short range and long range interactions.

### 7.3 Stepwise Einstein-de-Haas effect with chiral phonons

This thesis shows that ultrafast few-electron diffraction with terahertz-compressed pulses is capable of observing structural dynamics in complex materials. Through the limitation to few-electrons per pulse, space charge effects are avoided. The measurements within this thesis have shown that the combination of compressed single-electron pulses with ultrafast near-infrared pulses is an useful method for the observation of the light-induced movement of atoms in space and time. By

combining 95-fs near-infrared pump pulses at 1030 nm central wavelength and ultrafast electron diffraction with THz-compressed electron pulses as direct probe of lattice dynamics, we observe a reduction of diffraction intensity within 700 fs in agreement with the Debye-Waller-Effect. The time constant for the intensity decay is within hundreds of femtoseconds and thus in a similar time-regime to the demagnetization time of 120 – 300 fs reported by others [4, 8, 15, 43, 109]. This is an indication for the importance of phonons during the demagnetization process. Moreover, we report about the experimental observation of an introduced magnetic anisotropy within the isometric crystal lattice of Ni in dependence of an applied magnetic field. Our studies indicate an out-of-equilibrium population of anisotropic phonons, rotating perpendicular in dependence to their initial magnetization. The anisotropy of lattice disorder is observable as ratio of the similar Bragg spots  $I_{\{200\}}/I_{\{020\}} \approx 1 \pm 0.002$  emerging within  $< 500$  fs related to their orientation of a carefully chosen in-plane magnetic field. This break of crystal symmetry hints towards a localized excitation within a specific plane in dependence to the applied magnetic field. By averaging the centrosymmetric Bragg spots Ni(020) with Ni(0 $\bar{2}$ 0) and Ni(200) with Ni( $\bar{2}$ 00) the analyzed data is not affected by possible time-dependent variations of the Bragg condition, which could origin from a tilt or shear of the lattice. Our observation of ultrafast anisotropic disorder indicates that the angular momentum gets transferred locally to individual atoms or small domains. In the case that all atoms were exposed to equal forces, macroscopic strain waves at the speed of sound should occur and not transient atomic movement. A Pseudo-Voigt fit of the Bragg peaks did not reveal a deformation of the crystal nor gave an indication for transient strain waves.

From our results, we infer a transition of the angular momentum from the spin to the lattice by emission of anisotropic chiral motions. Due to photon absorption the atoms are exposed to non-equilibrium forces [110]. We suggest that angular momentum gets dissipated from the spin system, when the atoms of the lattice are accelerated to chiral motion. This would explain, why the demagnetization in Ni happens after a finite time span of roughly 120 – 300 fs [4, 8, 15, 43, 109], although the spin absorbs energy within 20 fs [15, 43]. However, electron diffraction can only observe the actual oscillation of the phonons and we argue that the demagnetization just needs their acceleration. Hence, the inferred time constants in Chapter 5.7 are upper limits for the transition time of the angular momentum to the phonons. The observed difference in the intensity between the Debye-Waller-Effect, which occurs due to thermal disorder, and the anisotropy, which occurs due to generation of chiral phonons, indicates that not all of the absorbed laser energy is used for the emergence of chiral phonons. A likely scenario for the residual energy is to heat the material. Thus, the emergence of chiral phonons would compete with the thermalization due to electron-phonon coupling. This

would expound, why different demagnetization rates and times are observed in other elements [8, 10, 12, 13] and why a higher demagnetization rate is obtained for an increased initial temperature [42].

We studied the temporal fluence dependence of Ni and report a linear increase of intensity loss and a stronger anisotropy with increasing laser fluence. An ultrafast electron diffraction analysis of the out-of-plane rocking curve confirms the X-ray out-of-plane rocking curve measurements done by Alexander Book in supervision of Dr. Wolfgang Kreuzpaintner and are in agreement with literature values for Cu and Ni thin-films of similar thickness [61]. Both results validate the epitaxial growth of the Ni crystal. Moreover, the slightly broad rocking curve, introduced by the atomic displacements of our growing procedure, implies that sub-unit-cell dynamics and atomic movements are examined. Hence, we can exclude that the experiment observes mechanical strain waves or torques. The investigation of the Si Bragg spots exposed no time-dependent intensity decay. This indicates that there is no spin-transport of the hot electrons from the Ni layer to the Si layer.

Our observations suggest, that spin-phonon interaction could be crucial for the transfer of the angular momentum to the lattice and that this interaction happens within hundreds of femtoseconds in form of chiral atomic motion. Consequently, chiral phonons could fill the temporal gap between ultrafast demagnetization performed within at least 120 – 300 fs for Ni [4, 8, 15, 42, 86] and mechanical rotation of the specimen. Thus, this work connects chiral phonons not only to materials with broken inversion symmetry [27, 111, 112] and to materials with a pseudogap phase [41], but also to the demagnetization of ferromagnets. The results can be interesting from a non fundamental-research point of view, since a sophisticated understanding of the demagnetization process can be helpful for the creation of spintronic devices, with enhanced speed and efficiency.

Simulations done in cooperation with Prof. Dr Ulrich Nowak and coworkers back up our assumption of the chiral phonon. They simulate an angular momentum within the crystal lattice, by distributing linear momentum and local displacement on arbitrarily chosen Ni atoms, without introducing a total momentum to the cubic crystal. The simulations show a similar intensity ratio and time-evolution as our measurements for an increasing amount of unit cells with open boundary conditions. Since the theoretical results of the Bragg spot anisotropies coincide well with our experimental measurements, we infer that chiral lattice motion is a feasible mechanism for transferring the angular momentum away from the spin system. Thus, our results agree with Dornes et al. [11] in regard to our observation of a sub-picosecond transfer of angular momentum to the lattice prior to macroscopic rotation. However, our conclusion on how this transfer proceeds is not by launching transverse strain waves, but by creating chiral phonons.

Single-electron, THz-compressed ultrafast electron diffraction has by the ad-

vances reported in this thesis become a valuable method to study primary light-matter interaction in complex materials at a time resolution well below the essential physics of electron-phonon coupling. The data presented dismiss therefore recent concerns against this approach [113].

## 7.4 Outlook

For future works, it would be interesting to investigate the asymmetry within other magnetic metals like iron or cobalt, but also magnetic alloys would be applicable. Especially, the theoretical and experimental analysis of gadolinium regarding chiral phonons could provide insights, since the 4f spin system mainly couples to the phonon heat bath [12].

The experiments presented in this work could be improved by growing a free standing sample of Ni similar to [32], to surely exclude any interactions of Ni with the sputtered seed layer of Cu or the Si membrane. Using significantly more electrons per pulse [44] would help to reduce the signal-to-noise ratio and refine the observation of the anisometry, but the current configuration of the ultrafast electron diffraction beam line would suffer from space charge effects. Nevertheless, it should be feasible to improve the observation of the intensity change since the observed asymmetry had a lifetime of at least several picoseconds. In order to prevent the oxidation of the top Ni layers to  $\text{NiO}_x$  it could be helpful to add an additional capping layer. However, the material needs to be chosen carefully, since it should be non-magnetic and be invisible to the applied pump and probe beam. In our experiments, we compared our pump fluence to literature values and deduced a demagnetization of 50%. This was supported by the predicted asymmetry calculated by the theoretical physicists and by an independently executed time-dependent Magneto-optical Faraday rotation experiment under similar conditions. To experimentally confirm the amount of demagnetization of the Ni layer, it would be helpful to measure the spin dynamics simultaneously to the ultrafast electron diffraction experiment. This could be realized by analyzing the reflected pump beam with time resolved magneto-optical Kerr effect measurements. Since the topic of the angular momentum transfer after demagnetization is strongly discussed since 20 years, more than one type of observation of the chiral phonon would be helpful to substantiate our theory. Although simulations and measurements agree, there have been several theories how the angular momentum transfer might happen in the last two decades. In this dissertation the chiral phonons were only indirectly observed by creating an anisotropy and comparing crystallographically equivalent Bragg spots. A direct observation would be helpful to elucidate the creation of chiral phonons as successive step to the demagnetization of the atoms and prior to mechanical rotation. One way to directly observe the chiral

---

phonon could be circular dichroism, as it was performed by Zhu et al. [27]. Since the experiment in this thesis was inspired by the Einstein-de Haas effect, it might be interesting to investigate, if a chiral lattice motion would induce a magnetic field. This would correspond to the atomistic version of the Barnett effect.



# Data archiving

The location of the experimental raw data, evaluation files, and original figures of this thesis are given in a `read_me.txt` at the Data Archive Server of the Laboratory for Attosecond Physics at the Max Planck Institute of Quantum Optics:

`/afs/ipp-garching.mpg.de/mpq/lap/publication_archive`

The main folder `Theses/2021/Tauchert, Sonja (PhD)` contains a link with the destination of the data preservation. Due to the big amount of data, the experimental raw data, evaluation files and original figures could not be saved directly on the server.



# Bibliography

- [1] Barnett, S. J. (1915). Magnetization by Rotation. *Physical Review*. **6** (4), pp. 239–270. <https://www.doi.org/10.1103/PhysRev.6.239>.
- [2] Einstein, A. & de Haas, W. J. (1915). Experimenteller Nachweis der Ampèreschen Molekularströme. *Deutsche Physikalische Gesellschaft*. **17**, pp. 152–170.
- [3] Frenkel', V. Y. (1979). On the history of the Einstein–de Haas effect. *Soviet Physics Uspekhi*. **22** (7), pp. 580–587. <https://doi.org/10.1070/pu1979v022n07abeh005587>.
- [4] Beaupaire, E., Merle, J.-C., Daunois, A. & Bigot, J.-Y. (1996). Ultrafast Spin Dynamics in Ferromagnetic Nickel. *Physical Review Letters*. **76** (22), pp. 4250–4253. <https://www.doi.org/10.1103/PhysRevLett.76.4250>.
- [5] Kryder, M. H. (1985). Magneto-optic recording technology (invited). *Journal of Applied Physics*. **57** (8), pp. 3913–3918. <https://doi.org/10.1063/1.334915>.
- [6] Stöhr, J. & Siegmann, H. C. (2006). *Ultrafast Magnetization Dynamics in Magnetism: From Fundamentals to Nanoscale Dynamics*. Springer Berlin Heidelberg, Berlin, Heidelberg. ISBN: 978-3-540-30283-4. [https://doi.org/10.1007/978-3-540-30283-4\\_15](https://doi.org/10.1007/978-3-540-30283-4_15).
- [7] Kirilyuk, A., Kimel, A. V. & Rasing, T. (2010). Ultrafast optical manipulation of magnetic order. *Reviews of Modern Physics*. **82** (3), pp. 2731–2784. <https://doi.org/10.1103/RevModPhys.82.2731>. (2016). Erratum: Ultrafast optical manipulation of magnetic order [Rev. Mod. Phys. 82, 2731 (2010)]. *Reviews of Modern Physics*. **88** (3), p. 039904. <https://doi.org/10.1103/RevModPhys.88.039904>.

- [8] Koopmans, B., Malinowski, G., Dalla Longa, F., Steiauf, D., Fähnle, M., Roth, T., Cinchetti, M. & Aeschlimann, M. (2010). Explaining the paradoxical diversity of ultrafast laser-induced demagnetization. *Nature Materials*. **9** (3), pp. 259–265. ISSN: 1476-4660. <https://doi.org/10.1038/nmat2593>.
- [9] Graves, C. E., Reid, A. H., Wang, T., Wu, B., de Jong, S., Vahaplar, K., Radu, I., Bernstein, D. P., Messerschmidt, M., Müller, L., Coffee, R., Bionta, M., Epp, S. W., Hartmann, R., Kimmel, N., Hauser, G., Hartmann, A., Holl, P., Gorke, H., Mentink, J. H., Tsukamoto, A., Fognini, A., Turner, J. J., Schlotter, W. F., Rolles, D., Soltau, H., Strüder, L., Acremann, Y., Kimel, A. V., Kirilyuk, A., Rasing, T., Stöhr, J., Scherz, A. O. & Dürr, H. A. (2013). Nanoscale spin reversal by non-local angular momentum transfer following ultrafast laser excitation in ferrimagnetic GdFeCo. *Nature Materials*. **12** (4), pp. 293–298. ISSN: 1476-4660. <https://doi.org/10.1038/nmat3597>.
- [10] Wietstruk, M., Melnikov, A., Stamm, C., Kachel, T., Pontius, N., Sultan, M., Gahl, C., Weinelt, M., Dürr, H. A. & Bovensiepen, U. (2011). Hot-Electron-Driven Enhancement of Spin-Lattice Coupling in Gd and Tb 4f Ferromagnets Observed by Femtosecond X-Ray Magnetic Circular Dichroism. *Physical Review Letters*. **106** (12), p. 127401. <https://doi.org/10.1103/PhysRevLett.106.127401>.
- [11] Dornes, C., Acremann, Y., Savoini, M., Kubli, M., Neugebauer, M., Huber, L., Lantz, G., Vaz, C., Lemke, H., Bothschafter, E., Porer, M., Esposito, V., Rettig, L., Buzzi, M., Alberca, A., Windsor, Y., Beaud, P., Staub, U. & Johnson, S. (2019). The Ultrafast Einstein-De Haas Effect. *Nature*. **565** (7738), pp. 209–212. ISSN: 14764687. <http://doi.org/10.1038/s41586-018-0822-7>.
- [12] Frietsch, B., Bowlan, J., Carley, R., Teichmann, M., Wienholdt, S., Hinzke, D., Nowak, U., Carva, K., Oppeneer, P. M. & Weinelt, M. (2015). Disparate ultrafast dynamics of itinerant and localized magnetic moments in gadolinium metal. *Nature Communications*. **6** (1), p. 8262. ISSN: 2041-1723. <https://doi.org/10.1038/ncomms9262>.
- [13] Frietsch, B., Donges, A., Carley, R., Teichmann, M., Bowlan, J., Döbrich, K., Carva, K., Legut, D., Oppeneer, P. M., Nowak, U. & Weinelt, M. (2020). The role of ultrafast magnon generation in the magnetization dynamics of rare-earth metals. *Science Advances*. **6** (39). <https://doi.org/10.1126/sciadv.abb1601>.
- [14] Von Korff Schmising, C., Pfau, B., Schneider, M., Günther, C. M., Giovannella, M., Perron, J., Vodungbo, B., Müller, L., Capotondi, F., Pedersoli, E., Mahne, N., Lüning, J. & Eisebitt, S. (2014). Imaging Ultrafast Demagnetization Dynamics after a Spatially Localized Optical Excitation. *Physical*

- Review Letters*. **112** (21), p. 217203. <https://doi.org/10.1103/PhysRevLett.112.217203>.
- [15] Tengdin, P., You, W., Chen, C., Shi, X., Zusin, D., Zhang, Y., Gentry, C., Blonsky, A., Keller, M., Oppeneer, P. M., Kapteyn, H. C., Tao, Z. & Murnane, M. M. (2018). Critical behavior within 20 fs drives the out-of-equilibrium laser-induced magnetic phase transition in nickel. *Science Advances*. **4** (3). <https://doi.org/10.1126/sciadv.aap9744>.
- [16] Koopmans, B., van Kampen, M. & de Jonge, W. J. M. (2003). Experimental access to femtosecond spin dynamics. *Journal of Physics: Condensed Matter*. **15** (5), S723–S736. <https://doi.org/10.1088/0953-8984/15/5/324>.
- [17] Battiato, M., Carva, K. & Oppeneer, P. M. (2010). Superdiffusive Spin Transport as a Mechanism of Ultrafast Demagnetization. *Physical Review Letters*. **105** (2), p. 027203. <https://doi.org/10.1103/PhysRevLett.105.027203>.
- [18] Boeglin, C., Beaurepaire, E., Halté, V., López-Flores, V., Stamm, C., Pontius, N., Dürr, H. A. & Bigot, J. Y. (2010). Distinguishing the ultrafast dynamics of spin and orbital moments in solids. *Nature*. **465** (7297), pp. 458–461. ISSN: 14764687. <https://doi.org/10.1038/nature09070>.
- [19] Carpene, E., Mancini, E., Dallera, C., Brenna, M., Puppini, E. & De Silvestri, S. (2008). Dynamics of electron-magnon interaction and ultrafast demagnetization in thin iron films. *Physical Review B*. **78** (17), p. 174422. <https://doi.org/10.1103/PhysRevB.78.174422>.
- [20] Chen, Z. & Wang, L.-W. (2019). Role of initial magnetic disorder: A time-dependent ab initio study of ultrafast demagnetization mechanisms. *Science Advances*. **5** (6). <https://doi.org/10.1126/sciadv.aau8000>.
- [21] Eschenlohr, A., Battiato, M., Maldonado, P., Pontius, N., Kachel, T., Holl-dack, K., Mitzner, R., Föhlisch, A., Oppeneer, P. M. & Stamm, C. (2013). Ultrafast spin transport as key to femtosecond demagnetization. *Nature Materials*. **12** (4), pp. 332–336. ISSN: 1476-4660. <https://doi.org/10.1038/nmat3546>.
- [22] Krauß, M., Roth, T., Alebrand, S., Steil, D., Cinchetti, M., Aeschlimann, M. & Schneider, H. C. (2009). Ultrafast demagnetization of ferromagnetic transition metals: The role of the Coulomb interaction. *Physical Review B*. **80** (18), p. 180407. <https://doi.org/10.1103/PhysRevB.80.180407>.
- [23] Zhang, G. P., Murakami, M., Bai, Y. H., George, T. F. & Wu, X. S. (2019). Spin-orbit torque-mediated spin-wave excitation as an alternative paradigm for femtomagnetism. *Journal of Applied Physics*. **126** (10), p. 103906. <https://doi.org/10.1063/1.5110522>.

- [24] Garanin, D. A. & Chudnovsky, E. M. (2015). Angular momentum in spin-phonon processes. *Physical Review B*. **92** (2), p. 024421. <https://doi.org/10.1103/PhysRevB.92.024421>.
- [25] Zhang, L. & Niu, Q. (2014). Angular Momentum of Phonons and the Einstein–de Haas Effect. *Physical Review Letters*. **112** (8), p. 085503. <https://doi.org/10.1103/PhysRevLett.112.085503>.
- [26] Zhang, L. & Niu, Q. (2015). Chiral Phonons at High-Symmetry Points in Monolayer Hexagonal Lattices. *Physical Review Letters*. **115** (11), p. 115502. <https://doi.org/10.1103/PhysRevLett.115.115502>.
- [27] Zhu, H., Yi, J., Li, M.-Y., Xiao, J., Zhang, L., Yang, C.-W., Kaindl, R. A., Li, L.-J., Wang, Y. & Zhang, X. (2018). Observation of chiral phonons. *Science*. **359** (6375), pp. 579–582. ISSN: 0036-8075. <https://doi.org/10.1126/science.aar2711>.
- [28] Chen, H., Zhang, W., Niu, Q. & Zhang, L. (2018). Chiral phonons in two-dimensional materials. *2D Materials*. **6** (1), p. 012002. <https://doi.org/10.1088/2053-1583/aaf292>.
- [29] Kittel, C. (1949). On the Gyromagnetic Ratio and Spectroscopic Splitting Factor of Ferromagnetic Substances. *Physical Review*. **76** (6), pp. 743–748. <https://www.doi.org/10.1103/PhysRev.76.743>.
- [30] Matsuo, M., Ieda, J. & Maekawa, S. (2015). Mechanical generation of spin current. *Frontiers in Physics*. **3**, p. 54. ISSN: 2296-424X. <https://doi.org/10.3389/fphy.2015.00054>.
- [31] Vaterlaus, A., Beutler, T. & Meier, F. (1991). Spin-lattice relaxation time of ferromagnetic gadolinium determined with time-resolved spin-polarized photoemission. *Physical Review Letters*. **67** (23), pp. 3314–3317. <https://doi.org/10.1103/PhysRevLett.67.3314>.
- [32] Maldonado, P., Chase, T., Reid, A. H., Shen, X., Li, R. K., Carva, K., Payer, T., Horn von Hoegen, M., Sokolowski-Tinten, K., Wang, X. J., Oppeneer, P. M. & Dürr, H. A. (2020). Tracking the ultrafast nonequilibrium energy flow between electronic and lattice degrees of freedom in crystalline nickel. *Physical Review B*. **101** (10), p. 100302. <https://doi.org/10.1103/PhysRevB.101.100302>.
- [33] Zhang, G., Hübner, W., Beaurepaire, E. & Bigot, J.-Y. (2002). *Laser-Induced Ultrafast Demagnetization: Femtomagnetism, a New Frontier?* (eds Hillebrands, B. & Ounadjela, K.) in *Spin Dynamics in Confined Magnetic Structures I*. Springer Berlin Heidelberg, Berlin, Heidelberg. ISBN: 978-3-540-40907-6. [https://doi.org/10.1007/3-540-40907-6\\_8](https://doi.org/10.1007/3-540-40907-6_8).

- [34] Gross, R. & Marx, A. (09 Jan. 2018). Festkörperphysik. De Gruyter, Berlin, Boston. ISBN: 978-3-11-055918-7. <https://doi.org/10.1515/9783110559187>.
- [35] Chen, H., Wu, W., Yang, S. A., Li, X. & Zhang, L. (2019). Chiral phonons in kagome lattices. *Physical Review B*. **100** (9), p. 094303. <https://doi.org/10.1103/PhysRevB.100.094303>.
- [36] Pandey, T., Polanco, C. A., Cooper, V. R., Parker, D. S. & Lindsay, L. (2018). Symmetry-driven phonon chirality and transport in one-dimensional and bulk Ba<sub>3</sub>N-derived materials. *Physical Review B*. **98** (24), p. 241405. <https://doi.org/10.1103/PhysRevB.98.241405>.
- [37] Romao, C. P. (2019). Anomalous thermal expansion and chiral phonons in BiB<sub>3</sub>O<sub>6</sub>. *Physical Review B*. **100** (6), p. 060302. <https://doi.org/10.1103/PhysRevB.100.060302>.
- [38] Xu, X., Chen, H. & Zhang, L. (2018). Nondegenerate chiral phonons in the Brillouin-zone center of  $\sqrt{3} \times \sqrt{3}$  honeycomb superlattices. *Physical Review B*. **98** (13), p. 134304. <https://doi.org/10.1103/PhysRevB.98.134304>.
- [39] Zhang, W., Srivastava, A., Li, X. & Zhang, L. (2020). Chiral phonons in the indirect optical transition of a MoS<sub>2</sub>/WS<sub>2</sub> heterostructure. *Physical Review B*. **102** (17), p. 174301. <https://doi.org/10.1103/PhysRevB.102.174301>.
- [40] Chen, X., Lu, X., Dubey, S., Yao, Q., Liu, S., Wang, X., Xiong, Q., Zhang, L. & Srivastava, A. (2019). Entanglement of single-photons and chiral phonons in atomically thin WSe<sub>2</sub>. *Nature Physics*. **15** (3), pp. 221–227. ISSN: 1745-2481. <https://doi.org/10.1038/s41567-018-0366-7>.
- [41] Grissonnanche, G., Thériault, S., Gourgout, A., Boulanger, M.-E., Lefrançois, E., Ataei, A., Laliberté, F., Dion, M., Zhou, J.-S., Pyon, S., Takayama, T., Takagi, H., Doiron-Leyraud, N. & Taillefer, L. (2020). Chiral phonons in the pseudogap phase of cuprates. *Nature Physics*. **16** (11), pp. 1108–1111. ISSN: 1745-2481. <https://doi.org/10.1038/s41567-020-0965-y>.
- [42] Roth, T., Schellekens, A. J., Alebrand, S., Schmitt, O., Steil, D., Koopmans, B., Cinchetti, M. & Aeschlimann, M. (2012). Temperature Dependence of Laser-Induced Demagnetization in Ni: A Key for Identifying the Underlying Mechanism. *Physical Review X*. **2** (2), p. 021006. <https://doi.org/10.1103/PhysRevX.2.021006>.

- [43] You, W., Tengdin, P., Chen, C., Shi, X., Zusin, D., Zhang, Y., Gentry, C., Blonsky, A., Keller, M., Oppeneer, P. M., Kapteyn, H., Tao, Z. & Murnane, M. (2018). Revealing the Nature of the Ultrafast Magnetic Phase Transition in Ni by Correlating Extreme Ultraviolet Magneto-Optic and Photoemission Spectroscopies. *Physical Review Letters*. **121** (7), p. 077204. <https://doi.org/10.1103/PhysRevLett.121.077204>.
- [44] Waldecker, L., Bertoni, R. & Ernstorfer, R. (2015). Compact femtosecond electron diffractometer with 100 keV electron bunches approaching the single-electron pulse duration limit. *Journal of Applied Physics*. **117** (4), p. 044903. <https://doi.org/10.1063/1.4906786>.
- [45] Ehberger, D., Mohler, K. J., Vasileiadis, T., Ernstorfer, R., Waldecker, L. & Baum, P. (2019). Terahertz Compression of Electron Pulses at a Planar Mirror Membrane. *Physical Review Applied*. **11** (2), p. 024034. <https://doi.org/10.1103/PhysRevApplied.11.024034>.
- [46] Ehberger, D., Kealhofer, C. & Baum, P. (2018). Electron energy analysis by phase-space shaping with THz field cycles. *Structural Dynamics*. **5** (4), p. 044303. <https://doi.org/10.1063/1.5045167>.
- [47] Kealhofer, C., Schneider, W., Ehberger, D., Ryabov, A., Krausz, F. & Baum, P. (2016). All-optical control and metrology of electron pulses. *Science*. **352** (6284), pp. 429–433. ISSN: 0036-8075. <https://doi.org/10.1126/science.aae0003>.
- [48] Kreier, D., Sabonis, D. & Baum, P. (2014). Alignment of magnetic solenoid lenses for minimizing temporal distortions. *Journal of Optics*. **16** (7), p. 075201. <https://doi.org/10.1088/2040-8978/16/7/075201>.
- [49] Williams, D. & Carter, C. (2009). Transmission Electron Microscopy: A Textbook for Materials Science. ISBN: 9780387765020. <https://www.doi.org/10.1007/978-1-4757-2519-3>.
- [50] Seidel, M., Brons, J., Arisholm, G., Fritsch, K., Pervak, V. & Pronin, O. (2017). Efficient High-Power Ultrashort Pulse Compression in Self-Defocusing Bulk Media. *Scientific Reports*. **7** (1), p. 1410. ISSN: 2045-2322. <https://doi.org/10.1038/s41598-017-01504-x>.
- [51] Kasmi, L., Kreier, D., Bradler, M., Riedle, E. & Baum, P. (2015). Femtosecond single-electron pulses generated by two-photon photoemission close to the work function. *New Journal of Physics*. **17** (3), p. 033008. <https://doi.org/10.1088/1367-2630/17/3/033008>.

- [52] Baum, P. (2013). On the physics of ultrashort single-electron pulses for time-resolved microscopy and diffraction. *Chemical Physics*. **423**, pp. 55–61. ISSN: 0301-0104. <https://doi.org/10.1016/j.chemphys.2013.06.012>.
- [53] Tsarev, M. V., Ehberger, D. & Baum, P. (2016). High-average-power, intense THz pulses from a LiNbO<sub>3</sub> slab with silicon output coupler. *Applied Physics B: Lasers and Optics*. **122** (2), p. 30. ISSN: 1432-0649. <https://doi.org/10.1007/s00340-015-6315-6>.
- [54] Ehberger, D., Ryabov, A. & Baum, P. (2018). Tilted Electron Pulses. *Physical Review Letters*. **121** (9), p. 094801. <https://doi.org/10.1103/PhysRevLett.121.094801>.
- [55] Gliserin, A., Walbran, M., Krausz, F. & Baum, P. (2015). Sub-phonon-period compression of electron pulses for atomic diffraction. *Nature Communications*. **6** (1), p. 8723. ISSN: 2041-1723. <https://doi.org/10.1038/ncomms9723>.
- [56] Kirchner, F. O., Gliserin, A., Krausz, F. & Baum, P. (2014). Laser streaking of free electrons at 25 keV. *Nature Photonics*. **8** (1), pp. 52–57. ISSN: 1749-4893. <https://doi.org/10.1038/nphoton.2013.315>.
- [57] Weninger, C. & Baum, P. (2012). Temporal distortions in magnetic lenses. *Ultramicroscopy*. **113**, pp. 145–151. ISSN: 0304-3991. <https://doi.org/10.1016/j.ultramic.2011.11.018>.
- [58] Otiti, T. (2004). Anisotropic magnetic properties of obliquely deposited Ni films. *Journal of Materials Science*. **39** (2), pp. 477–480. ISSN: 1573-4803. <https://doi.org/10.1023/B:JMISC.0000011501.36257.cd>.
- [59] Schmehl, A., Mairoser, T., Herrnberger, A., Stephanos, C., Meir, S., Förg, B., Wiedemann, B., Böni, P., Mannhart, J. & Kreuzpaintner, W. (2018). Design and realization of a sputter deposition system for the in situ- and in operando-use in polarized neutron reflectometry experiments. *Nuclear Instruments and Methods in Physics Research Section A: Accelerators, Spectrometers, Detectors and Associated Equipment*. **883**, pp. 170–182. ISSN: 0168-9002. <https://doi.org/10.1016/j.nima.2017.11.086>.
- [60] Ye, J., Book, A., Mayr, S., Gabold, H., Meng, F., Schäfferer, H., Need, R., Gilbert, D., Saerbeck, T., Stahn, J., Böni, P. & Kreuzpaintner, W. (2020). Design and realization of a sputter deposition system for the in situ and in operando use in polarized neutron reflectometry experiments: Novel capabilities. *Nuclear Instruments and Methods in Physics Research Section A: Accelerators, Spectrometers, Detectors and Associated Equipment*. **964**,

- p. 163710. ISSN: 0168-9002. <https://doi.org/10.1016/j.nima.2020.163710>.
- [61] Kreuzpaintner, W., Störmer, M., Lott, D., Solina, D. & Schreyer, A. (2008). Epitaxial growth of nickel on Si(100) by dc magnetron sputtering. *Journal of Applied Physics*. **104** (11), p. 114302. <https://doi.org/10.1063/1.3032383>.
- [62] Hirashita, N., Kinoshita, M., Aikawa, I. & Ajioka, T. (1990). Effects of surface hydrogen on the air oxidation at room temperature of HF-treated Si (100) surfaces. *Applied Physics Letters*. **56** (5), pp. 451–453. <https://doi.org/10.1063/1.102762>.
- [63] Ji, J.-Y. & Shen, T.-C. (2004). Low-temperature silicon epitaxy on hydrogen-terminated Si(001) surfaces. *Physical Review B*. **70** (11), p. 115309. <https://doi.org/10.1103/PhysRevB.70.115309>.
- [64] Jiang, H., Klemmer, T. J., Barnard, J. A. & Payzant, E. A. (1998). Epitaxial growth of Cu on Si by magnetron sputtering. *Journal of Vacuum Science & Technology A*. **16** (6), pp. 3376–3383. <https://doi.org/10.1116/1.581489>.
- [65] Chang, C.-A. (1990). Reversed magnetic anisotropy in deformed (100) Cu/Ni/Cu structures. *Journal of Applied Physics*. **68** (9), pp. 4873–4875. <https://doi.org/10.1063/1.346127>.
- [66] Chang, C.-A. (1991). Reversal in magnetic anisotropy of (100)Cu-Ni superlattices. *Journal of Magnetism and Magnetic Materials*. **97** (1), pp. 102–106. ISSN: 0304-8853. [https://doi.org/10.1016/0304-8853\(91\)90166-8](https://doi.org/10.1016/0304-8853(91)90166-8).
- [67] Kiessig, H. (1931). Interferenz von Röntgenstrahlen an dünnen Schichten. *Annalen der Physik*. **402** (7), pp. 769–788. <https://doi.org/10.1002/andp.19314020702>.
- [68] Björck, M. & Andersson, G. (2007). *GenX*: an extensible X-ray reflectivity refinement program utilizing differential evolution. *Journal of Applied Crystallography*. **40** (6), pp. 1174–1178. <https://doi.org/10.1107/S0021889807045086>.
- [69] Hull, C. M. & Switzer, J. A. (2018). Electrodeposited Epitaxial Cu(100) on Si(100) and Lift-Off of Single Crystal-like Cu(100) Foils. *ACS Applied Materials & Interfaces*. **10** (44). PMID: 30335962, pp. 38596–38602. <https://doi.org/10.1021/acsami.8b13188>.
- [70] Warren, B. E. (1990). X-Ray Diffraction. Dover Publications Inc., New York. ISBN: 0-486-66317-5.

- [71] Fiévet, F., Germi, P., de Bergevin, F. & Figlarz, M. (1979). Lattice parameter, microstrains and non-stoichiometry in NiO. Comparison between mosaic microcrystals and quasi-perfect single microcrystals. *Journal of Applied Crystallography*. **12** (4), pp. 387–394. <https://doi.org/10.1107/S0021889879012747>.
- [72] Rajkovic, V., Bozic, D. & Jovanovic, M. T. (2008). Properties of copper matrix reinforced with nano- and micro-sized Al<sub>2</sub>O<sub>3</sub> particles. *Journal of Alloys and Compounds*. **459** (1), pp. 177–184. ISSN: 0925-8388. <https://doi.org/10.1016/j.jallcom.2007.04.307>.
- [73] Ida, T., Ando, M. & Toraya, H. (2000). Extended pseudo-Voigt function for approximating the Voigt profile. *Journal of Applied Crystallography*. **33** (6), pp. 1311–1316. <https://doi.org/10.1107/S0021889800010219>.
- [74] Thompson, P., Cox, D. E. & Hastings, J. B. (1987). Rietveld refinement of Debye–Scherrer synchrotron X-ray data from Al<sub>2</sub>O<sub>3</sub>. *Journal of Applied Crystallography*. **20** (2), pp. 79–83. <https://doi.org/10.1107/S0021889887087090>.
- [75] González Vallejo, I., Gallé, G., Arnaud, B., Scott, S. A., Lagally, M. G., Boschetto, D., Coulon, P.-E., Rizza, G., Houdellier, F., Le Bolloc'h, D. & Faure, J. (2018). Observation of large multiple scattering effects in ultrafast electron diffraction on monocrystalline silicon. *Physical Review B*. **97** (5), p. 054302. <https://doi.org/10.1103/PhysRevB.97.054302>.
- [76] Morimoto, Y. & Baum, P. (2018). Diffraction and microscopy with attosecond electron pulse trains. *Nature Physics*. **14** (3), pp. 252–256. ISSN: 1745-2481. <https://doi.org/10.1038/s41567-017-0007-6>.
- [77] Ligges, M., Rajkovic, I., Zhou, P., Posth, O., Hassel, C., Dumpich, G. & von der Linde, D. (2009). Observation of ultrafast lattice heating using time resolved electron diffraction. *Applied Physics Letters*. **94** (10), p. 101910. <https://doi.org/10.1063/1.3095497>.
- [78] VandenBussche, E. J. & Flannigan, D. J. (2019). Sources of error in Debye–Waller-effect measurements relevant to studies of photoinduced structural dynamics. *Ultramicroscopy*. **196**, pp. 111–120. ISSN: 0304-3991. <https://doi.org/10.1016/j.ultramic.2018.10.002>.
- [79] Wei, L., Sun, S., Guo, C., Li, Z., Sun, K., Liu, Y., Lu, W., Sun, Y., Tian, H., Yang, H. & Li, J. (2017). Dynamic diffraction effects and coherent breathing oscillations in ultrafast electron diffraction in layered 1T-TaSeTe. *Structural Dynamics*. **4** (4), p. 044012. <https://doi.org/10.1063/1.4979643>.

- [80] Hennecke, M., Radu, I., Abrudan, R., Kachel, T., Holldack, K., Mitzner, R., Tsukamoto, A. & Eisebitt, S. (2019). Angular Momentum Flow During Ultrafast Demagnetization of a Ferrimagnet. *Physical Review Letters*. **122** (15), p. 157202. <https://www.doi.org/10.1103/PhysRevLett.122.157202>.
- [81] Agranat, M. B., Ashitkov, S., Granovskii, A. B. & Rukman, G. (1984). Interaction of picosecond laser pulses with the electron, spin, and phonon subsystems of nickel. *Journal of Experimental and Theoretical Physics (JETP)*. **59** (4), pp. 804–806.
- [82] Simerská, M. (1962). The temperature dependence of the characteristic temperature of nickel. *Czechoslovakij fiziceskij zurnal B*. **12** (11), pp. 858–859. ISSN: 1572-9486. <https://doi.org/10.1007/BF01689711>.
- [83] Miyake, S. & Uyeda, R. (1955). Friedel's law in the dynamical theory of diffraction. *Acta Crystallographica*. **8** (6), pp. 335–342. <https://doi.org/10.1107/S0365110X55001023>.
- [84] Qian, Q., Shen, X., Luo, D., Jia, L., Kozina, M., Li, R., Lin, M.-F., Reid, A. H., Weathersby, S., Park, S., Yang, J., Zhou, Y., Zhang, K., Wang, X. & Huang, S. (2020). Coherent Lattice Wobbling and Out-of-Phase Intensity Oscillations of Friedel Pairs Observed by Ultrafast Electron Diffraction. *ACS Nano*. **14** (7). PMID: 32538617, pp. 8449–8458. <https://doi.org/10.1021/acsnano.0c02643>.
- [85] Xiong, D., Lu, L., Wang, J., Zhao, D. & Sun, Y. (2013). Non-centrosymmetric electron diffraction pattern of icosahedral quasicrystal induced by combination of linear phason strain and curvature of Ewald sphere. *Micron*. **52-53**, pp. 45–48. ISSN: 0968-4328. <https://doi.org/10.1016/j.micron.2013.08.004>.
- [86] Stamm, C., Kachel, T., Pontius, N., Mitzner, R., Quast, T., Holldack, K., Khan, S., Lupulescu, C., Aziz, E. F., Wietstruk, M., Dürr, H. A. & Eberhardt, W. (2007). Femtosecond modification of electron localization and transfer of angular momentum in nickel. *Nature Materials*. **6** (10), pp. 740–743. ISSN: 14764660. <https://doi.org/10.1038/nmat1985>.
- [87] Dalla Longa, F., Kohlhepp, J. T., de Jonge, W. J. M. & Koopmans, B. (2007). Influence of photon angular momentum on ultrafast demagnetization in nickel. *Physical Review B*. **75** (22), p. 224431. <https://doi.org/10.1103/PhysRevB.75.224431>.
- [88] Kim, J.-W., Vomir, M. & Bigot, J.-Y. (2012). Ultrafast Magnetoacoustics in Nickel Films. *Physical Review Letters*. **109** (16), p. 166601. <https://doi.org/10.1103/PhysRevLett.109.166601>.

- [89] Wang, X., Nie, S., Li, J., Clinite, R., Clark, J. E. & Cao, J. (2010). Temperature dependence of electron-phonon thermalization and its correlation to ultrafast magnetism. *Physical Review B*. **81** (22), p. 220301. <https://doi.org/10.1103/PhysRevB.81.220301>.
- [90] Anisimov, S., Kapeliovick, B. & Perelman, T. (1974). Electron emission from metal surfaces exposed to ultra-short laser pulses. *Journal of Experimental and Theoretical Physics (JETP)*. **66**, pp. 776–781.
- [91] Kaganov, M. I., Lifshitz, I. M. & Tantarov, L. V. (1957). Relaxation between Electrons and the Crystalline Lattice. *Zhurnal Eksperimental'noi i Teoreticheskoi Fiziki*. **31** (2), p. 232. <http://jetp.ac.ru/cgi-bin/e/index/e/4/2/p173?a=list>. [Journal of Experimental and Theoretical Physics (JETP) **4**. 173–178 (1978)].
- [92] Kazantseva, N., Nowak, U., Chantrell, R. W., Hohlfeld, J. & Rebei, A. (2007). Slow recovery of the magnetisation after a sub-picosecond heat pulse. *EPL (Europhysics Letters)*. **81** (2), p. 27004. <https://doi.org/10.1209/0295-5075/81/27004>.
- [93] Maldonado, P., Carva, K., Flammer, M. & Oppeneer, P. M. (2017). Theory of out-of-equilibrium ultrafast relaxation dynamics in metals. *Physical Review B*. **96** (17), p. 174439. <https://doi.org/10.1103/PhysRevB.96.174439>.
- [94] Lange, H. (2020). *Computer Simulations of Ultrafast Phonon Phenomena in Nickel* Bachelor's Thesis, University Konstanz.
- [95] Danan, H., Herr, A. & Meyer, A. J. P. (1968). New Determinations of the Saturation Magnetization of Nickel and Iron. *Journal of Applied Physics*. **39** (2), pp. 669–670. <https://doi.org/10.1063/1.2163571>.
- [96] Scott, G. G. (1952). The Gyromagnetic Ratios of the Ferromagnetic Elements. *Physical Review*. **87** (5), pp. 697–699. <https://doi.org/10.1103/PhysRev.87.697>.
- [97] Mentink, J. H., Hellsvik, J., Afanasiev, D. V., Ivanov, B. A., Kirilyuk, A., Kimel, A. V., Eriksson, O., Katsnelson, M. I. & Rasing, T. (2012). Ultrafast Spin Dynamics in Multisublattice Magnets. *Physical Review Letters*. **108** (5), p. 057202. <https://doi.org/10.1103/PhysRevLett.108.057202>.
- [98] Ostler, T. A., Barker, J., Evans, R. F., Chantrell, R. W., Atxitia, U., Chubykalo-Fesenko, O., El Moussaoui, S., Le Guyader, L., Mengotti, E., Heyderman, L. J., Nolting, F., Tsukamoto, A., Itoh, A., Afanasiev, D., Ivanov, B. A., Kalashnikova, A. M., Vahaplar, K., Mentink, J., Kirilyuk,

- A., Rasing, T. & Kimel, A. V. (2012). Ultrafast heating as a sufficient stimulus for magnetization reversal in a ferrimagnet. *Nature Communications*. **3**, p. 666. ISSN: 20411723. <https://doi.org/10.1038/ncomms1666>.
- [99] Radu, I., Vahaplar, K., Stamm, C., Kachel, T., Pontius, N., Dürr, H. A., Ostler, T. A., Barker, J., Evans, R. F. L., Chantrell, R. W., Tsukamoto, A., Itoh, A., Kirilyuk, A., Rasing, T. & Kimel, A. V. (2011). Transient ferromagnetic-like state mediating ultrafast reversal of antiferromagnetically coupled spins. *Nature*. **472** (7342), pp. 205–208. ISSN: 1476-4687. <https://doi.org/10.1038/nature09901>.
- [100] Stanciu, C. D., Hansteen, F., Kimel, A. V., Kirilyuk, A., Tsukamoto, A., Itoh, A. & Rasing, T. (2007). All-Optical Magnetic Recording with Circularly Polarized Light. *Physical Review Letters*. **99** (4), p. 047601. <https://doi.org/10.1103/PhysRevLett.99.047601>.
- [101] Wienholdt, S., Hinzke, D., Carva, K., Oppeneer, P. M. & Nowak, U. (2013). Orbital-resolved spin model for thermal magnetization switching in rare-earth-based ferrimagnets. *Physical Review B*. **88** (2), p. 020406. <https://doi.org/10.1103/PhysRevB.88.020406>.
- [102] Siegrist, F., Gessner, J. A., Ossiander, M., Denker, C., Chang, Y. P., Schröder, M. C., Guggenmos, A., Cui, Y., Walowski, J., Martens, U., Dewhurst, J. K., Kleineberg, U., Münzenberg, M., Sharma, S. & Schultze, M. (2019). Light-wave dynamic control of magnetism. *Nature*. **571** (7764), pp. 240–244. ISSN: 14764687. <https://doi.org/10.1038/s41586-019-1333-x>.
- [103] Turgut, E., La-o-vorakiat, C., Shaw, J. M., Grychtol, P., Nembach, H. T., Rudolf, D., Adam, R., Aeschlimann, M., Schneider, C. M., Silva, T. J., Murnane, M. M., Kapteyn, H. C. & Mathias, S. (2013). Controlling the Competition between Optically Induced Ultrafast Spin-Flip Scattering and Spin Transport in Magnetic Multilayers. *Physical Review Letters*. **110** (19), p. 197201. <https://doi.org/10.1103/PhysRevLett.110.197201>.
- [104] Melnikov, A., Razdolski, I., Wehling, T. O., Papaioannou, E. T., Roddatis, V., Fumagalli, P., Aktsipetrov, O., Lichtenstein, A. I. & Bovensiepen, U. (2011). Ultrafast Transport of Laser-Excited Spin-Polarized Carriers in Au/Fe/MgO(001). *Physical Review Letters*. **107** (7), p. 076601. <https://doi.org/10.1103/PhysRevLett.107.076601>.
- [105] Schellekens, A. J., Verhoeven, W., Vader, T. N. & Koopmans, B. (2013). Investigating the contribution of superdiffusive transport to ultrafast demagnetization of ferromagnetic thin films. *Applied Physics Letters*. **102** (25), p. 252408. <https://doi.org/10.1063/1.4812658>.

- 
- [106] Zhang, G. P. & Hübner, W. (2000). Laser-Induced Ultrafast Demagnetization in Ferromagnetic Metals. *Physical Review Letters*. **85** (14), pp. 3025–3028. <https://doi.org/10.1103/PhysRevLett.85.3025>.
- [107] Stamm, C., Pontius, N., Kachel, T., Wietstruk, M. & Dürr, H. A. (2010). Femtosecond x-ray absorption spectroscopy of spin and orbital angular momentum in photoexcited Ni films during ultrafast demagnetization. *Physical Review B*. **81** (10), p. 104425. <https://doi.org/10.1103/PhysRevB.81.104425>.
- [108] Koopmans, B., Ruigrok, J. J. M., Longa, F. D. & de Jonge, W. J. M. (2005). Unifying Ultrafast Magnetization Dynamics. *Physical Review Letters*. **95** (26), p. 267207. <https://doi.org/10.1103/PhysRevLett.95.267207>.
- [109] Rhie, H.-S., Dürr, H. A. & Eberhardt, W. (2003). Femtosecond Electron and Spin Dynamics in Ni/W(110) Films. *Physical Review Letters*. **90** (24), p. 247201. <https://doi.org/10.1103/PhysRevLett.90.247201>.
- [110] Bauer, M., Marienfeld, A. & Aeschlimann, M. (2015). Hot electron lifetimes in metals probed by time-resolved two-photon photoemission. *Progress in Surface Science*. **90** (3), pp. 319–376. ISSN: 0079-6816. <https://doi.org/10.1016/j.progsurf.2015.05.001>.
- [111] Li, Z., Wang, T., Jin, C., Lu, Z., Lian, Z., Meng, Y., Blei, M., Gao, M., Taniguchi, T., Watanabe, K., Ren, T., Cao, T., Tongay, S., Smirnov, D., Zhang, L. & Shi, S.-F. (2019). Momentum-Dark Intervalley Exciton in Monolayer Tungsten Diselenide Brightened via Chiral Phonon. *ACS Nano*. **13** (12). PMID: 31765125, pp. 14107–14113. <https://doi.org/10.1021/acsnano.9b06682>.
- [112] Gao, M., Zhang, W. & Zhang, L. (2018). Nondegenerate Chiral Phonons in Graphene/Hexagonal Boron Nitride Heterostructure from First-Principles Calculations. *Nano Letters*. **18** (7). PMID: 29936844, pp. 4424–4430. <https://doi.org/10.1021/acs.nanolett.8b01487>.
- [113] Miller, R. J. D. (2014). Femtosecond Crystallography with Ultrabright Electrons and X-rays: Capturing Chemistry in Action. *Science*. **343** (6175), pp. 1108–1116. ISSN: 0036-8075. <https://doi.org/10.1126/science.1248488>.



# Acknowledgments

For sure, this work would not have been possible, without the support, help and encouragement of many people. So I would like to express my gratitude at this point.

First of all, I would like to thank Prof. Dr. Ferenc Krausz for taking me as PhD candidate in his world-leading research group. It is an incredible experience to work with so many talented scientists doing such an outstanding research, which makes my time as a PhD a remarkable and unforgettable experience. I would also like to thank Prof. Dr. Alexander Urban for kindly agreeing to review my thesis.

Then I would like to express my deep gratitude to my immediate advisor Prof. Dr. Peter Baum for his guidance during my PhD. His continuous support and visionary mindset paired with his patience and enthusiasm played an important role with my research as a PhD and helped me to keep inspired with our project. I also want to thank him for finding great collaborators to work with and for always staying optimistic.

Many thanks to Dr. Dominik Ehberger for introducing me to the UED beamline and for his insight on all electron-pulse related questions and for his advice and support with my measurements. I also want to thank Dr. Mikhail Volkov for helping me to perform experiments and for his great knowledge of data evaluation. Moreover, I want to thank Dr. Bo-Han Chen for his continuous support of all questions regarding optics and optical pulse compression and for all the organizational information he provided with writing the thesis.

I would like to thank my collaborators Alexander Book and Prof. Dr. Wolfgang Kreuzpaintner for helping us with their great knowledge on thin-films and for developing with us a procedure to sputter those nickel thin-films on a tiny, fragile membrane. Without their knowledge and support, we could have not performed our experiments the way we did. Furthermore, I want to thank my other collaborators Prof. Dr. Ulrich Nowak, Dr. Martin Evers and Hannah Lange for their theoretical support and the implementation of the algorithm to corroborate

our theory of an angular momentum transfer to the crystal lattice. It is thanks to their calculations, that we kept on measuring and refining our measurements. I am thankful for all the knowledge they provide and their interest to keep on performing simulations. I would also like to thank Daniel Kazenwadel for his shared knowledge of Magneto-optical Faraday effect measurements and for performing and refining Magneto-optical Faraday effect experiments. I also want to thank him, Dr. Martin Evers, Dr. Dominik Ehberger and Johannes Thurner for proof-reading parts of this thesis.

I am grateful for all the other members of the UED group I had the pleasure to work with: Dr. Yuya Morimoto, Dr. Maxim Tsarev, Dr. Andrey Ryabov, Kathrin Mohler, Johannes Thurner, David Nabben, Eruthuparna Ramachandran, Ann-Kathrin Raab, Sven Jandura and Jannik Esslinger. All of them contributed to a great work atmosphere and offered a helping hand and advice in many occasions.

I would like to thank Mr. Öhm and his mechanical workshop team for always giving valuable advice with mechanical design and for providing us with the high-quality pieces we needed to improve our experiments.

Last but not least, I want to thank my parents for their support and encouragement and Andy Krüger for his endless patience and enduring encouragement in all these years. Andy, I am especially thankful for your continuous support in these last months of my PhD and I am grateful for all the knowledge you shared with me.